INFORMATION TO USERS

This manuscript has been reproduced from the microfilm master. UMI films the text directly from the original or copy submitted. Thus, some thesis and dissertation copies are in typewriter face, while others may be from any type of computer printer.

The quality of this reproduction is dependent upon the quality of the copy submitted. Broken or indistinct print, colored or poor quality illustrations and photographs, print bleedthrough, substandard margins, and improper alignment can adversely affect reproduction.

In the unlikely event that the author did not send UMI a complete manuscript and there are missing pages, these will be noted. Also, if unauthorized copyright material had to be removed, a note will indicate the deletion.

Oversize materials (e.g., maps, drawings, charts) are reproduced by sectioning the original, beginning at the upper left-hand corner and continuing from left to right in equal sections with small overlaps.

Photographs included in the original manuscript have been reproduced xerographically in this copy. Higher quality 6" x 9" black and white photographic prints are available for any photographs or illustrations appearing in this copy for an additional charge. Contact UMI directly to order.

ProQuest Information and Learning
300 North Zeeb Road, Ann Arbor, MI 48106-1346 USA
800-521-0600

SIGNAL PROCESSING ISSUES IN REFLECTION TOMOGRAPHY

BY

NAİL ÇADALLI

B.S., Bilkent University, 1994
M.S., Bilkent University, 1996

THESIS

Submitted in partial fulfillment of the requirements
for the degree of Doctor of Philosophy in Electrical Engineering
in the Graduate College of the
University of Illinois at Urbana-Champaign, 2001

Urbana, Illinois

UNIVERSITY OF ILLINOIS AT URBANA-CHAMPAIGN

THE GRADUATE COLLEGE

JANUARY, 2001

(date)

WE HEREBY RECOMMEND THAT THE THESIS BY

NAIL CADALLI

ENTITLED SIGNAL PROCESSING ISSUES IN REFLECTION TOMOGRAPHY

BE ACCEPTED IN PARTIAL FULFILLMENT OF THE REQUIREMENTS FOR

THE DEGREE OF DOCTOR OF PHILOSOPHY

David C. Munson Jr.
Director of Thesis Research

N. Narayana Rao
Head of Department

Committee on Final Examination†

David C. Munson Jr. Chairperson

David Jr. Parks

W. O'Brien

Andrew Singer

† Required for doctor's degree but not for master's.

O-517

SIGNAL PROCESSING ISSUES IN REFLECTION TOMOGRAPHY

Nail Çadallı, Ph.D.
Department of Electrical and Computer Engineering
University of Illinois at Urbana-Champaign, 2001
David C. Munson, Jr., Adviser

In this dissertation, three topics in reflection tomography are investigated: synthetic aperture radar (SAR) imaging of a runway and surroundings from an aircraft approaching for landing, acoustic imaging of objects buried in soil, and lidar imaging of underwater objects. Our investigation focuses on signal modeling and processing issues in the above problems.

The highly squinted geometry of runway imaging necessitates the incorporation of wavefront curvature into the signal model. We investigate the feasibility of using the wavenumber-domain ($\omega - k$) SAR inversion algorithm, which models the actual curvature of the wavefront, for runway imaging. We demonstrate the aberrations that the algorithm can produce when the squint angle is close to 90°, and show that high-quality reconstruction is still possible provided that the interpolation is performed accurately enough, which can be achieved by increasing the temporal sampling rate. We compare the performance with that of a more general inversion method (GIM) that solves the measurement equation directly. The performances of both methods are comparable in the noise-free case. Being inherently robust to noise, GIM produces superior results in the noisy case. We also present a solution to the left-right ambiguity of runway imaging using interferometric processing.

In imaging objects buried in soil, we pursue an acoustic approach, with the primary purpose of detecting and imaging cultural artifacts. We have developed a mathematical model and associated computer software in order to simulate the signals acquired by the actual experimental system, and a bistatic SAR-type algorithm for reconstruction. In the reconstructions from simulated data, objects were detectable, but near-field objects suffered from shifts and smears. To account for wavefront curvature, we formulated processing of the simulated data using the 3-D version of the monostatic $\omega - k$ algorithm.

In lidar imaging of underwater objects, we describe the relation between the airborne lidar returns and corresponding tomographic projections of an underwater object. Having data at various angular orientations with respect to the object, a 3-D tomographic

reconstruction is obtained. We have developed software to simulate lidar returns at a photomultiplier tube and a charge coupled device, using the bistatic lidar return equations. Our simulator can model multiple scattering and absorption for various water types and system parameters. Our simulated data fits the characteristics of real data very well. We present our reconstruction results from the simulated and real data, and comparatively discuss the reconstructions.

To my parents.

ACKNOWLEDGMENTS

I would like to express my gratitude to my advisor, Professor David C. Munson, Jr., for his guidance and constant encouragement during the course of this research. This work could not have been possible without his support. I feel privileged for having worked with him.

I would like to thank Professors David J. Brady, William D. O'Brien, Jr., and Andrew C. Singer for serving in my doctoral committee and for providing helpful comments and suggestions.

During my studies, I had the chance to work with Professor O'Brien and Professor Singer. I would like to thank them for their guidance. Also many thanks to my colleagues Kate H. Frazier and Peter J. Shargo with whom I worked during this research.

This research was funded by Rockwell International, the U. S. Army Construction Engineering Research Laboratory under Contract DACA88-96 K 0002 and the Office of Naval Research under grant N61331-00-1-G001.

This research was made possible by the outstanding research environment provided by the Coordinated Science Laboratory, the Department of Electrical and Computer Engineering, and the University of Illinois at Urbana-Champaign.

Many thanks to all my friends for their support and understanding.

Finally, I would like to thank my parents and my sister for their patience, encouragement, and constant support throughout my studies.

TABLE OF CONTENTS

LIST OF FIGURES

CHAPTER 1

INTRODUCTION

Tomography is the process of imaging of an object from data collected by illuminating the object from various directions. Tomography has a wide range of applications, including medical imaging, electron microscopy in microbiology, geophysical exploration, nondestructive testing, and astronomy, among others [1–12]. The fundamental mathematical problem in tomography is image reconstruction from projections, the solution of which dates back to Radon [13], and amounts to the inversion of the Radon transform [14–23]. A *projection* is the linear, planar, or curvilinear integral of a property of the object. In a broader sense, a projection is the information derived from the transmitted energy when the object is illuminated from a particular angle. The transmission can be in the form of x-rays, acoustic waves, microwaves, or electromagnetic energy in the optical band.

In *transmission tomography*, projections are obtained by measuring the amount of energy that passes through the object. The measurement is an integral of the attenuation coefficient or refractive index of the object medium when the measured quantity is the amplitude or the time of arrival of the received signal, respectively. A best-known example of this tomographic mechanism is x-ray *computerized tomography* (CT), which is also known as *computer-aided tomography* (CAT). In a CT scanner, a source illuminates the object to be imaged with a thin beam of x-rays. On the far side of the object, the beam is measured by an x-ray detector. This measurement gives an integral of the attenuation coefficient along the line between the source and the detector through the object. Using a parallel beam of x-rays and an array of detectors on the far side, a projection of the object's cross section at that particular angular orientation can be obtained. Having such projections at various angles around the object, a cross section of the object's 3-D

attenuation coefficient can be reconstructed. Reconstruction in the case of fan beam is also possible [2], [24].

Emission tomography, which can be classified under transmission tomography, produces images of the emissive properties of radioactive isotopes planted within an object. Certain chemical compounds containing radioactive nuclei can affix themselves to certain parts of the human body. Medical emission tomography exploits this fact to determine the location of the chemical and the associated tissue within the body by detecting the gamma rays emitted by the decay of the isotopes (or emitted as a result of interaction of emitted positrons with electrons) [25–28]. Another important technique of transmission tomography is *magnetic resonance imaging* (MRI). This technique is an application of nuclear magnetic resonance (NMR) principle [9, 29–31].

When the measurement is a function of the reflected energy instead of the transmitted energy, the imaging process is called *reflection tomography*. In reflection tomography, the measurement is an integral of the reflectivity of the object. Depending on the nature of the system, the reflectivity depends on acoustic, electromagnetic, or optical scattering properties of the object [32–38].

In certain imaging scenarios, due to physical constraints, transmission tomography is not possible, and hence, reflection tomography must be used. For instance, in geophysical exploration, it may not be possible to place receivers on the far side of the object area to be imaged. Or, simply, the object to be imaged may not be transparent; it may be totally opaque. As another example, in ultrasonic imaging, when there are impedance discontinuities in the tissue, the transmitted signal experiences a large attenuation and it is very difficult to obtain measurable signals on the far side of the object. Current ultrasonic medical imaging systems, therefore, mostly operate with reflected signals. The most straightforward method of imaging using the reflected signals is the *B-mode* (brightness-mode) scanning. In this imaging modality, a short pulse is transmitted into the object, which is usually a soft tissue. Echos are collected with the same probe acting as a receiver. The transmitter continually changes direction and scans the object with a narrow beam. The amplitudes of return signals are displayed as a function of time, or penetration depth, and illumination direction [9]. The length of the transmitted pulse determines the

range resolution, and the beam width determines the lateral resolution. Notice that the mechanism of B-scan imaging is the same as conventional single-antenna radar imaging.

Now consider that the object is illuminated by a wide spherical beam from a single point transducer that transmits short ultrasound pulses. Then the received signal at time instant t represents the integral of all reflections at a distance tv from the transducer, with v being the speed of propagation in the medium. For simplicity, assume that the object is 2-D. Then, the locus of equidistant points of the object from the transducer is a circular arc. Thus, the received signal at time t is a line integral of the reflectivity along a circular arc. In addition, the entire received signal as a function of time represents the projection of the reflectivity along circular arcs. If the object is illuminated by a plane wave instead of a spherical wave, the locus of equidistant points to the transmitter/receiver will be a plane. In that case, we have linear projections of the reflectivity instead of projections along circular arcs. Thus, as in the x-ray CT, obtaining projections at different angular orientations with respect to the object, a tomographic reconstruction can be obtained.

A prominent example of reflection tomography is synthetic aperture radar (SAR) imaging [39, 40]. With this technique, an antenna is mounted on an aircraft. As the radar platform moves along a flight path, the radar collects backscattered signals from an area on the ground from various angular views. The returned signals are then processed so as to effectively synthesize a large-aperture antenna. In the case of spotlight-mode SAR, the antenna is steered so as to illuminate the same area on the ground as the aircraft moves. In strip-mapping SAR, the antenna is fixed so as to sweep out a strip on the ground [41, 42]. In SAR imaging, the recorded signals with respect to time of arrival represent the integrals of the ground reflectivity over the area illuminated by the radar beam along concentric circular arcs centered at the location of the radar antenna. If the ground area to be imaged is far enough, the wave propagation can be assumed to be in the form of plane waves, and the integrals along the circular arcs can be approximated as the line integrals along the direction perpendicular to the direction of plane-wave propagation. In that case, the returned radar signal is a projection of the ground reflectivity along the direction of integration. As the SAR platform moves along the synthetic aperture and illuminates the scene at various angles, enough number of projections can be

obtained to produce a high-resolution image. Notice that this is the same mechanism of image formation as in the x-ray CT.

The basic mathematical relation often used in the inversion of the data for tomographic reconstruction is the famous projection-slice theorem [15–18]. In the case that the acquired measurement is the projection of a physical property along a line, the 1-D Fourier transform of the measurement is the slice of the 2-D Fourier transform of the physical property at the same angular orientation as the projection. In 3-D tomography, this can be generalized to plane projections as well as linear projections [40]. The reconstruction is still possible in the case of integrals along curvilinear paths [39, 43]. For other reconstruction techniques, the reader is referred to [5, 17].

When the size of inhomogeneities in the object is comparable to or smaller than a wavelength, ray theory, or the geometric propagation, is not adequate for inversion. It is then necessary to use wave propagation and diffraction-based methods. In that case, the fundamental relation that replaces the projection-slice theorem is the Fourier diffraction theorem, which provides frequency components of reflectivity on circular arcs instead of straight lines. This area of tomography dealing with diffracting waves is called *diffraction tomography* [5].

In this dissertation, three topics in reflection tomography are investigated: (1) SAR imaging of a runway and surroundings from an aircraft approaching for landing, (2) acoustic imaging of objects buried in soil, and (3) lidar (light detection and ranging) imaging of underwater objects. The first system uses microwaves, the second system uses acoustic waves, and the third uses electromagnetic energy in the optical band. These three seemingly different topics are related to each other in various ways. The first and second topics involve synthetic aperture imaging. We use 2-D wavenumber-domain SAR inversion for imaging of runways. We develop a SAR-type reconstruction algorithm for the acoustic imaging problem where we also formulate the problem as 3-D wavenumber-domain inversion. Lidar imaging of underwater objects is a direct application of 3-D reflection tomography. Since SAR itself is a tomographic reconstruction technique, these three topics are strongly related to each other.

Our investigation focuses on signal modeling and processing issues in the above problems. In runway imaging, we mainly deal with the issue of wavefront curvature. The

specific geometry of the problem necessitates the incorporation of wavefront curvature into the signal model. For this data collection geometry, we investigate the feasibility of using the wavenumber-domain ($\omega - k$) SAR inversion algorithm, which models the actual curvature of the wavefront, for runway imaging. We compare these results with a more general SAR inversion method which attempts to solve the measurement equation directly. In the study of acoustic imaging of buried objects, we develop a signal model for the acoustic returns. The signal model, which enables us to simulate the returns easily, does not take into account the wavefront curvature. Consequently, images of near-field objects suffer from aberrations. We describe how to apply the 3-D $\omega - k$ algorithm to the problem in order to model the wavefront curvature accurately. In the work on lidar imaging of underwater objects, we interpret the lidar returns within a 3-D reflection tomography framework. We simulate lidar returns using a sophisticated model that provides analytical expressions for the received signals. We describe a model for simulation of lidar returns at a charge-coupled device (CCD) after presenting the bistatic lidar return expressions.

Another common point between the above three topics is the following: Data collection in each of the systems is performed at the extremes of the usual parameter ranges we would use for a similar problem. In the first topic, for instance, data collection is performed when the radar looks almost straight ahead, contrary to the usual broadside data collection. In the second topic, unlike the airborne radar case, there are reflections from scatterers in the medium between the radar and the objects to be imaged, and the objects are in the near-field. In the third topic, the range of observation angles is small compared to the tomographic applications in medical imaging.

In tomography, it is not always possible to collect projection data over a complete angular range around the object. This is known as the *limited-angle* or *missing cone* problem, since a cone-shaped region (usually, a biconic section) of the frequency domain is missing [44, 45]. Using a reconstruction method that assumes a complete frequency domain may result in poor reconstructions. Various approaches have been proposed for the solution of this problem [46–50]. The topics of this dissertation involve a more difficult version of the missing cone problem. Contrary to the easier case where the missing section

is a small portion of the data, here, most of the data is missing; the available data in the frequency domain constitutes a narrow biconic section.

1.1 Overview

In SAR imaging of a runway from an aircraft approaching for landing, the objective is to determine whether there is any object either on or near the runway that would make the landing unsafe. Most aircraft carry weather radars. Although the resolution of these radars is sufficient to detect and localize storm calls, the resolution is not sufficient for imaging other aircraft or vehicles on or near a runway. We have conducted a study to see if these radars can be modified to form useful images of a runway and environs from a landing aircraft.

In runway imaging, the radar looks almost straight ahead, which makes the squint angle close to 90 degrees. In such a high-squint case, the range of observation angles is very narrow, and it becomes necessary to take wavefront curvature into account to obtain higher resolution. Conventional SAR imaging algorithms that rely on a plane-wave assumption do not provide sufficient accuracy for the highly squinted case.

The popular $\omega - k$ algorithm successfully incorporates wavefront curvature into the processing. It has been reported in the literature that for broadside data collection scenarios the method produces very good results. The algorithm has not been studied for high squint angles except in runway imaging studies by Choi [51] and Lee [52]. In these studies, the method has been reformulated by using Hilbert space concepts. Point target simulations showed spurious targets that could not be explained. It was believed that the algorithm broke down at high squint angles due to inaccuracies in employed approximations.

In our work, we show that high-quality reconstruction is still possible for squint angles close to 90° provided that the interpolation is performed accurately enough. We first perform a careful analysis of the method, especially, of the interpolation step. We show that the interpolation can be improved by increasing the number of temporal samples, which in turn increases the overall computational complexity only linearly. We have implemented the algorithm as a fast and user-friendly, pieces of Matlab and C software,

which permits us to easily generate simulation results for different target locations, data collection segments, sampling rates and interpolation schemes. Our simulations demonstrate that the aberrations which occur when the squint angle is close to 90° can be eliminated by performing the interpolation more accurately.

The $\omega - k$ algorithm is not the only method that takes into account wavefront curvature and there is no reason to believe it is the optimal approach for the high squint-angle case. We therefore compare the performance of the $\omega - k$ algorithm with a more general inversion method that solves the measurement equation directly and accurately models the curvature of the wavefront. Our results show that the performance of the $\omega - k$ algorithm is comparable to that of the general inversion method (GIM). In the noisy case, however, GIM produces superior results since GIM is inherently robust to noise.

The runway imaging problem is subject to left-right ambiguity. This is because radar imaging relies on the ranging principle, so that a target to the left of the runway appears in the reconstruction at the same location as a target located symmetrically about the centerline to the right of the runway. We present our solution of the left-right ambiguity problem which makes use of a secondary set of data collected in an interferometric manner by a secondary receiver.

In the study of acoustic imaging of objects buried in soil, our motivating application is the detection and imaging of cultural artifacts. In this study, we apply synthetic aperture theory. We have developed a mathematical model and associated computer software to simulate the signals acquired by an actual experimental system, which consisted of an array of receiving elements, a circular omnidirectional transmitter, data collection equipment and a box of sand to bury objects in. We also have developed a SAR-type reconstruction algorithm for the acoustic scenario with data collected in a bistatic manner by using a linear array as the receiver. The main differences between the usual (strip-mapping) SAR scenario and the acoustic scenario are the following: (1) In usual SAR geometry, distances are large enough to satisfy the assumption of plane-wave or quadratic-wave propagation. (2) The soil medium is very attenuating. In the usual SAR scenario the medium between the radar and the scatterers is air, and hence, attenuation due to the medium is negligible. (3) The usual SAR return is spatially a single signal. In the

acoustic case, a linear array is used for beamforming to focus the received signals in the direction of the array.

We modify the conventional correlation-based strip-mapping SAR algorithm for bistatic acoustic data collection, along with compensation for signal attenuation. The bistatic SAR-type reconstruction algorithm, however, suffers from shifts and smears for near-field objects, since the employed assumption of plane-wave propagation is not accurate enough in the near field. On the other hand, the $\omega - k$ SAR algorithm, which takes wavefront curvature into account, can provide more accurate results for near-field objects. We present our formulation of the image reconstruction problem for the 3-D monostatic $\omega - k$ algorithm.

Detection and localization of underwater objects such as mines is an important problem for safe operation of naval platforms. Airborne lidar systems can transmit laser beams that can penetrate the air-water interface and optically detect and localize underwater mines. Transmitted optical energy is subject to scattering and absorption in water, similar to the effects observed in the acoustic imaging scenario above. Parts of the reflected optical field, can be captured by CCDs and PMTs (photomultiplier tubes). The CCDs generate images of the scatterers in the illuminated water column, while the PMT returns provide information about the scene in the range direction. The images and PMT returns can be analyzed and processed by a trained operator to detect, classify and locate hazardous objects.

In the study of lidar imaging of underwater objects, we formulate the above detection and localization problem as a 3-D tomographic reconstruction problem: We describe the relation between the airborne CCD/PMT returns and corresponding tomographic projections of an underwater object. Having CCD/PMT data at various angular orientations with respect to the object, a 3-D tomographic reconstruction can be obtained. We have developed software to simulate lidar returns in PMT and CCD sensors. Our simulator can model multiple scattering and absorption for various water types and system parameters. We also worked with a real data set from a previous study (1998 Competitive Evaluation Field Test (CEFT), Panama City, FL). Our simulated data fits the characteristics of real data very well. We present our reconstruction results from the simulated and real data, and comparatively discuss the reconstructions.

CHAPTER 2

SAR IMAGING OF RUNWAYS

2.1 Introduction

Radar imaging of runways from aircraft approaching for landing is of considerable interest since radar is capable of imaging in all weather conditions. Most aircraft carry weather radars. Although the resolution of these radars is sufficient to detect and localize storm calls, the resolution is not sufficient for imaging other aircraft or vehicles on or near a runway. This raises the question of synthetic aperture signal processing, to potentially improve resolution. Synthetic aperture radar (SAR) can produce very high resolution imagery [39, 40, 53–56]. In this chapter, we investigate SAR signal processing as a means of forming useful images of a runway and environs from a landing aircraft.

SAR typically employs approximations of the wavefront. The traditional plane-wave approximation used in spotlight-mode SAR leads to a model where the demodulated return signals represent polar spatial-frequency components of the scene. Polar-to-Cartesian interpolation followed by a 2-D inverse Fourier transform produces the SAR image. The geometry for runway imaging, which is described in Section 2.2, however, requires more accurate modeling and processing of the radar return. This is possible by taking into account the wavefront curvature. The so-called wavenumber-domain methods (also known as $\omega - k$ or k-domain algorithms) increase the resolution by modeling the actual spherical wave [57–63]. In [57] and [58], the image formation algorithm is developed by using seismic migration techniques [64, 65]. In [59], the inversion problem is solved by using a decomposition of the spherical wave into its plane-wave components [66]. The method also has been formulated using Hilbert-space concepts without requiring any knowledge of wave propagation [51]. The following description is based on this latter ap-

proach. The processing has also been formulated by using the Hankel transform instead of the Fourier transform [62].

The $\omega - k$ algorithm previously has been suggested for imaging a runway from an approaching aircraft in order to determine whether there is any object either on or near the runway that would make the landing unsafe [67]. The Federal Aviation Administration (FAA) regulations require that an aircraft maintain a distance of 76.2 m (250 ft) from the center of the runway when it does not have clearance to proceed to the runway. Objects on the runway, or inside the prohibited region, need not to be imaged with high-resolution. But they must be visible in the radar image so that the aircraft can abort landing. On the other hand, objects safely in the clearance region must be imaged with high resolution so that they are not smeared into the prohibited area in the radar image, which could cause a false alarm.

The $\omega - k$ algorithm models the acquired data as spatial frequency components of the radar reflectivity on a non-Cartesian grid. The frequency components are interpolated onto a Cartesian grid and a 2-D inverse Fourier transformation is applied in order to compute the spatial-domain image. Interpolation introduces error in the image reconstruction. In runway imaging, the radar looks almost straight ahead. At high squint angles, because of severe geometric distortion of the Fourier data grid, more accurate interpolation becomes necessary. In the literature, the $\omega - k$ algorithm is generally discussed only for broadside or slightly squinted cases where the interpolation is relatively simple and accurate. At high squint angles, the $\omega - k$ algorithm shows aberrations. It has been believed that the algorithm breaks down at high squint angles, due to error introduced by the Fourier transform approximation of the imaging kernel, in addition to inaccuracies in the interpolation.

In this chapter, we characterize the aberrations that occur when the squint angle is close to 90° and show that the performance of the $\omega - k$ method can be improved by increasing the accuracy of the interpolation, and that this can be done by increasing the number of temporal frequency samples of the radar spectrum. The complexity of the algorithm increases only linearly in the number of temporal samples. There have been some remarks in the literature about the fact that more accurate interpolation is needed for the highly squinted case, but the relation of this point to the number of temporal

samples was not addressed before. Furthermore, we provide an explanation for why the error due to the Fourier transform decomposition of the imaging kernel has little effect on the image reconstruction quality.

The $\omega - k$ algorithm decomposes the imaging kernel using the Fourier basis. Thus, it may not be the optimal method for the high-squint-angle case. We therefore compare, for a given level of computational complexity, the performance of the $\omega - k$ algorithm with a more general inversion method (GIM). This method is a numerical solution technique for a certain type of Fredholm integral equation that models our radar returns.

The runway imaging problem is subject to left-right ambiguity. This is because of the fact that radar imaging relies on the ranging principle, so that the radar can not differentiate between any two point objects at equal distances to the radar. In runway imaging, this amounts to imaging a target to the left of the runway on the right. We propose a solution to the left-right ambiguity problem, which makes use of a secondary set of data collected in an interferometric manner by a secondary receiver.

This chapter is organized as follows: We first describe the data acquisition scenario. Then we investigate the feasibility of data collection in terms of required cross-track resolution, data collection distance (equivalently, data acquisition time) and cross-track location of a target. Then we review the steps of the $\omega - k$ algorithm and present our point target simulation results for the runway imaging scenario. We discuss the feasibility of using this method, based on simulation results. Then we describe GIM and compare its effectiveness with the $\omega - k$ algorithm. Finally, we formulate a solution to the left-right ambiguity problem in runway imaging and present simulation results using the $\omega - k$ algorithm.

2.2 Data Acquisition Model

Figure 2.1 describes the geometry of the data collection in the ground plane. (All figures appear at the end of chapters.) The radar platform is an aircraft approaching a runway for landing. The flight path is along the y axis, and the origin of the coordinate system is at the midpoint of the synthetic aperture. The runway lies along the y axis straight ahead of the aircraft. The elevation of the aircraft in the z direction is omitted

but the generalization of the data model to slant-range geometry is straightforward. If we wished to include the elevation in the data model, we could perform the processing in the slant plane and project the data onto the ground plane, which may be accomplished in the Fourier domain as well. However, since the elevation-angle of approach of the aircraft for landing can be as small as 3°, the slant plane and ground plane data are almost the same in the current situation.

The radar collects data along its flight path from $y = -\frac{L_a}{2}$ to $y = \frac{L_a}{2}$ where L_a is the synthetic aperture length. The squint angle γ_0 of the scene center (X_0, Y_0) with respect to the origin of the coordinate system, is given by $\arctan(Y_0/X_0)$. The observation angle γ' corresponding to an arbitrary point (x', y') in the scene with respect to the radar platform is given by $\arctan((y'-y)/x')$. The radar beam illuminates a spotlight patch on the ground. At high squint angles close to 90° and with an elevation-angle of approach of 3°, the ground patch is a long ellipse with the longer axis along the along-track direction. For example, if the runway is 3200 m ahead, the antenna size is 1 m and the radar frequency is 10 GHz, then the scene is an ellipse with the longer axis being about 3600 m, whereas the shorter axis is 192 m. The area to be imaged, which is called the *scene*, is a smaller subarea of the ground patch and has size L_x by L_y. The shape of the scene area can be taken as a rectangle, an ellipse, or a circle within the area illuminated by the mainlobe of the radar beam by digital spotlighting. Different parts of the runway, that is, different scenes, can be imaged simultaneously.

In a data collection session, the radar transmits a pulse and collects the return at regular spatial intervals along its flight path. The transmitted signal is a real passband signal $\Re e\{s_T(t)\}$ where $s_T(t)$ is a linear FM (chirp) waveform given as

$$s_T(t) = p(t)\exp(j\omega_0 t) = \begin{cases} e^{j(\omega_0 t + \alpha t^2)} & |t| \le \frac{\tau_p}{2} \\ 0 & \text{otherwise} \end{cases} \tag{2.1}$$

where f_0 is the center frequency of the chirp signal, $\omega_0 = 2\pi f_0$, and 2α is the chirp rate in radians per second squared. The temporal variable t is called *fast time* in radar terminology. The instantaneous frequency of the chirp is given by

$$f_c(t) = \frac{1}{2\pi}(\omega_0 + 2\alpha t)\ . \tag{2.2}$$

The corresponding range of temporal frequencies extend from $\omega_0 - \alpha\tau_p$ to $\omega_0 + \alpha\tau_p$. Thus, the temporal bandwidth of the transmitted waveform is

$$B_T = \frac{1}{2\pi} 2\alpha\tau_p = \frac{\alpha\tau_p}{\pi} \ . \tag{2.3}$$

Let the range function be given by

$$r(x', y - y') = \sqrt{x'^2 + (y - y')^2} \tag{2.4}$$

when the radar is at location y on the flight path and the coordinates of a particular scatterer are given by (x', y'). As shorthand notation we will denote the range function by r'_y, which indicates the dependence of the range function on the primed coordinates (x', y') and the location y of the radar. Depending on the location of the scatterer and the position of the radar on the flight path, r'_y takes values in $[r_{min}, r_{max}]$.

The complex reflectivity function of the scene is denoted by $g(x, y)$ which can also be written as

$$g(x, y) = |g(x, y)| \ \exp\left(j\psi(x, y)\right) \tag{2.5}$$

in terms of its magnitude and phase. Due to the finite antenna footprint, $g(x, y)$ is not recoverable outside the antenna footprint. Insofar as the scene area is uniformly illuminated by the mainlobe of the antenna beam, the antenna gain actually can be assumed to be incorporated in $g(x, y)$. For a more general formulation, one should use a window function $w(x', y', y)$ to model the spotlight-mode antenna pattern separately. Since, in the spotlight mode, the antenna is steered to continuously point to the same scene area on the ground as the radar platform moves along the flight path, the magnitude of $w(x', y', y)$ for each point (x', y') in the scene depends on the observation angle $\arctan(\frac{y'-y}{x'})$. For the subsequent formulation, we assume that the scene area is inside the area illuminated by the mainlobe of the radar beam, and hence almost uniformly illuminated. In other words, the antenna pattern $w(x', y', y)$ can be assumed to be unity within the scene area. Notice that we assume that the reflectivity function is not dependent on the frequency of the radiation or the observation angle. This is justifiable as long as the radar is narrowband and the range of observation angles is small. Most targets do have frequency- and

direction-dependent reflectivity. Therefore, for wideband and wide-angle radars, which are mainly used to see through foliage, it is necessary to incorporate those dependencies into the reflectivity model. There are some studies for ultra wideband, wide-angle radars in that direction [68–70]. In the runway imaging case, however, the range of observation angles is small. Furthermore, the radar uses narrow-band pulses. Hence a reflectivity model with two arguments instead of four is adequate.

The return signal from a scene with reflectivity $g(x, y)$ is the collection of returns from all infinitesimal scatterers in the scene. The return signal in real passband form can be written as

$$\tilde{s}_R(t, y) = \iint_{-\infty}^{\infty} |g(x', y')| \, \Re e \left\{ p(t - \frac{2r'_y}{c}) \, \exp\left(j(\omega_0(t - \frac{2r'_y}{c}) + \psi(x', y')) \right) \right\} \, dx'dy' \, . \tag{2.6}$$

This is the data obtained when the radar is at location y.

2.2.1 Issue of wavefront curvature

The plane-wave approximation, which is usually employed in SAR inversion, is justified if the nonplanar wavefront can be approximated closely enough with a planar wavefront. This is possible when the scene is in the far field, in which case the range error between the actual wavefront curvature and assumed planar wavefront is small. In the near field, however, the range error is not tolerable. Range error causes degradation in the reconstruction in the form of shifts and smears in target images.

The runway imaging scenario has a geometry that is seemingly consistent with the far field, but the highly squinted geometry makes it necessary to incorporate wavefront curvature into the processing. In the electromagnetic theory of scattering, the extent of the near field is given by $2D^2/\lambda$, where D is the maximum dimension of the antenna [71]. For typical radar parameters, this limit is very small compared to the typical range values for runway imaging; hence, runway imaging can be considered to be in the far field in that sense. However, since the range of observation angles in this highly squinted geometry is

small compared to that in the broadside far-field data collection, it is difficult to achieve high resolution with conventional SAR inversion based on a plane-wave assumption.

The effects of the plane-wave approximation in the polar-format algorithm, which assumes plane-wave propagation, has been studied with point targets for both broadside and squint geometries [40,72]. For typical parameters in runway imaging, the effects of the plane-wave assumption appear as severe shifts and smears of imaged targets, especially for targets close to the runway center. Furthermore, for the plane-wave approximation to hold, there are certain constraints on the size of the scene area that can be imaged with reasonable resolution [39, 40]. In runway imaging these constraints are more restrictive than in the broadside case. It is therefore necessary to incorporate wavefront curvature into the processing for runway imaging. The $\omega - k$ algorithm performs this incorporation by modeling the actual spherical wavefront. For broadside and slightly squinted data collection, considerable improvement has been reported [57–59], through use of the $\omega - k$ algorithm.

2.2.2 Feasibility of data acquisition

Resolution in the cross-track direction for the highly squinted case, provided by the $\omega - k$ algorithm, is later derived as (2.48). For a target at location (x', y') with respect to the radar platform, the cross-track resolution is given by

$$\delta_x = \frac{c\pi}{\omega_{max}\cos(\gamma'_{min}) - \omega_{min}\cos(\gamma'_{max})} \tag{2.7}$$

where γ'_{min} and γ'_{max} are the minimum and maximum observation angles to the target. Maximum and minimum observation angles correspond to the beginning and end of the synthetic aperture, respectively. These extreme angles can be represented in terms of the location of the target and the radar platform as

$$\begin{aligned} cos(\gamma'_{min}) &= \frac{x'}{\sqrt{x'^2 + (y' - L_a/2)^2}} \\ cos(\gamma'_{max}) &= \frac{x'}{\sqrt{x'^2 + (y' + L_a/2)^2}} . \end{aligned} \tag{2.8}$$

Inserting these expressions into the cross-track resolution expression given in (2.7), we obtain the resolution in terms of the location of the target, (x', y'), the extreme points of the temporal bandwidth of the radar signal, ω_{min}, ω_{max}, and the synthetic aperture length, L_a. If the speed of the radar platform is known, the resolution can also be expressed in terms of total data collection time [67]. However, since the speed of radar platforms may vary and since the speed may not be constant throughout the aircraft's travel along the synthetic aperture, we find it more useful to express the relations in terms of the synthetic aperture length.

The cross-track resolution depends on the range of observation angles through which a target is illuminated by the radar beam. This has the following consequences:

(1) The resolution values for targets at different locations in the scene are different. Targets far from the runway, that is, the y axis, can be reconstructed with higher resolution since the range of observation angles would be larger for them compared to targets closer to the runway. In that sense, a target right on the runway has zero cross-track resolution[1] since the range of observation angles is zero for that target. The location of the target in the along-track dimension also affects the range of angles through which it is observed. If two targets have the same cross-track coordinate, but one is closer to the radar in the along-track dimension, the closer target will be reconstructed with higher resolution. This is illustrated in a contour mesh graph in Figure 2.2 where the cross-track resolution δ_x is computed and plotted for each point in the scene area.

(2) When the radar is very far away from the scene, there is not a large change in the observation angles as the radar travels along the synthetic aperture. The radar illuminates the target at about the same angle all along the aperture. However, if the radar platform is at a moderate distance to the scene, acceptable cross-track resolution values can be obtained. The range of "moderate" distance values can be computed easily from the resolution formula. For example, for a target at cross-track location $x' = 60$ m and with a radar bandwidth of 32 MHz centered about 10 GHz and synthetic aperture length of 500 m, we plot the achievable resolution versus the scene distance in Figure 2.3.

[1] *Resolution* is used to mean either resolution as a general concept or the minimum distance at which two targets can be resolved. *Resolution distance* would be a less ambiguous name for the latter. Here the resolution distance is infinite (ignoring limits placed by the antenna beam width), and the resolution is zero.

At a couple of kilometers from the scene, we achieve very useful resolution values. Data acquisition much closer to the scene produces better resolution. However, in the landing approach, the pilot needs a margin to decide and safely maneuver to abort the landing in case of emergency. This safety distance can be calculated by using the recommended speed and altitude profile of the aircraft during landing and considering the required time to perform such maneuvers. A typical landing speed for an aircraft is 65 m/s, which would result in 30 s for decision and approximately a 2 km distance from the runway.

From the cross-track resolution formula resulting from (2.7) and (2.8), we can compute the cross-track resolution for different synthetic aperture lengths as a function of cross-track position. Figure 2.4 shows results of such a computation. In the plot, the solid curves are for the along-track location of the target $y' = 3200$ m and dashed curves are for $y' = 1600$ m. Both sets of curves, from top to bottom, are for synthetic aperture lengths 500 m, 1300 m, and 2100 m. Conversely, given a desired resolution and the location of the target, the required synthetic aperture length can be calculated as displayed in Figure 2.5, where the solid curves are for the along-track location of the target $y' = 3200$ m, and dashed curves are for $y' = 1600$ m. In both sets of curves, from top to bottom, resolutions are 3 m, 8 m, and 13 m.

2.3 Wavenumber-Domain Processing

Let R_0 be the distance from the origin of the coordinate system to the center (X_0, Y_0) of the target scene. Let $\tau_0 = \frac{2R_0}{c}$. Also define the temporal frequency $\omega = \omega_0 + 2\alpha(t - \tau_0)$. The wavenumber is given by $k = \omega/c$. If the transmitted signal is a linear FM pulse as given in (2.1), then by deramping, that is, by passing the return signal through a quadrature demodulator at an oscillation phase of $\omega_0(t - \tau_0) + \alpha(t - \tau_0)^2$, we obtain, after some algebraic manipulations (see Appendix A), the return signal in complex baseband as

$$s_R(t, y) = \iint_{-\infty}^{\infty} g(x', y') \exp\left(-j2kr'_y\right) \exp\left(j2kR_0\right) \exp\left(j\frac{4\alpha}{c^2}(r'_y - R_0)^2\right) dx'dy' \,. \quad (2.9)$$

The return is zero outside the interval $t \in [t_{min}, t_{max}] = [-\frac{\tau_p}{2} + \frac{2}{c}r_{min}, \frac{\tau_p}{2} + \frac{2}{c}r_{max}]$ due to the finite-time pulse $p(t)$. Hence, $\omega \in [\omega_0 + 2\alpha(t_{min} - \tau_0), \omega_0 + 2\alpha(t_{max} - \tau_0)]$. Hence, bandwidth of the received signal is

$$B_R = \frac{\alpha}{\pi}\left(\tau_p + \frac{2}{c}(r_{max} - r_{min})\right) , \tag{2.10}$$

which is almost equal to the bandwidth B_T of the transmitted signal since the second term in parentheses is much smaller with respect to the duration of the transmitted pulse.

A point to notice about the data model is that an amplitude function to account for the spherical spreading of the electromagnetic waves has not been included. As the emitted spherical wave travels the round trip distance $2r'_y$ between the radar and a particular reflector, its amplitude is attenuated by $1/(r'_y)^2$. Since r'_y is proportional to fast time t, the attenuation can be compensated by multiplying $s_R(t, y)$ by t^2. Since the transmitted pulse is not an impulse, this correction, however, is only approximate.

The second exponential in (2.9) is known and the third exponential term can be corrected afterwards or can be totally omitted if the time-bandwidth product of the radar signal is large enough [39]. Then, letting the *imaging kernel* be denoted by

$$f(x', y; \omega) = \exp\left(-j2kr(x', y)\right) \tag{2.11}$$

and omitting the second and third exponential terms, we can write the return signal as

$$s(\omega, y) = \iint_{-\infty}^{\infty} g(x', y')\ f(x', y - y'; \omega)\ dx'dy' . \tag{2.12}$$

Such an integration represents nonseparable projection in x and convolution in y and is a special case of the well-known Fredholm integral equation with a nonseparable kernel [73]. The GIM in [74] provides for an efficient estimation of the solution to this integral equation. The GIM approach has been formulated for synthetic aperture radar imaging [75]. Here we first describe the so-called $\omega - k$ algorithm, which operates in the wavenumber domain and exploits the synthetic aperture radar principle. We describe

the GIM SAR inversion method in Section 2.4.1 where we compare its results with those of the $\omega - k$ algorithm.

2.3.1 Wavenumber-domain image formation

Denote the 2-D Fourier transform of $f(x', y; \omega)$ by $F(k_{x'}, k_y; \omega)$ which satisfies

$$f(x', y; \omega) = \frac{1}{4\pi^2} \iint_{-\infty}^{\infty} F(k_{x'}, k_y; \omega) e^{j(k_{x'}x' + k_y y)} \, dk_{x'} dk_y \, . \tag{2.13}$$

Inserting this into (2.12), we obtain

$$s(\omega, y) = \frac{1}{4\pi^2} \iint_{-\infty}^{\infty} F(k_{x'}, k_y; \omega) \iint_{-\infty}^{\infty} g(x', y') e^{j(k_{x'}x' + k_y(y - y'))} \, dx' dy' \, dk_{x'} dk_y \, , \tag{2.14}$$

which can be written as

$$s(\omega, y) = \frac{1}{4\pi^2} \iint_{-\infty}^{\infty} F(k_{x'}, k_y; \omega) e^{jk_y y} \iint_{-\infty}^{\infty} g(x', y') e^{j(k_{x'}x' - k_y y')} \, dx' dy' \, dk_{x'} dk_y \, . \tag{2.15}$$

The second double integral is $G(-k_{x'}, k_y)$ where $G(k_{x'}, k_y)$ is the 2-D Fourier transform of $g(x, y)$. Then we have

$$s(\omega, y) = \frac{1}{4\pi^2} \iint_{-\infty}^{\infty} F(k_{x'}, k_y; \omega) G(-k_{x'}, k_y) e^{jk_y y} \, dk_{x'} dk_y \, . \tag{2.16}$$

An expression for the Fourier transform, $F(k_{x'}, k_y; \omega)$ of the imaging kernel $f(x', y; \omega)$ is derived in Appendix C. We have not found it necessary to evaluate the Fourier transform for $|k_y| > 2k$ in (C.12). That is because the radar receiver only records nonevanescent waves. Evanescent waves which correspond to waves with wavenumber in the range $|k_y| > 2k$ decay within a distance of a few wavelengths. Although we mathematically carried along the evanescent component in Appendix C, in reality that part is zero since the imaging kernel does not produce frequencies in that range. Hence, the 2-D Fourier

transform of the imaging kernel can be taken to be

$$F(k_{x'}, k_y; \omega) \approx \begin{cases} 2\pi A_1 \, \delta(k_{x'} + \sqrt{4k^2 - k_y^2}) & |k_y| < 2k \\ 0 & |k_y| > 2k \end{cases} \tag{2.17}$$

where A_1 is a complex constant defined in Appendix C. Actually, A_1 is an approximation to a slowly varying function of x'. Besides this approximation, the above expression involves the asymptotic approximation of a Hankel function (see Appendix C). Both of these approximations become less accurate if the squint angle is close to 90°. However, these approximations introduce error only in amplitude functions. Error in amplitude does not affect the reconstruction as much as error in phase. That is why the interpolation error, which affects the phase of the Fourier domain samples, has a larger effect on image quality. As a matter of fact, as can be seen in the simulations, the performance of the $\omega - k$ algorithm can be improved by using more accurate interpolation, and the errors due to the approximations involved in the above expression do not seem to affect the reconstruction.

By using the approximation in (2.17) we obtain

$$s(\omega, y) \approx \frac{A_1}{2\pi} \int_{-2k}^{2k} G(\sqrt{4k^2 - k_y^2}, k_y) e^{jk_y y} \, dk_y \, . \tag{2.18}$$

Since recorded waves satisfy $k_y \leq 2k$, the limits of the integral in (2.18) can be extended to infinity, which yields an inverse Fourier transform integral. Hence,

$$S(\omega, k_y) \approx A_1 G(\sqrt{4k^2 - k_y^2}, k_y) \tag{2.19}$$

where $S(\omega, k_y)$ is the 1-D Fourier transform of $s(\omega, y)$. Let

$$k_x = \sqrt{4k^2 - k_y^2} \, . \tag{2.20}$$

Then (2.19) tells us that the collected data $s(\omega, y)$ is the 1-D inverse Fourier transform of $A_1 G(k_x, k_y)$ in the variable y. In other words, taking the 1-D Fourier transform of the collected data $s(\omega, y)$ in the y dimension, we obtain the 2-D Fourier transform of

the reflectivity function within a complex constant. Thus, taking the 2-D inverse Fourier transform of (2.19) we can obtain $g(x, y)$ and display its magnitude as the reconstructed image. However, as indicated by the relation in (2.20), k_x and k_y lie on an irregular grid, the form of which will be examined in a later section. This complicates the problem because, in order to be able to use a fast Fourier transformation (FFT), the data must lie on a Cartesian grid. Therefore, as an intermediate step, data on this irregular grid is interpolated onto a Cartesian grid before a 2-D inverse FFT is applied.

The image formation algorithm is summarized in Figure 2.6. In the first phase multiplication, k_y^c is the center frequency of the data in the y dimension. This phase multiplication in the spatial domain causes the k_y spectrum of the data to be shifted to baseband. The second phase multiplication in the wavenumber domain shifts the spatial-domain data such that the center of the reconstructed image is the scene center.

2.3.2 The Fourier data and its interpolation

The return signal in (2.12) is a sum of complex exponentials (imaging kernel) of the form

$$e^{j\phi(y)} = \exp\left(-j2k\, r(x', y - y')\right) \tag{2.21}$$

When considered as a function of y, the instantaneous angular spatial frequency (wavenumber) of this quantity is

$$k_y = \frac{d\phi(y)}{dy} = \frac{d}{dy}\left(-2k\sqrt{x'^2 + (y - y')^2}\right) \tag{2.22}$$

$$= 2k\frac{(y' - y)}{\sqrt{x'^2 + (y - y')^2}} \tag{2.23}$$

Defining

$$\sin\gamma_y' = \frac{(y' - y)}{\sqrt{x'^2 + (y - y')^2}} \tag{2.24}$$

we have the wavenumber in the y direction as

$$k_y = 2k \sin \gamma_y' \tag{2.25}$$

where γ_y' is the observation angle of a point scatterer at (x', y') with respect to the radar at position y along the flight path. Correspondingly, from the definition in (2.20),

$$k_x = 2k \cos \gamma_y' \ . \tag{2.26}$$

As the radar moves along the flight path, and for point scatterers at various locations in the scene, the angle γ_y' sweeps through the range of values in $[\gamma_{min}, \gamma_{max}]$. The temporal frequency ω is in $[\omega_{min}, \omega_{max}]$. Hence, the Fourier data $S(\omega, k_y)$ covers the area shown in Figure 2.7 in the $\omega - k_y$ plane. The wavenumbers k_x and k_y satisfy,

$$4k^2 = k_x^2 + k_y^2 \ , \tag{2.27}$$

which is the equation of a circle with radius $2k$ in the $k_x - k_y$ plane. Thus, the Fourier data lie on arcs that are parts of concentric circles between radial lines determined by the extremes of the squint angles as shown in Figure 2.8. This is the data to be interpolated onto a Cartesian grid before inverse Fourier transformation. This data grid is not polar since the data points do not necessarily lie on radial lines, but rather their locations in the $k_x - k_y$ plane are determined by ω and k_y.

Let us denote equally spaced values of ω and k_y as vectors $\underline{\hat{\omega}}$ and $\underline{\hat{k}}_y$ of size N_ω and N_y, respectively. (Actually, we have $N_\omega \times N_a$ samples of the return signal, $s(\omega, y)$. The number of discrete locations along the flight path (azimuth) at which the radar sends probing signals is N_a. The number of pixels in the reconstructed image in the along-track direction is denoted by N_y. For easier and faster interpolation we take $N_y = N_a$. The nominal value of N_a satisfying the Nyquist sampling requirement is suitable for the image size as well.) Then for a fixed k_y value, say $\hat{k}_y^j$, which is the jth component of $\underline{\hat{k}}_y$, we can write the following by using (2.20):

$$\tilde{k}_{x,j}^{\ell} = \sqrt{\frac{4}{c^2}(\hat{\omega}^{\ell})^2 - (\hat{k}_y^j)^2}, \qquad 0 \le \ell \le N_\omega - 1 \tag{2.28}$$

where $\underline{\tilde{k}}_{x,j}$ denotes the vector of unevenly spaced k_x values of size N_ω. Notice the dependence of the vector $\underline{\tilde{k}}_{x,j}$ on j, and in turn, on $\underline{\hat{k}}_y^j$. This is because the different $\underline{\hat{k}}_y^j$ values correspond to different sets of $\underline{\tilde{k}}_{x,j}^\ell$ values as can be easily seen in Figure 2.8. Now define the vector $\underline{\hat{k}}_x$ of size N_x to be the evenly spaced grid of k_x values. Then, $\underline{\hat{k}}_x$ and $\underline{\hat{k}}_y$ define a Cartesian grid and this corresponds to a matrix $\underline{\underline{\tilde{\omega}}}$ of size $N_x \times N_y$ which consists of unevenly spaced ω values

$$\underline{\underline{\tilde{\omega}}}^{ij} = \frac{c}{2}\sqrt{(\underline{\hat{k}}_x^i)^2 + (\underline{\hat{k}}_y^j)^2} \tag{2.29}$$

where $\underline{\underline{\tilde{\omega}}}^{ij}$ is the component of the matrix $\underline{\underline{\tilde{\omega}}}$ at the ith row and jth column. Let us define the matrices $\underline{\underline{\tilde{G}}}$ and $\underline{\underline{\hat{G}}}$ of size $N_\omega \times N_y$ and $N_x \times N_y$, respectively, such that

$$\begin{aligned} \underline{\underline{\tilde{G}}}^{\ell j} &= G(\underline{\tilde{k}}_{x,j}^\ell, \underline{\hat{k}}_y^j) \\ \underline{\underline{\hat{G}}}^{ij} &= G(\underline{\hat{k}}_x^i, \underline{\hat{k}}_y^j) \ . \end{aligned} \tag{2.30}$$

From this notation, it is clear that interpolation maps $\underline{\underline{\tilde{G}}}$ to $\underline{\underline{\hat{G}}}$. We use a Hamming-windowed sinc kernel $h(t, N_h)$ of size N_h for the interpolation:

$$\underline{\underline{\hat{G}}}^{ij} = \begin{cases} 0 & \mathcal{L}_{ij} = \emptyset \\ \sum\limits_{\ell \in \mathcal{L}_{ij}} \underline{\underline{\tilde{G}}}^{\ell j} h(\frac{1}{\Delta\omega}|\underline{\hat{\omega}}^\ell - \underline{\underline{\tilde{\omega}}}^{ij}|, N_h) & otherwise \end{cases} \tag{2.31}$$

where

$$\mathcal{L}_{ij} = \{\ell : \ 0 \le \ell \le N_\omega - 1, \ \ \frac{1}{\Delta\omega}|\underline{\hat{\omega}}^\ell - \underline{\underline{\tilde{\omega}}}^{ij}| \le N_h\} \tag{2.32}$$

and

$$h(t, N_h) = [0.54 + 0.46 \ \cos(\pi t/N_h)] \ \frac{\sin(\pi t)}{\pi t} \ . \tag{2.33}$$

Note that the interpolation from $\underline{\underline{\tilde{G}}}$ to $\underline{\underline{\hat{G}}}$ is actually performed in a 1-D manner between $\underline{\hat{\omega}}$ and $\underline{\underline{\tilde{\omega}}}$. Having denser samples in $\underline{\hat{\omega}}$, or larger N_ω, makes the interpolation more accurate. Also notice that as the squint angle increases, the irregularity in $\underline{\tilde{k}}_{x,j}$ increases. Hence, if the squint angle is large, we require more accurate 1-D interpolation.

2.3.3 Sampling requirements

The bandwidth of the data in the y dimension is, from (2.25),

$$\sigma_y = \frac{2}{c}\left(\omega_{max}\sin(\gamma_{max}) - \omega_{min}\sin(\gamma_{min})\right) \ . \tag{2.34}$$

Thus, the sampling interval in the along-track dimension must satisfy

$$\Delta y \leq \frac{\pi}{\sigma_y} \ . \tag{2.35}$$

From (2.19),

$$S(\omega, k_y) \approx A_1 \iint_{-\infty}^{\infty} g(x', y') e^{-jk_y y'} e^{-j\sqrt{4k^2 - k_y^2}\ x'}\ dx'\ dy' \ . \tag{2.36}$$

In the processing, we multiply $S(\omega, k_y)$ by the phase

$$\exp\left(jk_y Y_0 + j\sqrt{4k^2 - k_y^2}\ X_0\right) \tag{2.37}$$

which shifts the center of the resulting image to the center of the scene. Thus, considered as a function of ω, $S(\omega, k_y)$ is a superposition of exponentials of the form

$$\exp\left(j\theta(\omega)\right) = \exp\left(-j(x' - X_0)\sqrt{4k^2 - k_y^2}\right) \ . \tag{2.38}$$

The instantaneous frequency is

$$\begin{aligned} \nu_\omega &= \frac{d\theta(\omega)}{d\omega} = \frac{d}{d\omega}\left(-(x' - X_0)\sqrt{4k^2 - k_y^2}\right) = -\frac{2(x' - X_0)}{c}\frac{2k}{\sqrt{4k^2 - k_y^2}} \\ &= -\frac{2}{c}\,(x' - X_0)\,\frac{1}{\cos(\gamma_y')} \ . \end{aligned} \tag{2.39}$$

Define

$$\sigma_\omega = \max|\nu_\omega| \ . \tag{2.40}$$

The temporal frequency sampling interval must satisfy

$$\Delta\omega \leq \frac{\pi}{\sigma_\omega} \ . \tag{2.41}$$

Notice that the bound for $\Delta\omega$ depends on the offset $|x' - X_0|$ of a target in the scene. The farther a target is from the center of the scene in the cross-track direction, the smaller the temporal frequency sampling interval should be. The cosine term indicates that for a high squint angle, a smaller $\Delta\omega$ is necessary. Notice also that the bound given for $\Delta\omega$ is determined by the Nyquist criterion, which holds for evenly spaced samples that are infinite in extent. However, the interpolation step, which uses a finite set of samples separated by a distance of $\Delta\omega$, may require a smaller $\Delta\omega$ than dictated by (2.41) for accurate reconstruction.

2.3.4 Resolution

Resolution can be defined as in [39]. In the along-track, that is, the y direction, it is given as

$$\delta_y = \frac{2\pi}{k_{y_{max}} - k_{y_{min}}} \tag{2.42}$$

where

$$\begin{aligned} k_{y_{max}} &= 2\frac{\omega_{max}}{c}\sin(\gamma_{max}) \\ k_{y_{min}} &= 2\frac{\omega_{min}}{c}\sin(\gamma_{min}) \,. \end{aligned} \tag{2.43}$$

For the high squint angle, sine terms are close to unity. Hence for that case,

$$\delta_y = \frac{c\pi}{(\omega_{max} - \omega_{min})} \,. \tag{2.44}$$

From (2.10), the denominator is recognized to be $2\pi B_R$. Since B_R is approximately equal to B_T, we can write

$$\delta_y = \frac{c}{2B_T} \tag{2.45}$$

which is the well-known expression for range resolution of a radar. Notice that in the high-squint-angle case, the along-track direction is the range direction. This expression indicates that the range resolution is inversely proportional to the bandwidth of the radar signal.

Resolution in the cross-track direction is given as

$$\delta_x = \frac{2\pi}{k_{xmax} - k_{xmin}} \tag{2.46}$$

where

$$\begin{aligned} k_{xmax} &= 2\frac{\omega_{max}}{c}\cos(\gamma_{min}) \\ k_{xmin} &= 2\frac{\omega_{min}}{c}\cos(\gamma_{max}) \ . \end{aligned} \tag{2.47}$$

Thus,

$$\delta_x = \frac{c\pi}{(\omega_{max}\cos(\gamma_{min}) - \omega_{min}\cos(\gamma_{max}))} \ . \tag{2.48}$$

Resolution in the cross-track direction is dependent on the range of observation angles to the targets swept out as the radar moves along the flight path.

2.3.5 Software for point target imaging

We have implemented the $\omega - k$ algorithm in MATLAB with a graphical user interface (GUI) [76]. The part of the program that consumes most of the execution time is the interpolation. Thus, we implemented that part in C code and incorporated it into the main routine by using MATLAB's MEX-files . The GUI is a window called from MATLAB that consists of a number of list boxes, pop-up menus, text entries, and message boxes. The locations of the point target reflectors and parameters of the program can be edited, and the program can be run for the specified parameters and targets. When the program finishes, it displays the reconstructed image. Images can be displayed in a number of formats, and zooming is also possible.

The main window of the interface is shown in Figure 2.9. In the **Targets** section of the main window, the locations and the reflection coefficients of the point targets can be edited. The list box shows the current target locations (x and y coordinates relative to the scene center) and reflection coefficients. The values in the text boxes labeled as **x**, **y**, and **Reflection** can be added to the list, or the highlighted entry of the list may be replaced with these values by using the **Add** or **Update** buttons. The **Delete** button

removes the highlighted entry from the list. The **View** button is for producing a plot in which the locations (relative to the scene center) of the point reflectors are indicated by asterisks. The **Load** and **Save** buttons are intended to be used to load or save a list of targets from or to a specific file.

In the **Parameters** section of the main window, there is a list that shows the current parameters, their values and an explanation for each parameter. When an entry in the list is clicked and highlighted, the corresponding parameter name and its value appear in the text boxes, which are located just above the list. Then the value of the parameter can be changed by editing the value in the text box on the right. When either of the parameters for the center of the scene (X_0 or Y_0) are highlighted in the parameter list, the corresponding squint angle appears in the text box below the list on the right. The **Load** and **Save** buttons are intended for loading or saving the parameters from or to a file.

When there is an error in the editing process, either in the target or parameter section, such as not entering a numeral value for a parameter, an error message is displayed in the message box at the very bottom of the window.

After the targets and the parameters are edited, the algorithm can be run for the target and parameter values shown in the list boxes by clicking the **Run** button. When the processing finishes, the reconstructed image is displayed in a figure window in **Color Image** format. It is also possible to obtain a **Gray Image** or **Contour Image** by selecting from the pop-up menu in the bottom right corner of the main window. Selecting the option **Grid**, toggles the grid of the plot. Zooming is possible by choosing **Zoom** from the pop-up menu and then clicking on the desired area of the image.

2.3.6 Simulation results and discussion

To evaluate the feasibility of the $\omega - k$ algorithm for runway imaging, we simulated several example scenarios. In these examples, the temporal center frequency of the radar signal was 10 GHz and the bandwidth was 32 MHz. The radar traveled $L_a = 500$ m along track and illuminated a scene area of $L_x = 120$ m by $L_y = 500$ m.

In Figure 2.10 we see the results of a simulation where targets are at $(160, 3100)$, $(180, 3200)$, $(200, 3300)$, and $(220, 3400)$; all numbers are in meters. The scene center is at $(200, 3200)$; hence, the squint angle $\gamma_0 = 86.42°$. In Figure 2.10, images of targets are reconstructed at their correct locations. In Figure 2.11, without changing the positions of the targets relative to the scene center, we moved the scene center to $(60, 3200)$, which corresponds to a squint angle of $\gamma_0 = 88.93°$, and the new locations of the targets are $(20, 3100)$, $(40, 3200)$, $(60, 3300)$, and $(80, 3400)$. As the squint angle approaches $90°$ for targets nearer the runway center, the targets appear smeared out with energy smeared toward the center of the scene in the reconstructed image. The dashed line at $x = 76.2$ m is the edge of the FAA zone[2]. For these simulations the number of temporal samples N_ω was held constant at 1024. Notice that the condition (2.41) was satisfied with $N_\omega = 1024$ for all targets except the target at $(20, 3100)$. To satisfy that condition we took $N_\omega = 1536$. The result of the simulation with the increased number of samples is shown in Figure 2.12. Although the condition (2.41) has been satisfied, there are still certain aberrations. This suggests that the interpolation is not fine enough. As we increase N_ω, the interpolation will become more accurate as described in Section 2.3.2. The computational cost of interpolation increases only linearly with increasing N_ω. In Figures 2.13 and 2.14, N_ω was increased to 3072 and 6400, respectively. There is some improvement in the reconstruction because of the finer interpolation, but beyond some point, finer interpolation will not help because the target is located close to the center of the runway, so that the range of observation angles is very narrow. As an extreme case, another simulation was performed for a point target at the center of the runway, with $\gamma_y' = 90°$. We added a point target at $(0, 3000)$ to the previous set of targets and used $N_\omega = 6400$. The result is shown in Figure 2.15, where it is seen that the new target is not properly reconstructed; instead its energy is distributed across the cross-track dimension. This is predicted by the resolution formula in (2.48). We expect a similar reconstruction for targets that are anywhere near the center of the runway. This is not a problem for the runway imaging application, however, because targets on or very close to the runway need not be imaged with high resolution. An indication of their existence

[2]Recall that FAA regulations require that aircraft and vehicles maintain a distance of 76.2 m (250 ft) from the center of the runway when they do not have clearance to proceed to the runway.

is sufficient, which occurs in Figure 2.15. On the other hand, targets should not appear outside the FAA zone if they are actually inside. Our simulations, above, show that with accurate interpolation this is not a problem. Targets outside the FAA zone should not appear inside and cause a false alarm, which, of course, is a less hazardous case. From the simulations, it is seen that targets that are inside the FAA zone but not close to the runway center are accurately imaged. Objects outside the FAA safety zone will be imaged with even higher resolution, virtually eliminating the possibility of a false alarm.

2.4 Comparison of the $\omega - k$ Algorithm with GIM

In this section, we investigate an alternative algorithm that accurately models the wavefront. This is a general inversion method suggested for the numerical solution of the Fredholm integral equation of the first kind [74]. We call this particular method GIM, and present an outline of the method in Appendix E. This method, which was originally applied to borehole induction measurements, has been formulated for strip-mapping SAR [75]. By a modification of the kernel, it is also possible to formulate it for spotlight-mode SAR. Both the $\omega - k$ algorithm and GIM have been suggested for runway imaging [67]. Here we make an extensive comparison between the performances of the $\omega - k$ algorithm and GIM for the runway imaging scenario. The basic motivation behind our attempt to compare these two algorithms is the following: Even though it seems to be computationally attractive, the $\omega - k$ algorithm may not present the optimal solution to the highly squinted SAR imaging problem. We, therefore, consider using another, more general, algorithm, namely GIM, that accurately models the wavefront curvature. The $\omega - k$ algorithm decomposes the imaging kernel in a Fourier basis, while GIM makes a similar decomposition in a more general orthogonal basis. This might possibly provide a more efficient is a better representation of the data. Hence, GIM might be expected to produce reconstructions with less severe target-location dependent aberrations.

In this study, our objective is to make a comparison between the image reconstruction performances of the $\omega - k$ algorithm and GIM for squint angles close to 90 degrees. Since the performance of the $\omega - k$ algorithm can be improved by increasing the complexity of

the interpolation, a fair comparison will allow each method to use the same number of computations and then compare the resulting image quality.

2.4.1 GIM processing

The GIM performs a 2-D inversion by exploiting the fact that any finite energy kernel can be approximated arbitrarily closely by means of a kernel of finite rank where the approximation is in the metric of the space of square summable complex-valued functions [77]. In the processing, measurements are first projected onto the subspace containing the measurement kernel and then the measurement integral is represented in a multichannel convolution form by a finite rank kernel approximation. Solving the multichannel convolution problem by a regularized inversion scheme, such as regularized least squares estimation [78], and back-projecting gives an estimate of the reflectivity which is the image of the scene. Because of the projection onto the kernel subspace, this method is inherently robust to additive noise. On the other hand, inversion of the multichannel convolution, which is an ill-posed problem, requires regularization which, with all the other operations, increases the amount of computation. But certain parts of the computation can be performed off-line. The performance of the method depends primarily on the regularized inversion scheme used for the solution of the multichannel deconvolution problem. The method is described in detail in Appendices E and F.

2.4.2 Simulation results and discussion

Here, we compare the reconstruction performance of the two methods under the condition that the $\omega - k$ and GIM algorithms use the same number of computations. Therefore, we first elaborate on the computational cost of the methods. The computational complexity of the $\omega - k$ algorithm can be easily calculated from Figure 2.6. We have $N_\omega \times N_a$ samples of the return signal, $s(\omega, y)$. The Cartesian interpolation grid consists of $N_x \times N_y$ points. In the interpolation step, the number of multiplications is at most $N_h N_x N_y$ where N_h is the length of the window used in the interpolation. Thus, the total number of (complex) multiplications is given by $N_\omega N_a + N_\omega N_a log_2 N_a + N_\omega N_a + N_x N_y (log_2 N_x + log_2 N_y) + N_h N_x N_y$. The various terms are for the first phase multipli-

cation, 1-D FFT, second phase multiplication, interpolation and 2-D IFFT, respectively. In GIM, the quantities given by (F.6), (F.8) and (F.13) can be precomputed because of their dependence only on the transmitted pulse and the data collection geometry. The computation of the multichannel deconvolution filter can be done off-line as well. Thus, the required number of (complex) multiplications, once the off-line computations have been completed, is $IN_tN_a + [(N_aI + M)N_a log_2 N_a + MN_aI] + MN_yN_x$, corresponding to (F.7), (F.15) and (F.16), respectively. Here, N_t is the number of spatial samples in the x direction for the range compressed return signal given in (F.3).

In the following simulations, the temporal center frequency of the radar signal was 10 GHz, and the bandwidth was 32 MHz. The radar traveled 500 m along track and illuminated a scene area of 120 m by 500 m. Considering the sampling requirements, we let $N_t = 128$ and $N_a = 256$. After running GIM for a simulation with $N_x = N_y = 128$, we obtained I and M values and calculated $N_\omega = 6912$ which made the number of computations for both algorithms equal. With that number of temporal frequency samples, the interpolation step in the $\omega - k$ algorithm is accurate [79].

Figure 2.16(a) shows the image reconstructed by GIM, where the actual locations of the simulated point targets are $(0, 3000)$, $(20, 3100)$, $(40, 3200)$, $(60, 3300)$, and $(80, 3400)$; all numbers are in meters. Notice that the target at $(0, 3000)$ is at the center of the runway. For this simulation there was no measurement noise in the return signal. The scene center is at $(60, 3200)$, which corresponds to a squint angle of $\gamma_0 = 88.93°$. The dashed line at $x = 76.2$ m is the edge of the FAA zone. The corresponding image obtained by the $\omega - k$ algorithm is given in Figure 2.16(b). In the $\omega - k$ reconstruction, the sidelobes are at least 12 dB below the mainlobe. Those for the GIM reconstruction are at least 13 dB below the mainlobe. The reason for the variety of target positions is that we wished to investigate the image reconstruction performance as a function of target location, especially in the cross-track direction. In both of the reconstructions, targets relatively far away from the center of the runway are reconstructed at their correct locations. For the target at the center of the runway, the $\omega - k$ reconstruction has a narrow mainlobe but it is shifted from its true location. In the GIM reconstruction, the mainlobe peak is located at $x = 0$ but it is much wider; hence, it is not possible to detect the location accurately. However, in runway imaging, targets on or very close to the runway need

not be imaged with high resolution. An indication of their existence in the FAA zone is sufficient, which occurs in Figure 2.16. We notice spreading of the energy of the target in the cross-track dimension, but this is expected since the range of observation angles for on-the-runway targets is exceedingly small.

We also performed simulations for the case with measurement noise in the return signal, assuming additive white Gaussian noise. Notice that for the noisy case, the Equations (2.12), (F.1), (F.3), (F.9), and (F.12) must be appended with additive noise terms as in Appendix E. Figure 2.17(a) is a reconstruction by GIM. In this simulation, the signal-to-noise ratio (SNR) was 30 dB. The weakest reconstructed target image has sidelobes that are about 9 dB below the mainlobe. The corresponding $\omega - k$ reconstruction is not shown since the targets were not identifiable in the image. However, for a less noisy case of 40 dB SNR, the reconstruction is shown in Figure 2.17(b). The weakest target has sidelobes that are about 8 dB lower than the mainlobe.

As seen from the above simulations, the $\omega - k$ algorithm and GIM produce comparable reconstructions for the noiseless case. Under the constraint that both methods use the same number of computations, interpolation in the $\omega - k$ algorithm is accurate enough so that no aberrations pertaining to the inaccuracies of the interpolation step occur. GIM is more robust to noise as seen from the simulations, which could be of value in some scenarios. Recall, however, that for GIM we did not factor in some computations that we assumed could be performed prior to data collection, off-line. If the geometry for data collection is not known a priori, then these additional computations must be performed online, which would greatly add to the complexity of GIM.

2.5 Resolution of the Left-Right Ambiguity

The runway imaging problem requires resolution of the left-right ambiguity. The reason that such an ambiguity arises is that the radar works on a ranging principle. Two different point targets at equal distances from the radar and opposite displacements from the runway centerline will produce exactly the same set of radar return signals and, therefore, will be mapped to the same location in the image. Since the antenna beam is not totally zero outside the main beam, or the spotlighting may not be performed

precisely within the large main beam of the antenna, there may be contributions from the left side of the runway when the antenna squinted to the right (but looking almost straight ahead) and vice versa. In that case, objects on the left and right sides of the runway are together at the same locations in the radar image. Interferometry can be used to obtain more diverse information about the location of the targets. This amounts to using another antenna, let us say, antenna B, in addition to the former antenna, which will be indexed by A. If the antennas are at different distances from the flight path (centerline), then the radar return will arrive at one of the antennas before the other. Basically, the phase difference between the two antennas will indicate if the target is on the left or right. Due to operational considerations, it may be desirable to have antenna B only receive.

To simplify matters, we assume the main beams of both antennas uniformly illuminate the same area on the ground. Suppose that antenna B is mounted at a distance X_B from antenna A in the positive x direction. The radar return is given by (2.12) and reproduced here for antenna A as follows:

$$s_A(\omega, y) = \iint_{-\infty}^{\infty} g(x', y')\ f_A(x', y - y'; \omega)\ dx'dy' \ . \tag{2.49}$$

where the imaging kernel and the radar return for antenna A are denoted by $f_A(x', y; \omega)$ and $s_A(\omega, y)$, respectively. Similarly, denote the respective quantities for antenna B by $f_B(x', y; \omega)$ and $s_B(\omega, y)$ where y is the location of the aircraft along its flight path and (x', y') is the location of a reflector in the scene. A similar equation then holds for $s_B(\omega, y)$ and $f_B(x', y; \omega)$. The imaging kernels can be written as

$$\begin{aligned} f_A(x', y - y'; \omega) &= e^{-j2k\sqrt{x'^2 + (y'-y)^2}} \\ f_B(x', y - y'; \omega) &= e^{-j\left[k\sqrt{x'^2 + (y'-y)^2} + k\sqrt{(x'-X_B)^2 + (y'-y)^2}\right]} \ . \end{aligned} \tag{2.50}$$

We have

$$\sqrt{(x' - X_B)^2 + (y' - y)^2} = \sqrt{(y' - y)^2 + x'^2 - 2x'X_B + X_B^2} \tag{2.51}$$

$$= \sqrt{(y'-y)^2+x'^2}\left[1+\frac{X_B^2-2x'X_B}{(y'-y)^2+x'^2}\right]^{\frac{1}{2}} \tag{2.52}$$

$$\approx \sqrt{(y'-y)^2+x'^2}\left[1+\frac{1}{2}\frac{X_B^2-2x'X_B}{(y'-y)^2+x'^2}\right] \tag{2.53}$$

$$= \sqrt{(y'-y)^2+x'^2}+\frac{X_B^2}{2\sqrt{(y'-y)^2+x'^2}}-\frac{x'X_B}{\sqrt{(y'-y)^2+x'^2}} \tag{2.54}$$

where the approximation is made by discarding the second- and higher-order terms of the Taylor series, [80],

$$\sqrt{1+x} = 1+\frac{1}{2}x-\frac{1}{8}x^2+\frac{1}{16}x^3+\ldots\,, \quad |x|\leq 1\,. \tag{2.55}$$

Then,

$$f_B(x',y-y';\omega) = e^{-j2k\sqrt{x'^2+(y'-y)^2}}\, e^{-jk\frac{1}{2\sqrt{(y'-y)^2+x'^2}}X_B^2}\, e^{jk\frac{x'}{\sqrt{(y'-y)^2+x'^2}}X_B} \tag{2.56}$$

$$= f_A(x',y-y';\omega)\, e^{-jk\frac{1}{2\sqrt{(y'-y)^2+x'^2}}X_B^2}\, e^{jk\frac{x'}{\sqrt{(y'-y)^2+x'^2}}X_B}\,. \tag{2.57}$$

For the runway imaging case, we can make the following approximation

$$\sqrt{(y'-y)^2+x'^2} \approx \sqrt{y'^2+x'^2}\,. \tag{2.58}$$

Inversion of the return data $s_A(\omega,y)$ and $s_B(\omega,y)$ will yield the complex reflectivity function estimates $g_A(x,y)$ and $g_B(x,y)$, respectively, where we can replace the wavenumber k with a constant k_c in the case of a narrow-band radar. The approximations employed above do not affect the quality of the reconstructed image since they are used solely for interpretation of the side information provided by a second antenna. The conjugate product of the complex images yields

$$g_A(x',y')g_B^*(x',y') = |g(x',y')|^2\, e^{jk_c\frac{1}{2\sqrt{y'^2+x'^2}}X_B^2}\, e^{-jk_c\frac{x'}{\sqrt{y'^2+x'^2}}X_B}\,. \tag{2.59}$$

If we assume that the antenna is squinted to the right, the arguments of the complex images $g_A(x',y')$ and $g_B(x',y')$ refer to the positive coordinates no matter what the sign

of x' actually is. (Putting absolute value signs around the x' arguments on the left-hand side of the above equation will make them mathematically correct.) This is because in the reconstruction, all the targets to the left of the runway appear on the right (with positive cross-track locations). The first exponential term in (2.59) is already known given the (x', y') coordinates of a pixel in the image. Alternatively, multiplying $s_B(\omega, y)$ by $\exp\left(jk\frac{1}{2\sqrt{X_0^2+(Y_0-y)^2}}X_B^2\right)$ and processing the resulting data compensates for that term. In that case, there is no need for approximating k by k_c; however, x' and y' would then be approximated by the scene center values X_0 and Y_0, respectively. Let us denote the resulting complex image after the compensation as $g_R(x', y')$, given by

$$g_R(x', y') = |g(x', y')|^2 \, e^{-jk_c\frac{x'}{\sqrt{y'^2+x'^2}}X_B} . \tag{2.60}$$

The sign of the phase in the exponential is dependent on the sign of x', which indicates whether the target is to the left or right of the runway. The phase is positive if the target is to the left and negative if the target is to the right.

2.5.1 Simulation results and discussion

Figure 2.18 shows the $\omega - k$ reconstruction of point targets at locations $(-40, 3000)$, $(20, 3100)$, $(40, 3200)$, $(60, 3300)$, and $(80, 3400)$. Notice that the target at $(-40, 3000)$ is reconstructed at $(40, 3000)$. This image is the magnitude of $g_A(x', y')$. After processing the data from antennas A and B according to the method outlined above, we obtain the phase image shown in Figure 2.19. This corresponds to the phase of (2.60). This image is median filtered to eliminate outliers due to phase errors or phase wrapping [81–83]. Only the positive phase values are plotted, indicating a target to the left of the runway. The extension of sidelobes appear in the top portion of the image since the image domain is periodic with the size of the image due to FFT processing. The result is clearly an indication of a target to the left of the runway in the along-track dimension $y' = 3000$, but it is not apparent, from this phase image alone, where the target is actually located in the cross-track dimension. This is because the phase associated with the amplitude of the complex image does not taper off as the amplitude does in the side lobes and away from the main lobe. That is why, while there is very small energy smeared throughout the

cross-track dimension for the target at $(-40, 3000)$ in Figure 2.18, the associated phase in the corresponding small-energy areas are not small in amplitude. It is, therefore, a useful idea to use the amplitude image in Figure 2.18 together with the phase image. The phase image can simply be masked with the amplitude image using pixel-by-pixel multiplication. This will clearly indicate the location of the targets. A so-formed image corresponding to the image in Figure 2.19 is shown in Figure 2.20.

To check that the proposed solution of left-right ambiguity works well when the target is on the right instead of the left, we placed the target at $(40, 3000)$ in another simulation. The phase image after processing is shown in Figure 2.21. Except for a few localized errors, this almost empty image is what we expected. Those few errors can be eliminated by using a larger median filter. As a second check of our software, we placed antennas A and B at the same location, that is, $X_B = 0$. In that case, we correctly obtained an all-zero phase image.

To test this procedure when there are two targets at symmetrical locations with respect to the runway, we placed a target at $(40, 3000)$ and another at $(-40, 3000)$. The resulting processed phase image is shown in Figure 2.22. In comparison with Figure 2.21, this is clearly an indication of a target on the left side. The difference between this image and the image in Figure 2.19 is that the positive phase due to the target at $(-40, 3000)$ has been combined with the negative phase due to the target at $(40, 3000)$.

The above simulations used a second antenna separated by a half meter from the main antenna. For larger separations, phase unwrapping [40] is necessary. Notice that as the separation of the antennas increases, the approximations involved in expressing $f_B(x', y; \omega)$ in terms of $f_A(x', y; \omega)$ become less accurate. This induces other limitations on the distance by which the two antennas can be separated.

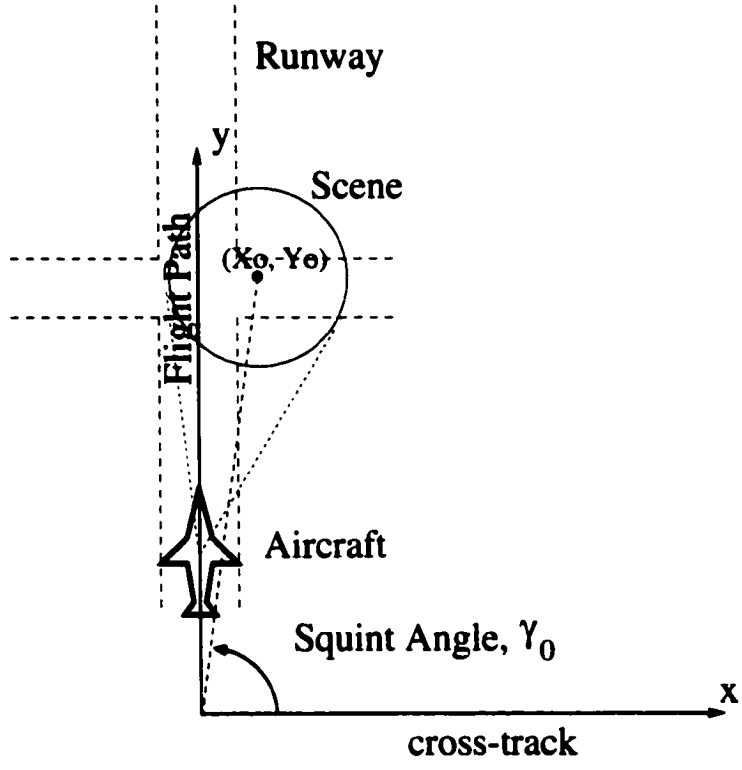

Figure 2.1 Geometry of synthetic aperture radar data collection for runway imaging.

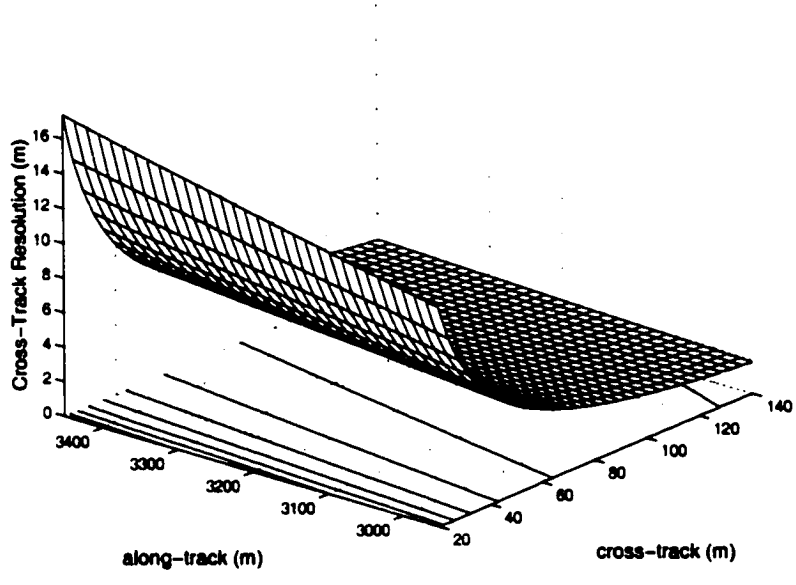

Figure 2.2 Cross-track resolution at each location in the scene. Scene center is at (60, 3200). The radar bandwidth is 32 MHz centered around 10 GHz. Synthetic aperture length is 500 m.

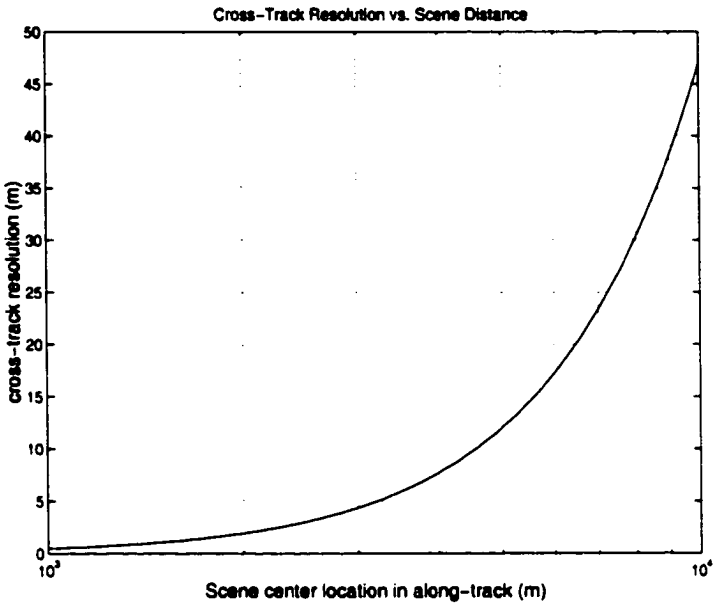

Figure 2.3 Cross-track resolution versus scene distance (along-track location of the scene center). The radar bandwidth is 32 MHz centered around 10 GHz. Synthetic aperture length is 500 m.

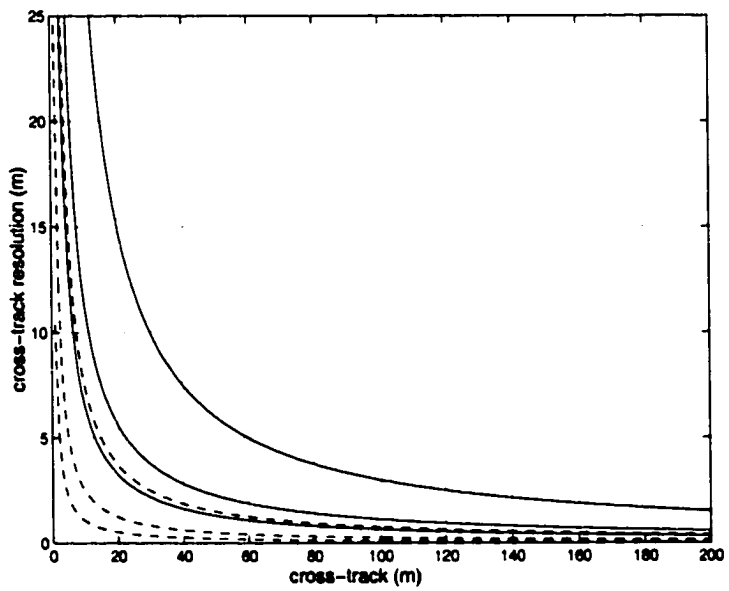

Figure 2.4 Plots showing cross-track resolution as a function of cross-track location of a point target for different synthetic aperture lengths. The along-track location y' of the target is 3200 m for the solid curves and 1600 m for the dashed curves. In both sets of curves, from top to bottom, curves are for synthetic aperture lengths 500 m, 1300 m and 2100 m, respectively. The radar bandwidth is 32 MHz centered around 10 GHz.

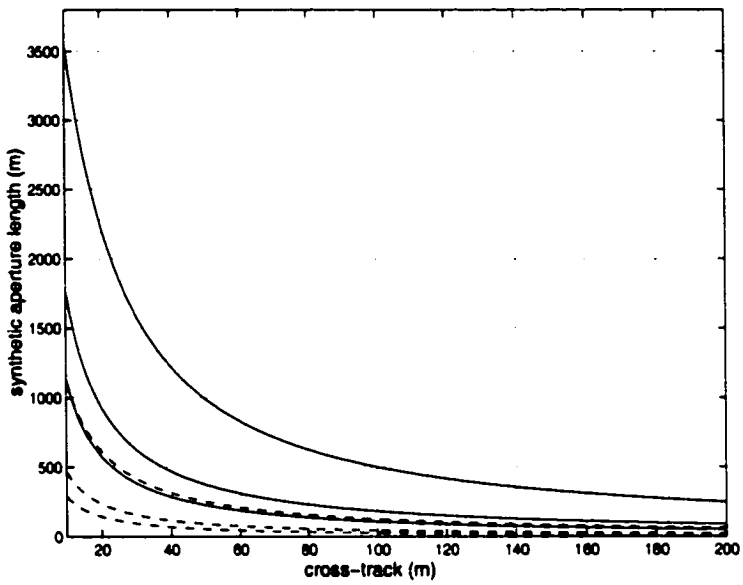

Figure 2.5 Plots showing synthetic aperture length as a function of cross-track location of a point target for different cross-track resolutions. The along-track location y' of the target is 3200 m for the solid curves and 1600 m for the dashed curves. In both sets of curves, from top to bottom, curves are for resolutions 3 m, 8 m and 13 m, respectively. The radar bandwidth is 32 MHz centered around 10 GHz.

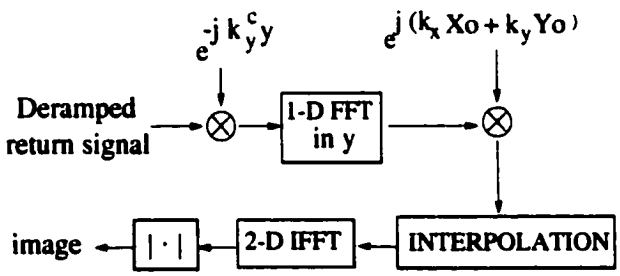

Figure 2.6 Block diagram of $\omega - k$ algorithm.

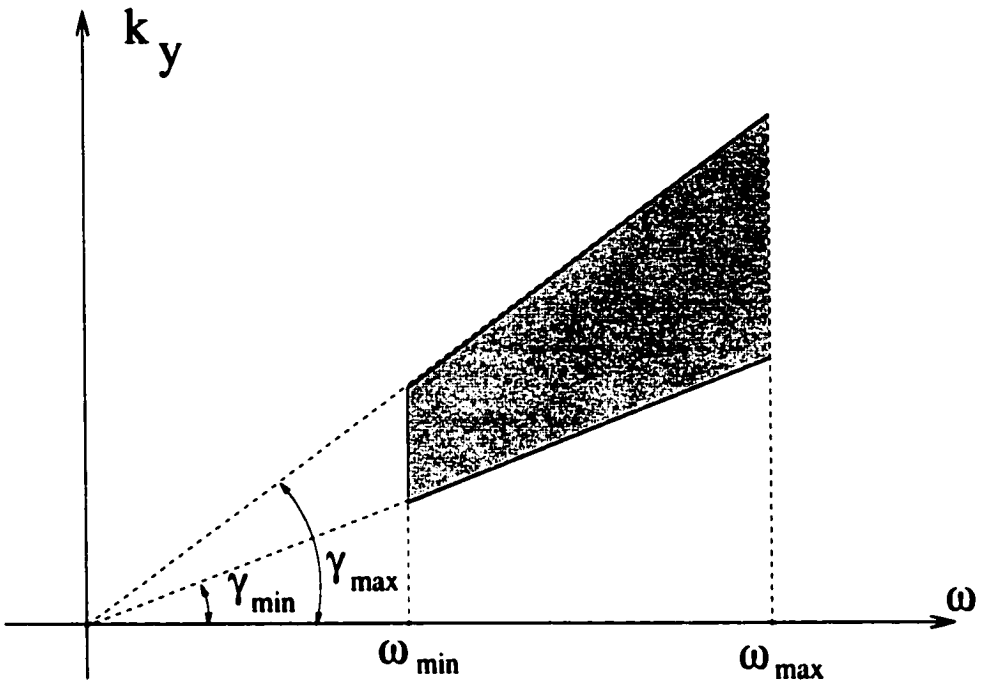

Figure 2.7 Fourier data on $\omega - k_y$ plane.

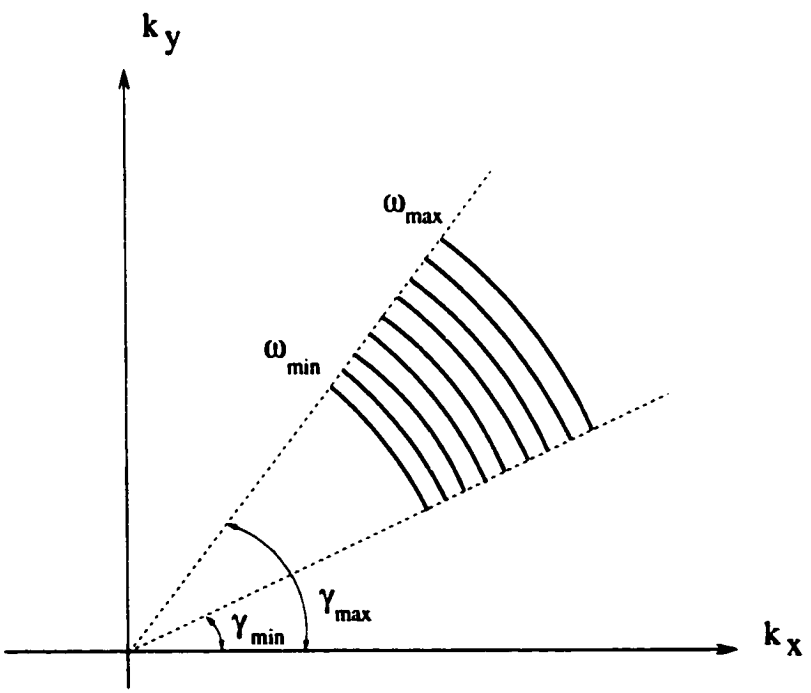

Figure 2.8 Fourier data on $k_x - k_y$ plane.

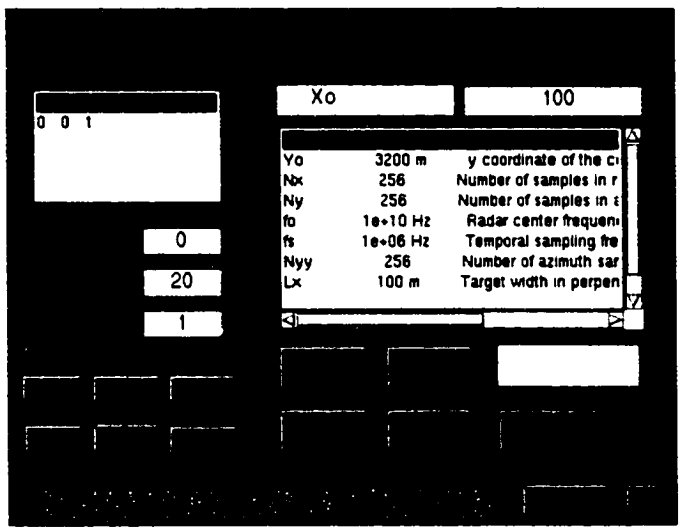

Figure 2.9 Main window of the graphical user interface.

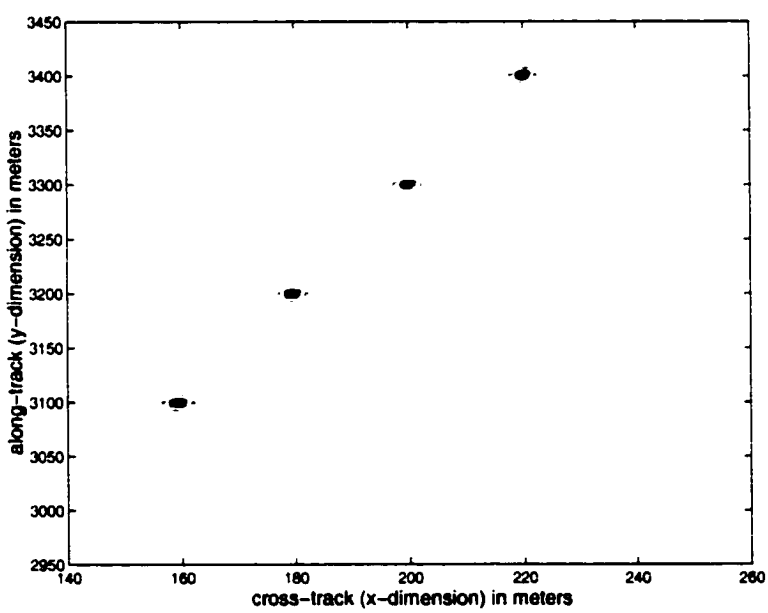

Figure 2.10 $\gamma_0 = 86.42°$, $N_\omega = 1024$.

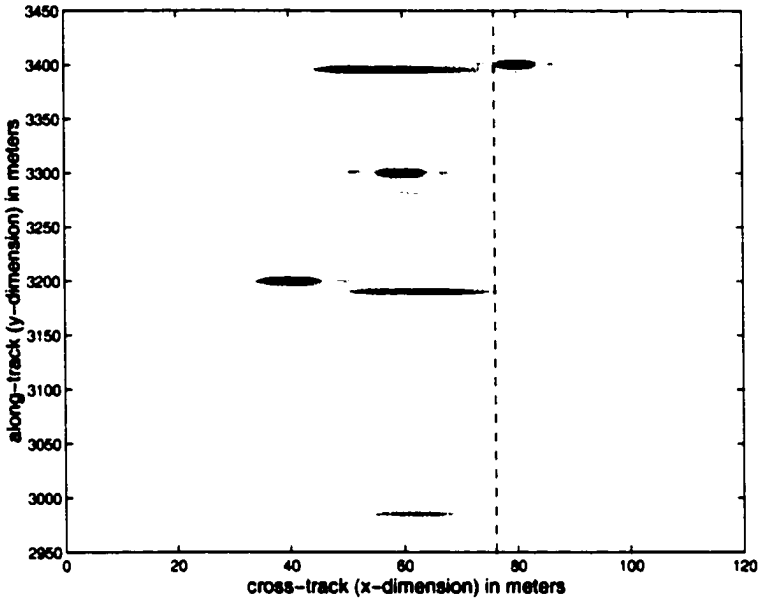

Figure 2.11 $\gamma_0 = 88.93°$, $N_\omega = 1024$.

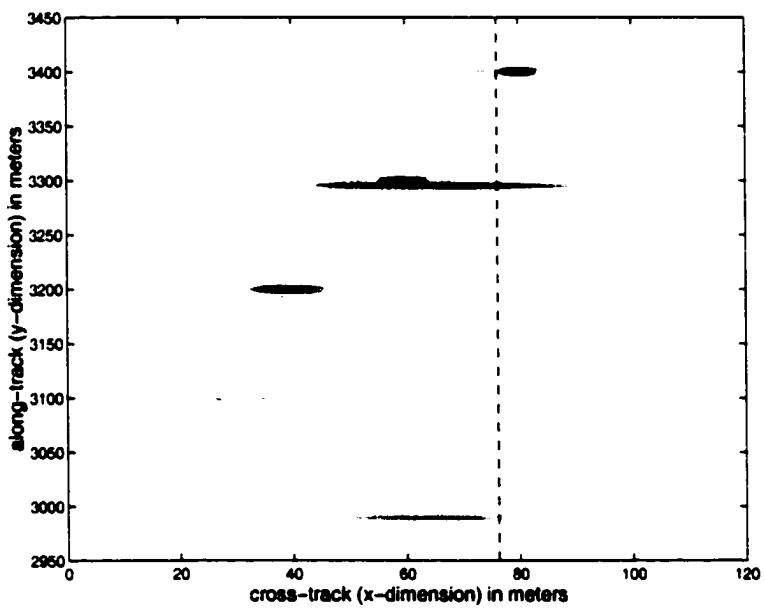

Figure 2.12 $N_\omega = 1536$.

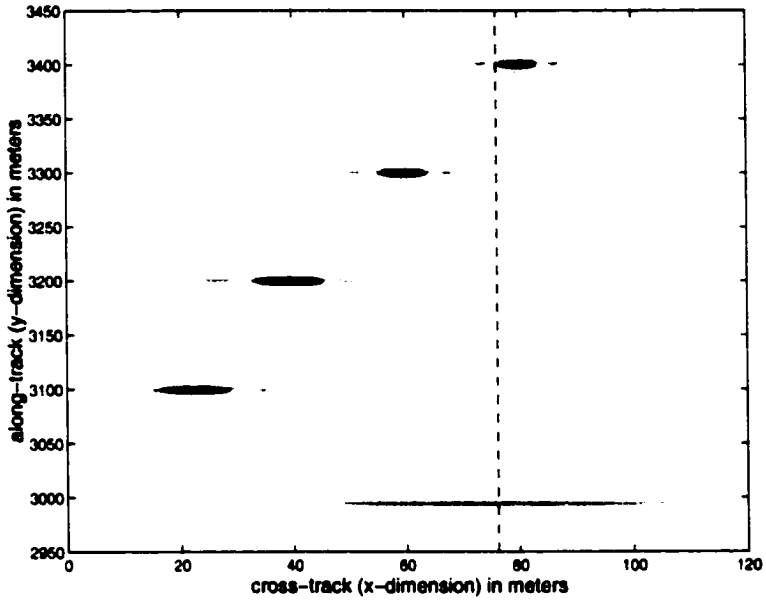

Figure 2.13 $N_\omega = 3072$.

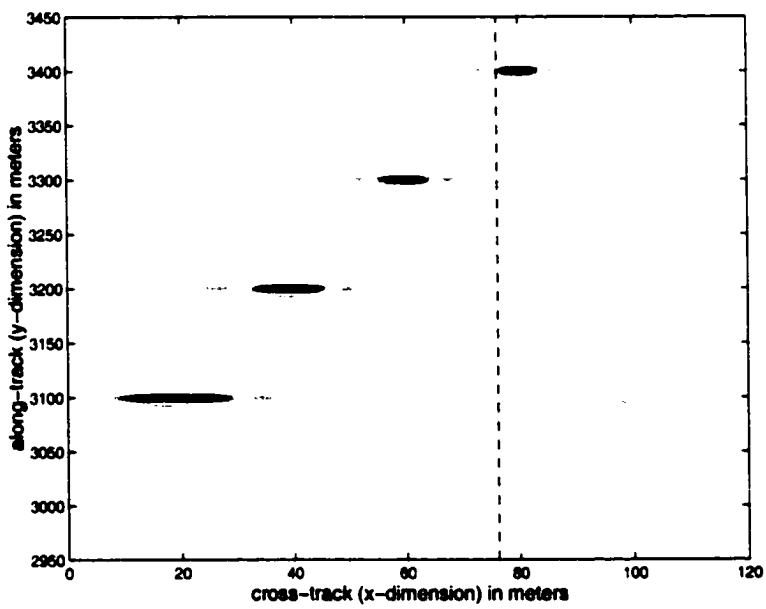

Figure 2.14 $N_\omega = 6400$.

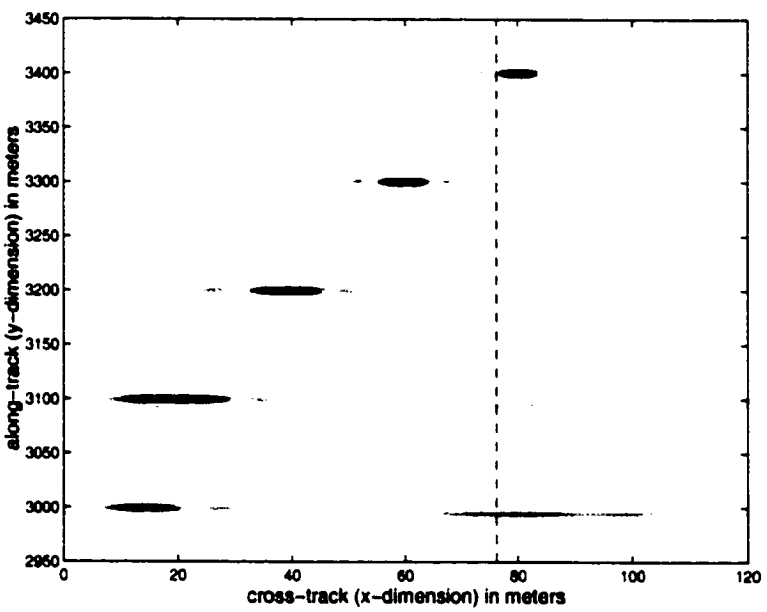

Figure 2.15 Additional target at the center of the runway, $N_\omega = 6400$.

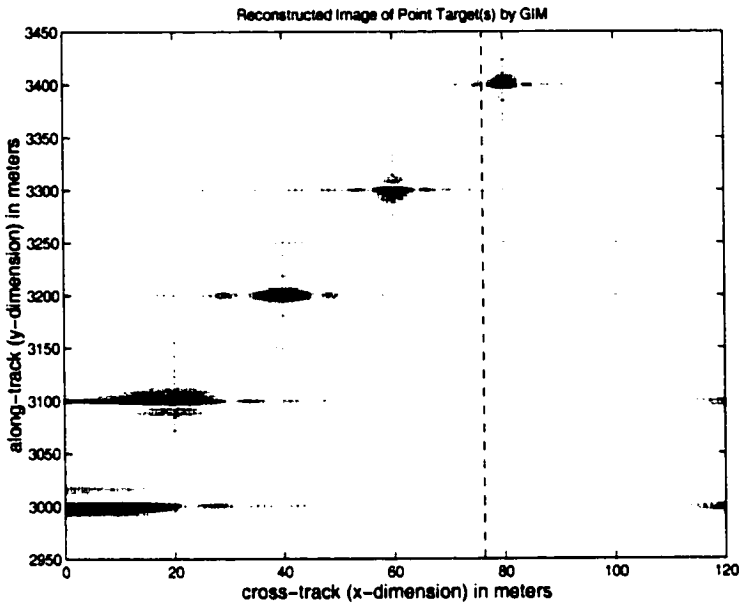

(a)

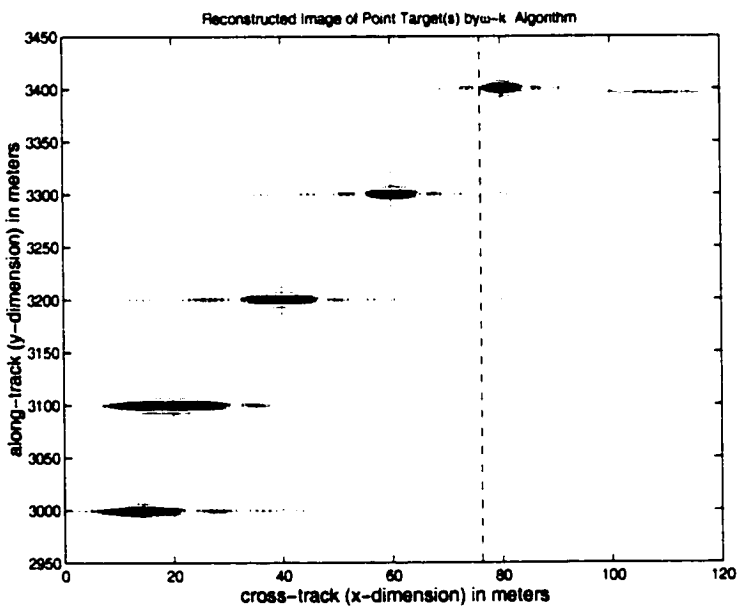

(b)

Figure 2.16 Image of point targets reconstructed by (a) GIM, and (b) $\omega - k$ algorithm. No noise.

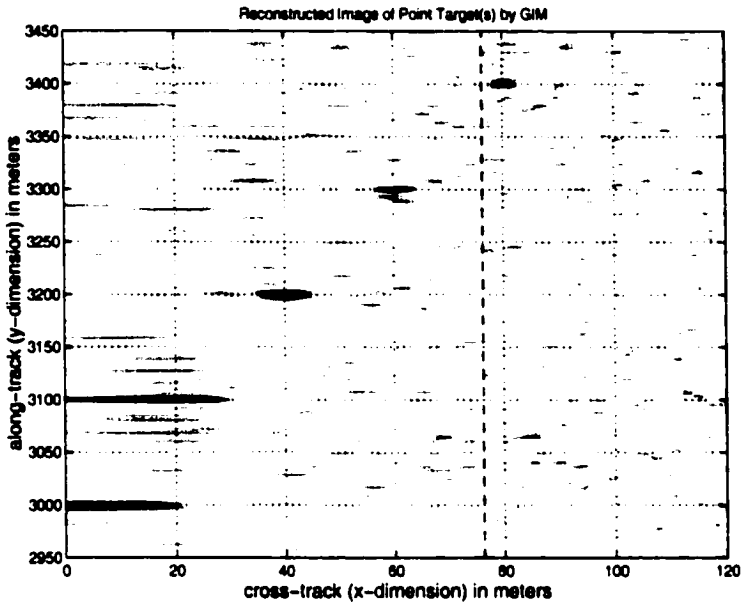

(a)

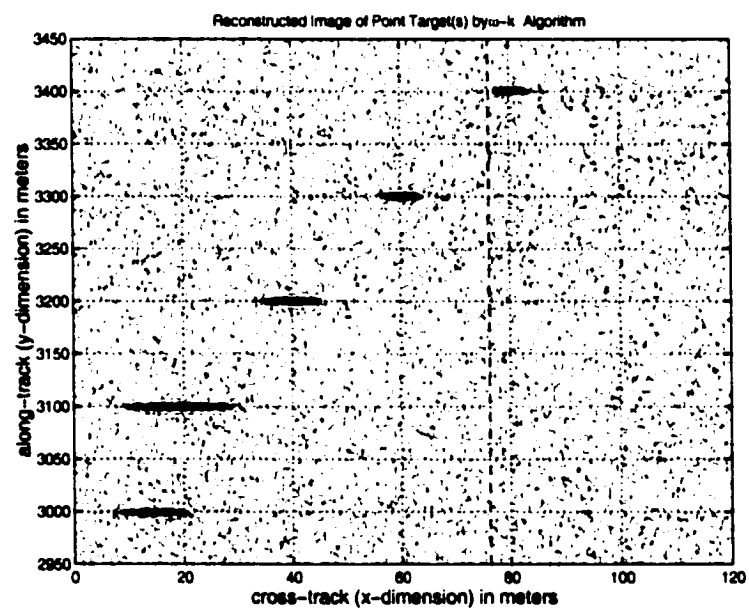

(b)

Figure 2.17 Image of point targets reconstructed by (a) GIM for SNR = 30 dB, and (b) $\omega - k$ algorithm for SNR = 40 dB.

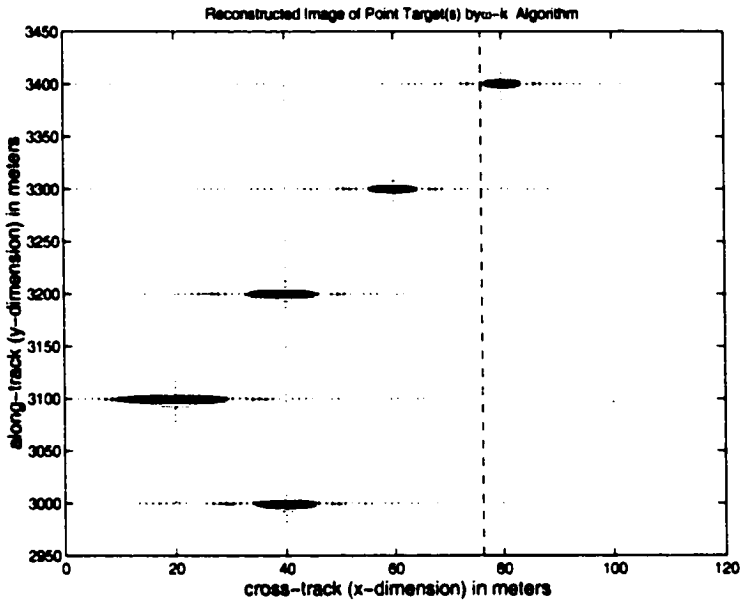

Figure 2.18 SAR image of a scene formed by the $\omega - k$ algorithm. The target which appeared at $(40, 3000)$ is actually at $(-40, 3000)$.

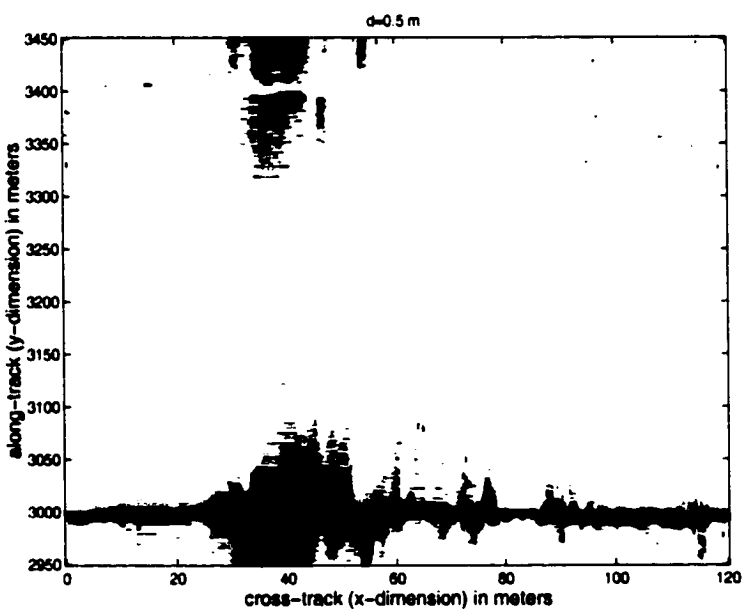

Figure 2.19 Positive phase image of (2.60) after median filtering. The test target is at $(-40, 3000)$.

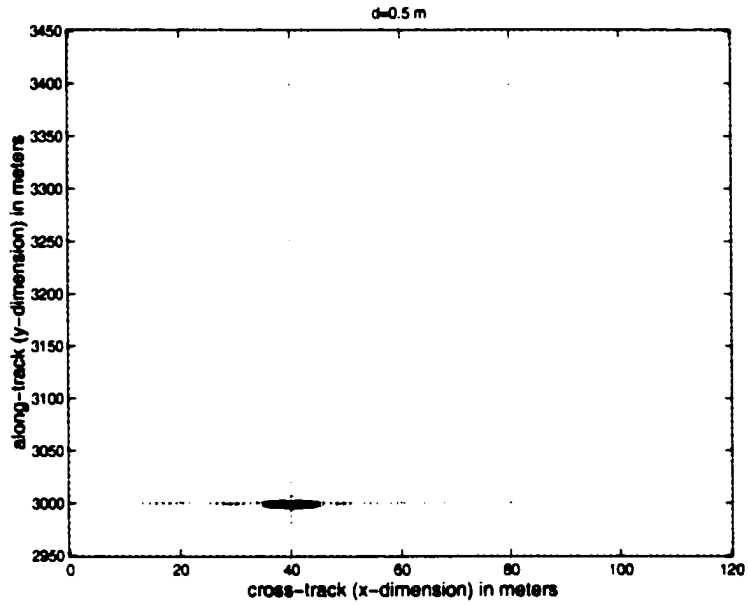

Figure 2.20 Amplitude masked phase image corresponding to the image in Figure 2.19.

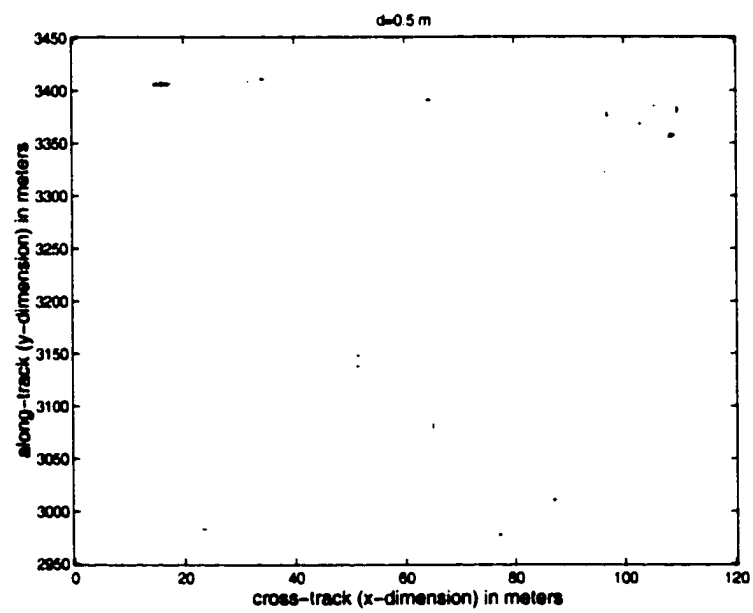

Figure 2.21 Positive phase image of (2.60) after median filtering. The test target is at $(40, 3000)$. No targets on the left of the runway.

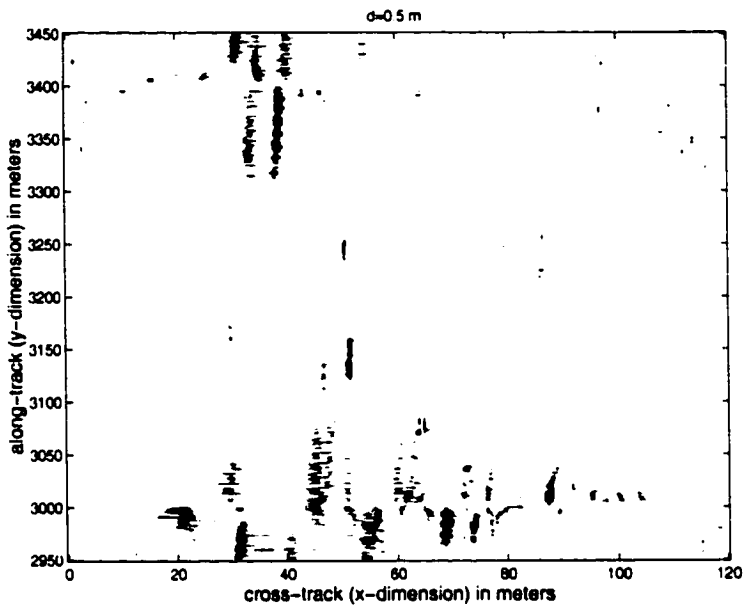

Figure 2.22 Positive phase image of (2.60) after median filtering. The test targets are at $(40, 3000)$ and $(-40, 3000)$.

CHAPTER 3

ACOUSTIC IMAGING OF OBJECTS BURIED IN SOIL

3.1 Introduction

Once a cultural or archaeological resource site is identified, it must be assessed in order to determine its significance and eligibility for the National Registry of Historic Places. Current methods for this assessment involve scattered small-scale digs at the site, which are expensive and imprecise. The cost of complete assessments is prohibitive; therefore, there is an urgent need to significantly reduce the cost of data recovery, especially for the many sites having lower probabilities of containing significant cultural or archaeological resources. In this study, we apply synthetic aperture theory to an acoustic system for high-resolution imaging of buried artifacts. In addition to finding cultural artifacts, a system designed to image buried objects possibly could be adapted to detect land mines.

An acoustic system has potential advantages over existing imaging modalities. Current technologies in seismic exploration and borehole techniques are not designed to meet the resolution requirements for imaging cultural artifacts or land mines. A study showed that, using acoustic techniques for subsurface imaging, resolution could be improved from tens of meters achievable in petroleum and mineral exploration to on the order of 1 m using geophysical tomography (boreholes) for applications such as finding buried waste or abandoned mines [84]. However, finding cultural artifacts will require resolution on the order of 5 cm.

Ground-penetrating radar (GPR) has had some success in identifying underground structures; however, the success is site specific, depending on the moisture content of the soil [85]. It has been shown that GPR is effective in dry soil, but that water attenuates the electromagnetic energy. Conversely, acoustic energy propagates better in a saturated medium than in dry soil [86]. Thus, an acoustic system would complement a GPR system.

3.2 Experimental System

A picture of the system is shown in Figure 3.1. This system was designed and constructed by Professor William D. O'Brien, Jr., and his students. The soil is contained in a cubic wooden box of 1.2 m on a side. The box has a false bottom, with only the top 60 cm filled with soil. The system incorporates a torpedo transducer array from the Applied Research Laboratory at Pennsylvania State University. The torpedo head, which contains the receiver array, is suspended above the box by a metal frame that surrounds the box. The source is to the right of the torpedo head. Sitting on top of the box of soil is a child's pool filled with 3 cm depth of water. The water is used to couple the sound energy between the transducers and the sand since the transducers are designed for underwater applications. To the right of the frame are two computers which are used to control the motion of the receiver array along three translational axes and the data acquisition.

The source transducer is a single element that is well approximated as a point source. In the torpedo head, a 52-element sonar array serves as the receive array and allows for beamforming on receive. In future versions of the system, a transmitter array may be used to provide focusing of the transmit beam to increase the energy coupled into a localized volume of soil, thereby improving SNR. In a recent study both the transmitter and the receiver array use focused beams [87].

The receiver array and the corresponding coordinate system are depicted in Figure 3.2. The z axis represents the depth into the soil and the x-y plane represents the soil surface. The y and z dimensions are called *azimuth* and *range*, respectively. The detailed geometry of the transmitter and the receiver is shown in Figure 3.3. Due to the size of the torpedo and the source, the smallest possible center-to-center spacing of the source and receiver array is 33 cm.

The excitation signal is a cosine-weighted pulse of 6 cycles at 6 kHz which is plotted in Figure 3.4. The choice of center frequency was influenced by the operational requirements of the acoustic transducers and by resolution considerations. Achievable resolution is determined in part by the medium. Propagation speed determines the wavelength for a

given frequency. With a higher frequency, better resolution can be achieved; however, higher frequencies suffer from large attenuation, resulting in poor SNR.

Signals from the 52 elements were captured individually so that processing could be done off-line. Received signals were averaged 64 times. A separate transmit pulse was used for each signal captured, so that at each position of the source and receiver array, 3328 (52×64) pulses were transmitted. Before the received signal was digitized, it was amplified by an in-line linear amplifier with a gain of 330.

Acoustic properties of soil are described by the Biot theory for sound propagation in a porous medium [88], [89]. The theory predicts the propagation of two compressional waves and a shear wave in the porous medium. A soil characterization study performed in the Bioacoustics Research Laboratory measured speed of sound and attenuation of the fast compressional wave over the range of frequencies, 1-10 kHz, for six soil types as a function of four soil moistures and two soil compactions using through transmission methods [90]. The study showed that speed of sound and attenuation for all samples varied over small ranges, 100-300 m/s and 0.1-1 dB/cm-kHz, respectively.

These results are in general agreement with the results for unconsolidated sand by Hickey and Sabatier [91]. They measured a phase velocity of 143 m/s for the slow wave and 240 m/s for the fast wave. The slow wave attenuation was measured to be 3.0 dB/cm at 1 kHz, and the fast wave attenuation was measured to be 0.87 dB/cm at 1 kHz. In their experiments, both phase velocity and attenuation of the slow wave increased with frequency.

3.3 Data Acquisition Model

We have developed a mathematical model and associated computer software to simulate the signals acquired by the experimental system. Our simulator serves as a convenient platform for the development of image reconstruction algorithms. In our model, the medium (soil) is assumed to consist of densely-spaced point scatterers, which are placed on a 3-D grid, representing the object(s) and the soil background. Each scatterer

is assigned a complex reflection coefficient

$$g(x,y,z) = |g(x,y,z)| \exp\left(\psi(x,y,z)\right). \tag{3.1}$$

The magnitude of the reflectivity is Rayleigh distributed and the phase is uniformly distributed in $[-\pi, \pi)$ for a soil scatterer [92, 93]. Both the magnitude and phase are deterministic values if there is an object at that point.

In considering the returned signal, let us first deal with the case of one scatterer. The received response from a particular reflector is a delayed version of the transmitted signal, scaled by the reflection coefficient of the scatterer and by a factor that is dependent on the range function and that is due to the attenuation of the medium and the spherical spreading of the acoustic wave [94]. The transmitted signal is $\Re e\left\{p(t)e^{j2\pi f_0 t}\right\}$ where $p(t)$ is a baseband pulse and f_0 is the carrier frequency.

Receiving element surfaces are considered to be decomposed into a collection of point receivers. Since the transmitting element is approximately omnidirectional, such a decomposition is not necessary for that element. For a particular scatterer, the signal received at a transducer is the sum of the signals received by those point receivers on the surface of the transducer [95]. This model accounts for the curvature of the wavefront incident on the transducer and eliminates the need for the knowledge of the receiving transducer beam pattern. In reference to Figure 3.2, let us denote the coordinates of a point scatterer by the vector $\underline{v} = (x, y, z)$. Similarly, we denote the center locations of the transmitter and the receiver array by $\underline{v}_t = (x_t, y_t, z_t)$ and $\underline{v}_r = (x_r, y_r, z_r)$, respectively. Notice that for the case when the transmitter and the receiver array are in the x-y plane and move along the y axis, we have $\underline{v}_t = (0, y_t, 0)$ and $\underline{v}_r = (0, y_r, 0)$. The signal received by the ith receiver, when the transmitter is at $\underline{v}_t$ and the center of the receiver array is at $\underline{v}_r$, is

$$\begin{aligned}\tilde{s}_i(t, \underline{v}_t, \underline{v}, \underline{v}_r) \;=\; & \int\int w_i(\underline{v}''; \underline{v}_r)\; |g(x,y,z)|\; \Re e\left\{p(t - \frac{R(\underline{\Lambda})}{c}) e^{j[2\pi f_0 (t - \frac{R(\underline{\Lambda})}{c}) + \theta(x,y,z)]}\right\} \\ & \cdot \frac{e^{-\beta R(\underline{\Lambda})}}{R_t(\underline{v}_t, \underline{v}) R_r(\underline{v}'', \underline{v})} dx'' dy'' \,. \end{aligned} \tag{3.2}$$

Here $\underline{v}'' = (x'', y'', z'')$ is the coordinate of the simple receiver on the surface of the ith receiver transducer. If the receiver array is in the $x - y$ plane, $z'' = 0$. This surface is represented by the window function $w_i(\underline{v}''; \underline{v}_r)$, the location of which depends on the position of the array center, $\underline{v}_r$. Vector $\underline{\Lambda} = [\underline{v}^T \ \underline{v}_t{}^T \ \underline{v}''^T \ \underline{v}_r{}^T]^T$ is defined for notational simplicity. The attenuation coefficient of the medium is β, and c is the speed of sound in soil. The range function $R(\underline{\Lambda})$ is the sum of $R_t(\underline{v}_t, \underline{v})$, which is the distance from the transmitter to a particular scatterer, and $R_r(\underline{v}'', \underline{v})$, which is the distance from the scatterer to the infinitesimal receiver surface on a particular receiver transducer. R_t and R_r are given as

$$\begin{aligned} R_t(\underline{v}_t, \underline{v}) &= \sqrt{(x - x_t)^2 + (y - y_t)^2 + (z - z_t)^2} \\ R_r(\underline{v}'', \underline{v}) &= \sqrt{(x - x'')^2 + (y - y'')^2 + (z - z'')^2} \ . \end{aligned} \tag{3.3}$$

The integrand in (3.2) is a delayed version of the transmitted signal reflected from a scatterer at $\underline{v}$. It is scaled by the magnitude of the reflectivity and phase shifted by the phase of the reflectivity. The fractional term in the integrand is the attenuation term. The numerator of this term represents the attenuation due to the medium and the denominator accounts for the attenuation due to the spherical spreading of the acoustic wave. The return wave is incident onto a point receiver at the coordinate $\underline{v}''$. The limits of the integration are determined by $w_i(\underline{v}''; \underline{v}_r)$. Hence, the integration is over the surface of the ith receiver transducer.

After quadrature demodulation, we have the complex baseband representation of the received signal as

$$\begin{aligned} \bar{s}_i(t, \underline{v}_t, \underline{v}, \underline{v}_r) &= \int\int w_i(\underline{v}''; \underline{v}_r) g(x, y, z) \frac{e^{-\beta R(\underline{\Lambda})}}{R_t(\underline{v}_t, \underline{v}) R_r(\underline{v}'', \underline{v})} \\ &\quad \cdot p(t - \frac{R(\underline{\Lambda})}{c}) \exp\left(-jk_0 R(\underline{\Lambda})\right) dx'' dy'' \end{aligned} \tag{3.4}$$

where $k_0 = 2\pi f_o / c$ is the wavenumber corresponding to the center frequency. The term due to attenuation can be eliminated approximately by using time gain compensation (TGC) on the received data [9]. The total received signal for the ith transducer of the receiver array, for a fixed array position, is the sum of responses from all scatterers in

the medium:

$$\hat{s}_i(t, \underline{v}_t, \underline{v}_r) = \int_0^\infty \int_{-\infty}^\infty \int_{-\infty}^\infty \bar{s}_i(t, \underline{v}_t, \underline{v}, \underline{v}_r)\, dx\, dy\, dz. \tag{3.5}$$

In computer implementation of this model, it is not possible to account for a continuum of scatterers or a semi-infinite medium. Therefore we assume a finite size, 3-D, discrete grid of point scatterers in order to simulate objects and the background soil.

3.4 Image Reconstruction

The data acquisition system is translated across the surface of the medium as the the system emits the tapered sinusoidal pulse and collects returns. We mainly have explored two methods of forming images from the collected data, namely delay-and-sum beamforming and a method which basically is an application of synthetic aperture radar (SAR) processing to the current data collection scenario.

The study concerning the beamforming was carried out by Frazier et al. [96]. The basic idea of the beamforming is the following: At each position of the data acquisition system, a single beam can be formed by focusing the array broadside, so that a conventional B-mode image may be formed with data from multiple positions. Alternatively, since the signals have been recorded separately, several beams can be formed for each source-receiver array position by synthesizing several elements centered at positions between the source and the receiver. To synthesize an element between the source and receiver, the 52 signals are first delayed to simulate a signal transmitted from a synthesized position and then are delayed to simulate a focused receiver at the synthesized position. Creating multiple beams at each position of the source and receiver could provide for some averaging to increase signal-to-noise ratio, although this was not done in our study. The beamforming has been applied to experimental data obtained from the experiment set described above. In the images reconstructed by the beamforming, buried objects can be detected, but the resolution is not at the desired level to identify the objects. For the full description and results of the beamforming applied to experimental data, see [96].

Given N transducers, a linear receiver array could provide far higher resolution than a rectangular array if synthetic aperture processing were used. Suppose data were collected from a linear array moved in a direction normal to its orientation. This corresponds to

a linear array with its longer dimension being along the x axis, as depicted in Figure 3.5. High resolution in the direction of travel could then be obtained by using algorithms similar to those employed in synthetic aperture radar (SAR) or synthetic aperture sonar. High resolution along the dimension of the array would be obtained by using the beamforming approach. A difference between subsurface imaging and SAR is that in the former we have attenuation of the signal due to the medium. We have developed a SAR-type reconstruction algorithm for the acoustic imaging scenario using a modification of the correlation algorithm described in Appendix D. The main steps and the necessary modifications are explained briefly in the following.

By passing the returned signal through a quadrature demodulator, the carrier can be suppressed, and the complex baseband signal can be obtained for each of the receivers in the linear array. The linear array then can be focused to a fixed depth, or can be dynamically focused to various depths by using beamforming. This results in a single waveform for each location of the data acquisition system. Let us denote the signal obtained after focusing as

$$\bar{s}(t, y_a) = \int_0^{\infty} \int_{-\infty}^{\infty} g(y,z) w_a(y - y_a) w_r(z) p(t - \frac{R_t + R_r}{c}) \exp\left(-jk_0(R_t + R_r)\right) dydz, \tag{3.6}$$

where y_a is the azimuth coordinate at which the returns are collected by the linear receiver array. The terms $w_a(y)$ and $w_r(z)$ are window functions representing the area illuminated by the transmitted acoustic beam in the azimuth and range directions, respectively. First-order Taylor series approximations of R_r and R_t,

$$R_r = \sqrt{(y - y_a)^2 + z^2} \approx z + \frac{(y - y_a)^2}{2z} \tag{3.7}$$

$$R_t = \sqrt{(y - y_a - d)^2 + z^2} \approx z + \frac{(y - y_a - d)^2}{2z}, \tag{3.8}$$

are valid if the conditions $z \gg y - y_a$ and $z \gg y - y_a - d$ hold. Here, d is the distance between the transmitter and receiver. We assume that the transmitted signal varies slowly enough that $p(t - \frac{R_t + R_r}{c}) \approx p(t - \frac{2z}{c})$. Assigning $g_1(y,z) = g(y,z)e^{-j2k_0 z}$ and

making the change of variables, $y \rightarrow \nu, z \rightarrow \xi$, and $t = \frac{2z}{c}$, we can write

$$s(y_a, z) = \int \bar{g}(y_a, \xi)\ w_r(\xi)\ p(\frac{2}{c}(z-\xi))\ d\xi \tag{3.9}$$

$$\bar{g}(y_a, \xi) = \int g_1(\nu, \xi)\ w_a(\nu - y_a)\ \exp(-jk_0\frac{(\nu - y_a)^2}{2\xi})\ \exp(-jk_0\frac{(\nu - y_a - d)^2}{2\xi})\ d\nu\ . \tag{3.10}$$

In the so-called range processing step, the received signal in (3.9) is correlated with the transmitted signal to find a matched-filter estimate for $\bar{g}_1(y_a, z)$. Then this estimate is used to solve for $g_1(y_a, z)$ by correlating the estimate of $\bar{g}_1(y_a, z)$ with the filter corresponding to the exponential terms in (3.10). This step is called *azimuth processing.* With the above formulation, range processing is the same as in the standard correlation-based SAR algorithm in [42], which is also outlined in Appendix D. But in the standard algorithm, since it has been derived for a radar scenario, there is only one signal received by the single antenna located on the radar platform. Also, for the case of a single antenna, the transmitter-to-reflector and reflector-to-receiver distances are the same in the radar case. Notice that the attenuation term in (3.2) is not incorporated in (3.6). This is because we apply time-gain compensation to the received signal to compensate approximately for the effect of attenuation.

The above SAR-type algorithm was applied to simulated data consisting of three point targets and background soil scatterers. A linear array of eight receivers, corresponding to the center of the experimental receiver array, was used. The point targets were positioned at $x = y = 0$ and at depths 0.1 m, 0.4 m, and 0.7 m. The grid for the background soil scatterers extended from $x = -0.2$ m to $x = 0.2$ m, from $y = -0.49$ m to $y = 0.49$ m, and from $z = 0.01$ m to $z = 0.9$ m. The resulting image is shown in Figure 3.6. The reconstructed image represents the $y - z$ plane at a fixed x value according to our coordinate convention in Figure 3.2. As mentioned, we used time-gain compensation to nearly eliminate the effect of attenuation. Without the compensation, only the scatterer at $z = 0.1$ m could be seen. Note that the point objects are not reconstructed at their exact locations in depth. This effect is most noticeable for the object closest to the surface. The reason for this is that our Taylor approximations for the transmitter-reflector-receiver distances are not valid for close objects. In a SAR scenario,

these approximations are generally valid because the range distance in radar imaging is typically very large. Note also that we approximated two distance functions in our case to take into account the off-center transmitter. If the standard monostatic SAR algorithm had been applied without that modification, the point target images in Figure 3.6 would have been shifted in the azimuth direction, too. The clouds around the images of point objects are due to the soil scatterers.

The SAR-type reconstruction algorithm was also applied to real data obtained from the experimental system. However, the result was not satisfactory; there was much clutter in the image, although there were bright spots at the locations of the objects. In a SAR reconstruction, resolution in the range direction increases as the bandwidth of the transmitted signal increases. Azimuth resolution depends on the distance covered by the data acquisition system during illumination of a target by the transmitted acoustic beam. Collecting more data in the azimuth dimension provides for an increase in resolution in the azimuth direction. In our experimental system, the length of the scan is limited by the size of the box, which presented a complication to successfully applying SAR-type imaging. An interesting point about the real data is that most of the information in the returned signals was in the frequencies below 1500 Hz rather than near 6 kHz, which was the center frequency of our transmitted pulse. The high received signal strength at frequencies below 1500 Hz is clearly due to the frequency-dependent attenuation of the medium. However, in our data model we incorporated the attenuation of the medium by the parameter β only for a single frequency. Compensating the return signals for the loss due to attenuation is done accordingly for a single frequency.

The system itself could be improved to produce data with better signal-to-noise ratio. Currently we use a point source and array receiver. The source and receiver were chosen because of their availability and their ability to transmit high-powered, shaped pulses and to receive small signals. With a focused source, we could transmit more energy to the region of interest, rather than spreading the energy over a wide area. A study exploiting this idea has been published recently [63]. In addition, if we could put the source and receiver closer together, we could increase the depth of penetration by reducing the total distance the sound must travel from source to target to receiver at a given depth. Our source had been designed to give the best performance between 6 kHz and 10 kHz.

Since the received signal components are at a lower frequency, a source with an optimal response at 2 kHz or even below will perform better.

3.5 Three-Dimensional $\omega - k$ Formulation of the Problem

The bistatic SAR-type reconstruction algorithm, which we have developed to reconstruct images of objects buried in soil, suffer from shifts and smears for objects very close to the surface, since the employed assumption of plane-wave propagation is not accurate in the near field. If the transmitter were capable of transmitting linear FM chirp signals, it would be possible to use the wavenumber-domain ($\omega - k$) SAR algorithm to give more accurate results for near-field sources, since the $\omega - k$ algorithm takes wavefront curvature into account [57,59]. The transmitter in the experimental system was designed to transmit shaped sinusoidal pulses and cannot transmit linear FM chirp waveforms efficiently. However, using a linear FM chirp as the transmitted waveform is an important step in performing wavenumber-domain processing accurately.

The geometry of the data acquisition scenario for acoustic imaging of buried objects is depicted in Figure 3.5. A linear array of receivers is used to collect the returns at different locations along the x axis as the array moves in the y direction. Since the linear array collects two-dimensional data in the x-y plane from the 3-D volume beneath, the collected data is suitable for processing by the 3-D version of the $\omega - k$ algorithm.

Let us assume that the transmitter and the receiver array in Figure 3.5 are concentric; that is, the offset of the transmitter along the y axis is zero. Also assume that the transmitted signal is a linear FM chirp pulse given in (2.1). These assumptions enable us to use the monostatic version of the 3-D $\omega - k$ algorithm. Our software can easily produce data according to these settings. The bistatic version of the algorithm employs certain additional approximations [60], which become less accurate for our near-field problem. The description of the 3-D monostatic $\omega - k$ algorithm formulated for acoustic imaging of buried objects follows.

The return signal acquired by the receiver element at (x, y), when the array is at location y, is

$$\bar{s}_R(t, x, y) = \int_0^{\infty} \iint_{-\infty}^{\infty} |g(x', y', z')| \tag{3.11}$$

$$\cdot \Re e \left\{ p(t - \frac{2r'_{x,y}}{c}) \exp\left(j(\omega_0(t - \frac{2r'_{x,y}}{c}) + \psi(x', y', z')) \right) \right\} dx'dy'dz' \tag{3.12}$$

where $r'_{x,y}$ is shortened notation for the range function which is defined as

$$r(x - x', y - y', z') = \sqrt{(x - x')^2 + (y - y')^2 + z'^2}, \tag{3.13}$$

when the receiver is at location (x, y) and the coordinates of a particular scatterer are (x', y', z'). The complex reflectivity function, $g(x, y, z)$, of the volume is given by

$$g(x, y, z) = |g(x, y, z)| \exp(j\psi(x, y, z)). \tag{3.14}$$

Notice that the lower limit of the integration over the z dimension is zero since the transmitter is assumed to radiate into the soil. Alternatively, we can extend this limit to $-\infty$, keeping in mind that $g(x, y, z)$ vanishes for negative values of z.

Let us define R_0 to be the distance from the origin of the coordinate system to the center (X_0, Y_0, Z_0) of the target scene. Also, let $\tau_0 = \frac{2R_0}{c}$. Notice that unlike the scenario in Chapter 2, the transmitter here always emits toward broadside, that is, in the z direction. Since the array is not steered as in the spotlight-mode SAR scenario, the mode of data collection is the same as in strip-mapping SAR. In this geometry, what we mean by *scene* is the common volume irradiated by the transmitter beam pattern as the array moves along the synthetic aperture. With an omnidirectional transmitter, the target can be illuminated independent of the size of the receiver aperture. However, because of the large attenuation of the soil, the return signal will be very small if the array is far from the target scene in the y direction.

Define the temporal frequency $\omega = \omega_0 + 2\alpha(t - \tau_0)$. The wavenumber is given by $k = \omega/c$ where c is the speed of the acoustic wave in the soil. Deramping (see Appendix

A) yields the return signal in complex baseband as

$$s_R(t,x,y) = \iiint_{-\infty}^{\infty} g(x',y',z') e^{-j2kr'_{x,y}} e^{j2kR_0} e^{j\frac{4\alpha}{c^2}(r'_{x,y}-R_0)^2}\, dx'dy'dz'. \tag{3.15}$$

Then, letting the 3-D *imaging kernel* (see also the 2-D imaging kernel (2.11)) be denoted by

$$f(x,y,z';\omega) = \exp\left(-j2kr(x,y,z')\right) \tag{3.16}$$

and omitting the second and third exponential terms, we can write the return signal as

$$s(\omega,x,y) = \iiint_{-\infty}^{\infty} g(x',y',z')\ f(x-x',y-y',z';\omega)\ dx'dy'dz'. \tag{3.17}$$

Let us write the imaging kernel in terms of its 3-D Fourier transform as

$$f(x,y,z';\omega) = \frac{1}{8\pi^3} \iiint_{-\infty}^{\infty} F(k_x,k_y,k_{z'};\omega) e^{j(k_x x + k_y y + k_{z'} z')}\, dk_x dk_y dk_{z'}. \tag{3.18}$$

Inserting this into the return equation, we obtain

$$\begin{aligned} s(\omega,x,y) \;=\; & \frac{1}{8\pi^3} \iiint_{-\infty}^{\infty} g(x',y',z') \iiint_{-\infty}^{\infty} F(k_x,k_y,k_{z'};\omega) \\ & \cdot\ e^{j(k_x(x-x')+k_y(y-y')+k_{z'}z')}\, dk_x dk_y dk_{z'} dx'dy'dz', \end{aligned} \tag{3.19}$$

which can be written as

$$\begin{aligned} s(\omega,x,y) \;=\; & \frac{1}{8\pi^3} \iiint_{-\infty}^{\infty} F(k_x,k_y,k_{z'};\omega) e^{jk_x x} e^{jk_y y} \\ & \cdot \iiint_{-\infty}^{\infty} g(x',y',z') e^{j(-k_x x' - k_y y' + k_{z'} z')}\, dx'dy'dz'\ dk_x dk_y dk_{z'}. \end{aligned} \tag{3.20}$$

The second triple integration amounts to $G(k_x, k_y, -k_{z'})$ where $G(k_x, k_y, k_{z'})$ is the 3-D Fourier transform of $g(x, y, z)$. Then we have

$$s(\omega, x, y) = \frac{1}{8\pi^3} \iiint_{-\infty}^{\infty} F(k_x, k_y, k_{z'}; \omega) G(k_x, k_y, -k_{z'}) e^{jk_x x} e^{jk_y y} \, dk_x dk_y dk_{z'}. \tag{3.21}$$

Inserting $F(k_x, k_y, k_{z'}; \omega)$ from Appendix C gives

$$s(\omega, x, y) \approx \frac{A_2}{4\pi^2} \iint_{-\infty}^{\infty} G(k_x, k_y, \sqrt{4k^2 - k_x^2 - k_y^2}) e^{jk_x x} e^{jk_y y} \, dk_x dk_y. \tag{3.22}$$

Thus,

$$S(\omega, k_x, k_y) \approx A_2 \, G(k_x, k_y, \sqrt{4k^2 - k_x^2 - k_y^2}) \tag{3.23}$$

where $S(\omega, k_x, k_y)$ is the two-dimensional Fourier transform of $s(\omega, x, y)$. Let

$$k_z = \sqrt{4k^2 - k_x^2 - k_y^2} \, . \tag{3.24}$$

Thus, taking the 2-D Fourier transform of the collected data $s(\omega, x, y)$ in the x and y dimensions, we obtain the 3-D Fourier transform of the reflectivity function within a complex constant. Specifically, the 2-D Fourier transform of $s(\omega, x, y)$ in the latter two variables gives $A_2 \, G(k_x, k_y, k_z)$.

Therefore, taking the 3-D inverse Fourier transform of (3.23), we can obtain $g(x, y, z)$. However, as indicated by the relation in (3.24), k_x, k_y, and k_z lie on an irregular grid. Therefore, data on this irregular grid must be interpolated onto a Cartesian grid before a 3-D inverse FFT can be applied. Fortunately, since this is the broadside case (squint angle is zero), the Fourier data is not subject to severe geometric distortion; hence, interpolation is easier than in the runway imaging problem.

Figure 3.1 Experimental system.

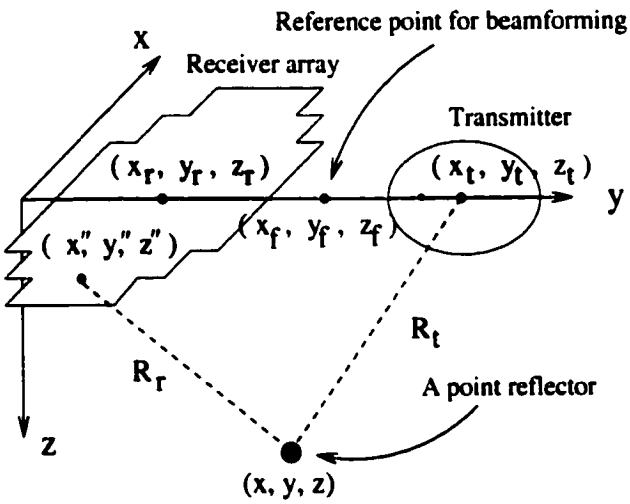

Figure 3.2 Array of transducers and associated coordinate system. Surface of the array is in the $x - y$ plane. Array motion is in y direction.

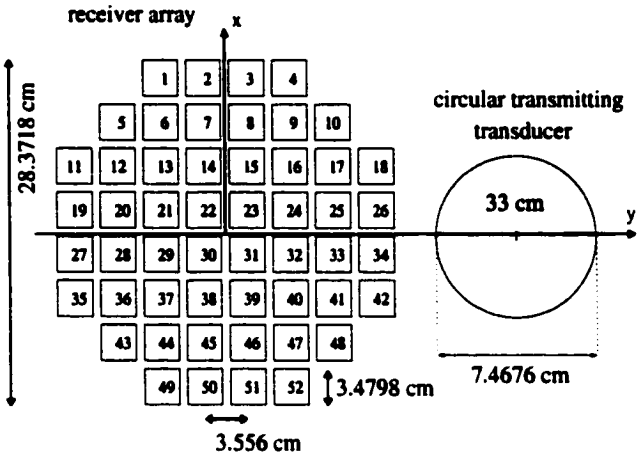

Figure 3.3 Geometry of the transmitter and receiving array; view from the top. Origin is at the center of the receiver array.

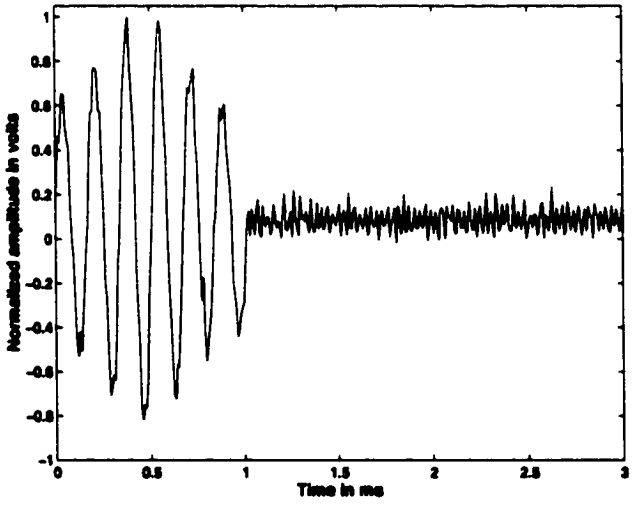

Figure 3.4 Transmitted signal.

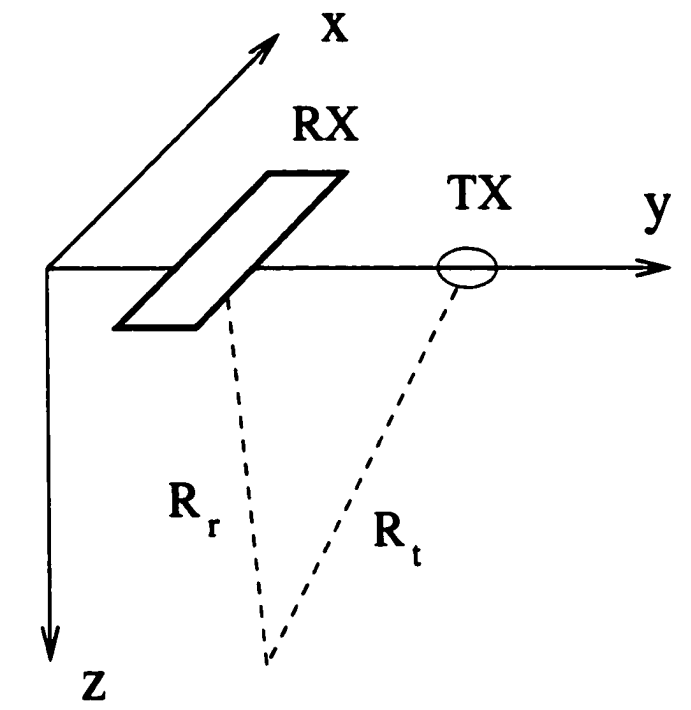

Figure 3.5 Linear array and off-center transmitter.

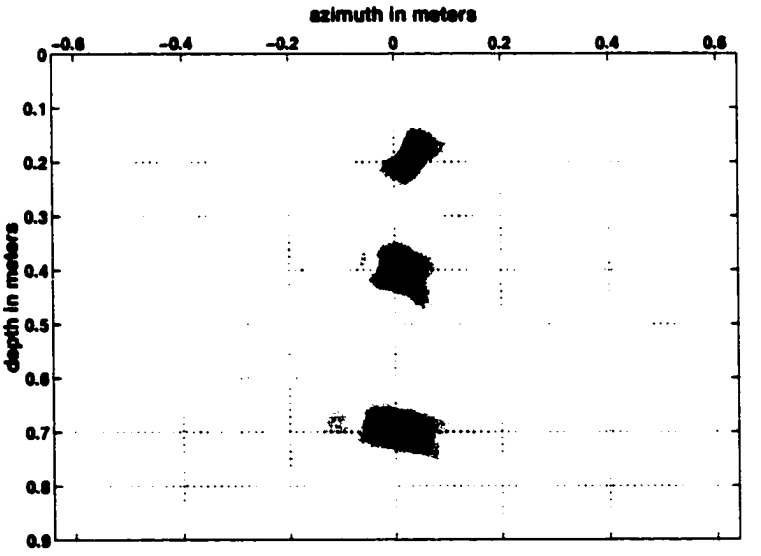

Figure 3.6 SAR-type reconstruction of three point objects from simulated data.

CHAPTER 4

LIDAR IMAGING OF UNDERWATER OBJECTS

4.1 Introduction

Detection and localization of underwater objects is an important problem, especially for military purposes. In a prototype system designed by Lockheed-Sanders for the U.S. Navy, airborne lidar is used to detect, locate, and classify underwater objects, such as mines. The transmitted laser beam can penetrate the air-water interface and illuminate scatterers in the water column. The transmitted laser signal experiences scattering and absorption within the water column illuminated by the laser beam. The returned lidar signals are received by a photomultiplier tube (PMT) and a charge-coupled device (CCD). The CCD image and the PMT data provide shape and depth information, respectively, about objects that are in the illuminated water column. Both receiver outputs can be analyzed and processed by a trained operator to classify the object and determine its depth and location.

An improvement to the above method of detection and imaging of underwater objects might be possible by collecting lidar returns from a specific 3-D volume of water at various view angles. In this case, 3-D tomographic processing might produce 3-D reconstructions with possibly better resolution or provide an estimate of the surface curvature of objects. In this study, we formulate the detection and localization problem as a 3-D tomographic reconstruction problem: We describe the relation between the airborne CCD/PMT returns and corresponding tomographic projections of an underwater object. We describe our development of software to simulate lidar returns in PMT and CCD sensors. Our simulator can model multiple scattering and absorption for various water types and system parameters. We perform reconstructions using real data from a previous study (1998 Competitive Evaluation Field Test (CEFT), Panama City, FL). We

present our reconstruction results from the simulated and real data, and comparatively discuss the reconstructions.

4.2 Data Acquisition and Tomographic Interpretation

The data collection scenario is depicted in Figure 4.1. A laser transmitter and a receiver are mounted externally on an aircraft. The laser emits short, high-energy pulses of light at a 532-nm wavelength, with a large beam width. The receiver optics is boresighted to the transmitter and uses a filter to admit only the returning laser frequency. The system continuously scans the field of view over a rectangular search swath by deflecting the laser beam. A wide area can be searched in this manner as the aircraft travels along its flight path. Revisit scans can be performed if the trained operator encounters a suspicious object in the monitored data. The receiver involves two types of sensors: a 2×2 PMT, and a 64×64 element CCD array. The returns are photons backscattered from objects, particles in the water, and the water itself. For each *shot* (that is, the process of transmission of a laser pulse and reception of the return) the CCD and PMT data are stored, together with various other orientation information, such as the location and altitude of the aircraft and the location of the beam spot on the surface of the water. The CCD array records 2-D data. If we assume that the line of sight is the z direction, the output of each element of the CCD array is the the signal at a given x and y position, integrated over time, that is, over depth, or along the z direction. A minelike object appears as a bright spot in a CCD image. If the mine is above the integration depth, it appears as a shadow. Figure 4.2 shows 22 CCD images from CEFT database. These are images of a mine at different view angles. The mine is 21 ft deep and 1 m in diameter. These 22 CCD images and corresponding PMT data and parameter values were extracted from the larger CEFT database by Peter J. Shargo.

The PMT has five channels. The first channel is called the *flash channel*, and is used to detect air-water interface. This information is then used to align signals in the other channels. Each of the remaining four channels collects backscattered energy from the corresponding quadrant of the water column. The output of the PMT is displayed as a function of time or, equivalently, depth. As the system scans the field of view, the

average return profile is formed. An object such as a mine is not transparent to light and can be highly reflective. Thus, a larger return than the average and a following shadow appears in the time history of the PMT output when a minelike opaque object is inside the laser beam. The depth of the object can be found using PMT data. Figure 4.3 shows the PMT data for the fourth quadrant for the 12th shot from CEFT database. As seen in the 12th CCD image in Figure 4.2, the target appears as a bright spot in the fourth quadrant. The point A in Figure 4.3 corresponds to the air-water interface, the bottom is indicated by point C, and the bump due to the object is marked with B. The amplitude axis is logarithmic. The PMT samples are recorded every 6 ns. The location of the bump at point B can be calculated to approximately match the depth of the object. The resolution in depth depends on the duration of the laser pulse. A 10 ns pulse corresponds to a 2.25 m spatial extent. Thus, spatial length of the laser pulse is comparable to the size of the object, resulting in useful, but fairly poor, depth resolution.

The PMT and CCD outputs can be interpreted in a tomographic framework. Tomography exploits the linear and planar projections of a physical quantity via the use of projection-slice theorems. Three-dimensional versions of the projection-slice theorem are given in [18, 40].

The PMT output can be considered as the 1-D projection function of the 3-D reflectivity of the water column. In other words, the PMT output is the 2-D projection (*conjection*, as it is called in [18]) along the x and y directions of the reflectivity, if we assume that the beam axis is in the z direction. This is depicted in Figure 4.4. Due to the linear trace version of the projection-slice theorem, the 1-D Fourier transform of the PMT data (conjection) yields a ray of the 3-D Fourier transform of the reflectivity evaluated along the line of sight. This is only an approximation though, since the spatial length of the laser pulse is usually comparable to the size of an underwater mine. However, for a larger underwater object, such as a submarine, this tomographic interpretation is accurate.

CCD output can be considered as the 2-D projection function of the 3-D reflectivity of the water column. In other words, the CCD output is the 1-D projection, along the z direction, of the reflectivity, if we assume that the beam axis is in the z direction. This is depicted in Figure 4.5. Using the planar version of the 3-D projection-slice theorem,

the 2-D Fourier transform of the CCD output is a planar slice, perpendicular to the projection direction, of the 3-D Fourier transform of the reflectivity. By combining data from CCD and PMT projections, it is possible to build up a significant volume of the 3-D Fourier transform of the reflectivity of the unknown object.

4.3 Simulation of Lidar Returns

Electromagnetic theory is governed by Maxwell's equations [97, 98]. At optical frequencies, in highly scattering media, coherence degrades sufficiently so that the addition of electromagnetic fields can be safely replaced by the addition of radiant power or intensity. The theory that describes the propagation of electromagnetic energy in highly scattering media such as ocean waters is called *radiative transport theory*,[1] [99–105]. The radiative transport equation, which is the counterpart of Maxwell's equations, can be derived using the conservation of energy principle. Via small-angle scattering approximations, the radiative transport equation can be solved by Fourier transform methods. For oceanic hydrosols, particle dimensions are large compared to the wavelength. Light scattered by such particles is confined to small angles about the ray axis.

To simulate the lidar returns incident on lidar receivers, we have specifically worked with the lidar model given in [106–108], which exploits the small-angle scattering approximation. The model takes into account multiple scattering with time dispersion. Analytical expressions for the lidar returns, using numerical integration, are given by using a statistical model for the beam spread function. These expressions have been reported to be in agreement with multiple-scattering Monte-Carlo simulations and real lidar data. The lidar equations in [108] are for a monostatic geometry of transmitter and receiver. We have derived the lidar equations for the more general case of bistatic lidar. Next, we present the bistatic lidar equations and then show examples of simulated lidar returns that are computed using these equations.

[1] In some texts, it is referred to as *radiative transfer theory*.

4.3.1 Bistatic lidar equations

Let the source radiance for a laser pulse with energy Q, located at the origin and directed along the z axis, be

$$L(0, \bar{\rho}, \bar{s}, t) = Q\ \delta(\bar{\rho})\ \delta(\bar{s})\ \delta(t)\ , \tag{4.1}$$

where the position vector is

$$\bar{r} = \hat{i}x + \hat{j}y + \hat{k}z = \bar{\rho} + \hat{k}z \tag{4.2}$$

and the direction vector is

$$\begin{aligned} \hat{s} &= \hat{i}\sin\theta\cos\phi + \hat{j}\sin\theta\sin\phi + \hat{k}\cos\theta & (4.3)\\ &\approx \bar{s} + \hat{k}\ . & (4.4) \end{aligned}$$

The approximation is due to the small-angle scattering assumption. This dictates the so-called forward scattering regime where $s = |\bar{s}| \ll 1$ and $\rho \ll z$. Notice that, temporally, the pulse is an impulse. To incorporate the pulse shape, we convolve the lidar returns, which we calculate later in this section, with the pulse shape.

The so-called target plane is parallel to the x-y plane and located at a distance z in the z direction. Radiance after propagating a distance z to the target plane is

$$L(z, \bar{\rho}, \bar{s}, t) = Q\ k(z, \bar{\rho}, \bar{s}, \tau)\ . \tag{4.5}$$

The *medium beam spread function* is denoted by $k(z, \bar{\rho}, \bar{s}, \tau)$. The multipath time is given by

$$\tau = t - z/c\ , \tag{4.6}$$

where c is the speed of light. The multipath time is the time required for a scattered photon to arrive at the target plane. The medium transfer function is the Fourier transform

of the beam spread function,

$$K(z,\bar{\kappa},\bar{q},\tau) = \int\cdots\int k(z,\bar{\rho},\bar{s},\tau)\ \exp\left(j(\bar{\kappa}\cdot\bar{\rho}+\bar{q}\cdot\bar{s})\right)\ d\bar{\rho}\ d\bar{s}. \tag{4.7}$$

Inversely,

$$k(z,\bar{\rho},\bar{s},\tau) = \frac{1}{(2\pi)^4}\int\cdots\int K(z,\bar{\kappa},\bar{q},\tau)\ \exp\left(-j(\bar{\kappa}\cdot\bar{\rho}+\bar{q}\cdot\bar{s})\right)\ d\bar{\kappa}\ d\bar{q}. \tag{4.8}$$

Here, $\bar{\kappa}$ and $\bar{q}$ are the vectors for spatial and angular frequencies corresponding to $\bar{\rho}$ and $\bar{s}$, respectively. The terms $d\bar{\rho}$, $d\bar{s}$, $d\bar{\kappa}$, and $d\bar{q}$ are the corresponding 2-D differentials. Limits of the integrals extend from $-\infty$ to ∞, consistent with the small-angle scattering approximation.

The beam spread function can serve as a Green's function in the formulation of the lidar equations, with the introduction of arbitrary position and direction offsets for the source radiance expression. Then, for a source at $\bar{\rho}'$ and radiating toward the direction $\hat{s}' = \bar{s}' + \hat{k}$, we have

$$L(0,\bar{\rho},\bar{s},\bar{\rho}',\bar{s}',t) = Q\ \delta(\bar{\rho}-\bar{\rho}')\ \delta(\bar{s}-\bar{s}')\ \delta(t)\ . \tag{4.9}$$

In the target plane at a distance z in the z direction from the source, the radiance is

$$L(z,\bar{\rho},\bar{s},\bar{\rho}',\bar{s}',t) = Q\ k(z,\bar{\rho},\bar{s},\bar{\rho}',\bar{s}',\tau) \tag{4.10}$$

Here $s' \ll 1$, that is, the arbitrary radiation direction satisfies the small angle approximation too. Thus, $|\bar{s}'| = \theta$, that is, the angle between the beam axis and the z axis. Beam axis offset is, therefore, given by $\bar{\rho}' + z\bar{s}'$. Let r_0 be the distance from the source to the beam center in the target plane. We have

$$\begin{aligned} r_0 &= \sqrt{|\bar{\rho}'+z\bar{s}'|^2+z^2} \\ &\approx z + \frac{|\bar{\rho}'+z\bar{s}'|^2}{2z}\ . \end{aligned} \tag{4.11}$$

The time required for a photon to arrive at the target plane is then

$$\begin{aligned} t &= r_0/c + \tau \\ &\approx \frac{z}{c} + \frac{|\vec{\rho}' + z\vec{s}'|^2}{2zc} + \tau \end{aligned} \tag{4.12}$$

or stated in another way

$$t - \frac{z}{c} = \tau + \frac{|\vec{\rho}' + z\vec{s}'|^2}{2zc}\ , \tag{4.13}$$

that is, the time gets extended by the geometric path. We then have

$$\begin{aligned} L(z, \bar{\rho}, \bar{s}, \vec{\rho}', \vec{s}', t) &= Q\ k(z, \bar{\rho}, \bar{s}, \vec{\rho}', \vec{s}', \tau) \\ &\approx Q\ k(z, \bar{\rho} - (\vec{\rho}' + z\vec{s}'), \bar{s} - \vec{s}', \tau + \frac{|\vec{\rho}' + z\vec{s}'|^2}{2zc}) \end{aligned} \tag{4.14}$$

where the approximation is due to the small-angle scattering assumption in the definition of $\bar{s}$. We assume that the multipath length is much larger than the geometric path length. Thus, we can drop the term due to the geometric path length extension and assume

$$t = \frac{z}{c} + \frac{|\vec{\rho}' + z\vec{s}'|^2}{2zc} + \tau \approx z/c + \tau. \tag{4.15}$$

The radiance in the target plane due to a shaped laser beam is

$$L(z, \bar{\rho}, \bar{s}, t) = Q \int\cdots\int \psi(\vec{\rho}')\ \theta(\vec{s}')\ k(z, \bar{\rho} - (\vec{\rho}' + z\vec{s}'), \bar{s} - \vec{s}', \tau)\ d\vec{\rho}'\ d\vec{s}', \tag{4.16}$$

where the beam spread function $k(z, \bar{\rho}, \bar{s}, \tau)$ is convolved with the *aperture function* $\psi(\bar{\rho})$ that specifies the spatial extent of the source and with the function $\theta(\bar{s})$ that specifies the *angular radiation pattern* of the source. Since

$$k(z, \bar{\rho} - (\vec{\rho}' + z\vec{s}'), \bar{s} - \vec{s}', \tau) = \frac{1}{(2\pi)^4} \int\cdots\int K(z, \bar{\kappa}, \bar{q}, \tau)\ e^{-j(\bar{\kappa}\cdot(\bar{\rho} - \vec{\rho}' - z\vec{s}') + \bar{q}\cdot(\bar{s} - \vec{s}'))}\ d\bar{\kappa}\ d\bar{q}, \tag{4.17}$$

we have

$$L(z, \bar{\rho}, \bar{s}, t) = \frac{Q}{(2\pi)^4} \int\cdots\int \Psi(\bar{\kappa})\ \Theta(\bar{q} + \bar{\kappa}z)\ K(z, \bar{\kappa}, \bar{q}, \tau)\ e^{-j(\bar{\kappa}\cdot\bar{\rho} + \bar{q}\cdot\bar{s})} d\bar{\kappa}\ d\bar{q}. \tag{4.18}$$

Consider a transmitter (laser source) that has position and direction offsets $\bar{\rho}_{TX}$ and $\bar{s}_{TX}$, respectively. The offset functions are

$$\psi_{TX}(\bar{\rho} - \bar{\rho}_{TX}) \quad \text{and} \quad \theta_{TX}(\bar{s} - \bar{s}_{TX}) \tag{4.19}$$

with Fourier transforms

$$\Psi_{TX}(\bar{\kappa}) e^{j\bar{\kappa}\cdot\bar{\rho}_{TX}} \quad \text{and} \quad \Theta_{TX}(\bar{q}) e^{j\bar{q}\cdot\bar{s}_{TX}} \tag{4.20}$$

Thus, in general, we have

$$L(z, \bar{\rho}, \bar{s}, t) = \frac{Q}{(2\pi)^4} \int\cdots\int \Psi_{TX}(\bar{\kappa})\, \Theta_{TX}(\bar{q} + \bar{\kappa}z)\, K(z, \bar{\kappa}, \bar{q}, \tau)\, e^{j\bar{\kappa}\cdot\bar{\rho}_{TX}}\, e^{j(\bar{q}+\bar{\kappa}z)\cdot\bar{s}_{TX}}\, e^{-j(\bar{\kappa}\cdot\bar{\rho}+\bar{q}\cdot\bar{s})}\, d\bar{\kappa}\, d\bar{q} \tag{4.21}$$

as the radiance at the target plane at a distance z from the origin due to an offset transmitter.

4.3.1.1 Bottom return

Consider the airborne lidar geometry depicted in Figure 4.6, where TX and RX denote a transmitter (laser source) and a receiver. The transmitter and the receiver are, in general, at different locations and directed at different directions. This geometry is often called *bistatic*. The geometry where the transmitter and receiver are at the same location and have the same directional orientation is called *monostatic*. To handle the bistatic case, we assign position and direction offsets $\bar{\rho}_{RX}$, $\bar{s}_{RX}$ to the aperture function, $\psi_{RX}(\bar{\rho})$, and radiation pattern, $\theta_{RX}(\bar{s})$, of the receiver. The altitude of the transmitter and receiver from the water surface is H.

We first calculate the radiance incident on the bottom of the water column, which is usually the ocean bottom in mine imaging. Let the bottom be at depth z in Figure 4.6. We incorporate the refraction at the air-water interface. Let m denote the index of refraction for water, which is, in general, a function of wavelength, temperature, pressure,

and type of water. However, it can be assumed to be a constant, approximately equal to $\frac{4}{3}$, since it does not vary much over a large range of parameters relevant to hydrological optics [104, p.83]. The index of refraction for air is assumed to be unity. Denoting the speed of light in air by c, we have c/m as the speed of light in water. We assume that the atmosphere is dispersionless with transmission coefficient T_{atm}. Transmission coefficient for the air-water interface is given by $T_{aw} = (\frac{1-m}{1+m})^2$. This employs the fact that water does not display any significant magnetic properties, and hence the permeability of water is close to that of air and free space. Applying Snell's law at the air-water interface, we have $\sin\theta_1 = m \sin\theta_2$. Due to the small-angle assumption, this becomes $\theta_1 = m\,\theta_2$. Then, the position offset of the transmitter associated with the downwelling path is

$$z\tan\theta_2 + H\tan\theta_1 \approx z\theta_2 + H\theta_1 = (z + Hm)\theta_2 \; . \tag{4.22}$$

Notice that in (4.16), $\bar{\rho}'$ and $\bar{s}'$ denote the offset position and direction in water. Here, $\bar{s}'$ stands for the direction offset of the airborne transmitter. Thus, in water this angle is $\bar{s}'/m$ due to the refraction. Inserting these expressions in the equation, we have the transmitted radiance incident on the bottom

$$\begin{aligned} L_{TX}(H + z, \bar{\rho}, \bar{s}, t) = \frac{QT_{atm}T_{aw}}{(2\pi)^4} \int\cdots\int \Psi_{TX}(\bar{\kappa})\; \Theta_{TX}(\bar{q}/m + \bar{\kappa}(H + z/m)) \\ \cdot\, K(z, \bar{\kappa}, \bar{q}, \tau)\; e^{j\bar{\kappa}\cdot\bar{\rho}_{TX}}\; e^{j(\bar{q}/m + \bar{\kappa}(H+z/m))\cdot\bar{s}_{TX}}\; e^{-j(\bar{\kappa}\cdot\bar{\rho} + \bar{q}\cdot\bar{s})}\; d\bar{\kappa}\; d\bar{q} \; , \end{aligned} \tag{4.23}$$

where $t = H/c + zm/c + \tau$. The reflected radiance from the bottom is given by

$$\begin{aligned} L_{back}(H + z, \bar{\rho}, \bar{s}, t) &= \frac{R}{\pi} \iint L_{TX}(H + z, \bar{\rho}, \bar{s}, t) d\bar{s} \\ &= \frac{Q\; T_{atm}\; T_{aw}\; R}{\pi(2\pi)^2} \iint \Psi_{TX}(\bar{\kappa})\; \Theta_{TX}(\bar{\kappa}(H + z/m)) \\ &\quad \cdot\, K(z, \bar{\kappa}, \bar{0}, \tau)\; e^{j\bar{\kappa}\cdot(\bar{\rho}_{TX} + (H+z/m)\bar{s}_{TX})}\; e^{-j\bar{\kappa}\cdot\bar{\rho}}\; d\bar{\kappa}\; d\bar{q} \; , \end{aligned} \tag{4.24}$$

where R is the bottom reflectance. Notice that the integral over $\bar{s}$ is the irradiance, which is the sum of the radiance from all directions, associated with a particular point

on the bottom. To find the radiance presented to the receiver, we assume that each point on the bottom is a diffuse source. The radiance incident on the receiver is then a convolution over $\bar{\rho}$ and t between the reflected irradiance L_{back} and the radiance due to a diffuse source. For a diffuse source, the radiance in the target plane at a distance z in the direction $\hat{s} \approx \hat{k} + \bar{s}$ is given by

$$L_{diff}(z, \bar{\rho}, \bar{s}, t) = \frac{1}{(2\pi)^2} \iint K(z, \bar{\kappa}, -z\bar{\kappa}, \tau)\, e^{-j\bar{\kappa}\cdot(\bar{\rho} - z\bar{s})}\, d\bar{\kappa}. \tag{4.25}$$

Here, we need to take into account the direction of propagation associated with the principle of optical reciprocity and the coordinate convention. In the bistatic case, the propagation direction determines the sign of the phase terms. In the expression for L_{TX}, $\bar{s}$ represents the direction $\hat{s} \approx \hat{k} + \bar{s}$, with $\hat{k}$ being downward. Thus, in the expression for L_{diff}, we need to use $-\hat{s}$. This can be justified by the optical reciprocity principle [104, 106]. Hence, for a diffuse source at the bottom radiating upwards (upwelling radiance), we have at the receiver

$$L_{diff}(H + z, \bar{\rho}, \bar{s}, t) = \frac{1}{(2\pi)^2} \iint K(z, \bar{\kappa}, -z\bar{\kappa}, \tau)\, e^{-j\bar{\kappa}\cdot(\bar{\rho} + (H + z/m)\bar{s})}\, d\bar{\kappa}. \tag{4.26}$$

Then, the radiance presented to the receiver at an altitude H from the air-water interface is

$$L_{RX}(\bar{\rho}, \bar{s}, t) = \frac{T_{atm}\, T_{aw}}{m^2} L_{back}(H + z, \bar{\rho}, \bar{s}, t) \;*_{\bar{\rho}}\; *_t \; L_{diff}(H + z, \bar{\rho}, \bar{s}, t), \tag{4.27}$$

where the term $1/m^2$ is due to the Snell cone, that is, the solid angle in the water is $1/m^2$ times the solid angle in air. We take into account this effect only in the return path because the return from the bottom is from a diffuse source. On the other hand, the downwelling radiance is from a narrow laser beam which certainly is in the Snell cone. We calculate (4.27) as

$$L_{RX}(\bar{\rho}, \bar{s}, t) = \frac{Q\, T_{atm}^2\, T_{aw}^2\, R}{m^2\, \pi} \int \frac{1}{(2\pi)^2} \iint \Psi_{TX}(\bar{\kappa})\, \Theta_{TX}(\bar{\kappa}(H + z/m))\, K(z, \bar{\kappa}, \bar{0}, \tau') \cdot e^{-j\bar{\kappa}\cdot\bar{\rho}}\, e^{j\bar{\kappa}\cdot(\bar{\rho}_{TX} + (H + z/m)\bar{s}_{TX})}\, K(z, \bar{\kappa}, -z\bar{\kappa}, \tau - \tau')\, e^{-j(H + z/m)\bar{\kappa}\cdot\bar{s}}\, d\bar{\kappa}\, d\tau'. \tag{4.28}$$

After some manipulation, we have

$$L_{RX}(\bar{\rho},\bar{s},t) = \frac{Q\,T_{atm}^2\,T_{aw}^2\,R}{m^2\,\pi(2\pi)^2}\iint\ \Psi_{TX}(\bar{\kappa})\,\Theta_{TX}(\bar{\kappa}(H+z/m))$$
$$\cdot\ e^{-j\bar{\kappa}\cdot\bar{\rho}}\ e^{j\bar{\kappa}\cdot(\bar{\rho}_{TX}+(H+z/m)\bar{s}_{TX})}\ e^{-j(H+z/m)\bar{\kappa}\cdot\bar{s}}\ (K(z,\bar{\kappa},\bar{0},\tau)\ *_t K(z,\bar{\kappa},-z\bar{\kappa},\tau))\ d\bar{\kappa} \tag{4.29}$$

with $t = 2H/c + 2zm/c + \tau$. To complete the return, we include receiver field of view (FOV) Ω_{RX}, and receiver aperture area A_{RX},

$$P_{bottom}(t) = A_{RX}\Omega_{RX}\int\cdots\int L_{RX}(\bar{\rho},\bar{s},t)\ \psi'_{RX}(\bar{\rho})\ \theta'_{RX}(\bar{s})\ d\bar{\rho}\ d\bar{s}, \tag{4.30}$$

where

$$\begin{aligned}\psi'_{RX}(\bar{\rho}) &= \psi_{RX}(\bar{\rho}-\bar{\rho}_{RX})\\ \theta'_{RX}(\bar{s}) &= \theta_{RX}(\bar{s}-\bar{s}_{RX})\end{aligned} \tag{4.31}$$

are the offset functions specifying the spatial extent and angular radiation pattern of the receiver. We have

$$\begin{aligned}P_{bottom}(t) &= \frac{C_{bottom}}{(2\pi)^2}\iint\ \Psi_{TX}(\bar{\kappa})\,\Theta_{TX}(\bar{\kappa}(H+z/m))\\ &\quad\cdot\ e^{j\bar{\kappa}\cdot(\bar{\rho}_{TX}+(H+z/m)\bar{s}_{TX})}\ (K(z,\bar{\kappa},\bar{0},\tau)\ *_t K(z,\bar{\kappa},-z\bar{\kappa},\tau))\\ &\quad\cdot\left(\int\cdots\int\ \psi'_{RX}(\bar{\rho})\ \theta'_{RX}(\bar{s})\ e^{-j\bar{\kappa}\cdot(\bar{\rho}+(H+z/m)\bar{s})}\ d\bar{\rho}\ d\bar{s}\right)d\bar{\kappa},\end{aligned} \tag{4.32}$$

where

$$C_{bottom} = \frac{Q\ A_{RX}\ \Omega_{RX}\ T_{atm}^2\ T_{aw}^2\ R}{m^2\ \pi}\ . \tag{4.33}$$

The last term in parentheses in (4.32) is a Fourier transform integral, which is equal to

$$\Psi'_{RX}(-\bar{\kappa})\Theta'_{RX}(-\bar{\kappa}(H+z/m)). \tag{4.34}$$

From (4.31),

$$\begin{aligned} \Psi'_{RX}(\bar{\kappa}) &= \Psi_{RX}(\bar{\kappa})e^{j\bar{\kappa}\cdot\bar{\rho}_{RX}} \\ \Theta'_{RX}(\bar{q}) &= \Theta_{RX}(\bar{q})e^{j\bar{q}\cdot\bar{s}_{RX}} \ . \end{aligned} \tag{4.35}$$

Since $\psi'_{RX}(\bar{\rho})$ and $\theta'_{RX}(\bar{s})$ are real,

$$\begin{aligned} \Psi'_{RX}(-\bar{\kappa}) &= (\Psi'_{RX}(\bar{\kappa}))^* \\ \Theta'_{RX}(-\bar{q}) &= (\Theta'_{RX}(\bar{q}))^* \ . \end{aligned} \tag{4.36}$$

Thus, we have

$$\begin{aligned} P_{bottom}(t) = \frac{C_{bottom}}{(2\pi)^2} \iint & \Psi_{TX}(\bar{\kappa})\, \Theta_{TX}(\bar{\kappa}(H+z/m))\, \Psi^*_{RX}(\bar{\kappa})\, \Theta^*_{RX}(\bar{\kappa}(H+z/m)) \\ & \cdot e^{j\bar{\kappa}\cdot((\bar{\rho}_{TX}-\bar{\rho}_{RX})+(H+z/m)(\bar{s}_{TX}-\bar{s}_{RX}))} \\ & \cdot (K(z,\bar{\kappa},\bar{0},\tau) *_t K(z,\bar{\kappa},-z\bar{\kappa},\tau))\, d\bar{\kappa} \ , \end{aligned} \tag{4.37}$$

with $t = 2H/c + 2zm/c + \tau$. Notice that if $\psi_{RX}(\bar{\rho})$ and $\theta_{RX}(\bar{s})$ are even, the conjugations above can be dropped. Notice also that for collinear and boresighted case, $\bar{\rho}_{TX} = \bar{\rho}_{RX}$ and $\bar{s}_{TX} = \bar{s}_{RX}$. If we express the bottom return in terms of lidar range ζ, we have

$$\begin{aligned} P_{bottom}(\zeta) = \frac{C_{bottom}}{(2\pi)^2} \iint & \Psi_{TX}(\bar{\kappa})\, \Theta_{TX}(\bar{\kappa}(H+D/m))\, \Psi^*_{RX}(\bar{\kappa})\, \Theta^*_{RX}(\bar{\kappa}(H+D/m)) \\ & \cdot e^{j\bar{\kappa}\cdot((\bar{\rho}_{TX}-\bar{\rho}_{RX})+(H+D/m)(\bar{s}_{TX}-\bar{s}_{RX}))} \\ & \cdot (K(D,\bar{\kappa},\bar{0},\tau) *_t K(D,\bar{\kappa},-D\bar{\kappa},\tau))\, d\bar{\kappa} \ , \end{aligned} \tag{4.38}$$

where $\zeta = D + \frac{c\tau}{2m}$ with D being the bottom depth. This is valid for $\zeta \geq D$.

4.3.1.2 Water return

The lidar return from the water medium itself is calculated similarly as the bottom return calculation. Consider the water column as a stack of infinitesimally small layers of water. Then, the backscattered radiance from each interface can be obtained using the bottom return calculation. In this case, the reflectance coefficient R/π is replaced with

$\beta(\pi)dz$, and an integration is performed over the lidar range as we keep $t = \tau + 2H/c + 2zm/c$ constant. This accounts for the photons received at a certain time from different layers of water. The term $\beta(\pi)$ is the volume scattering coefficient evaluated at the angle π corresponding to backward direction. This method of calculation assumes that the backscattered radiation is uniform over a conic section of the backward hemisphere, corresponding to the small-angle cone. We have,

$$\begin{aligned} P_{water}(t) &= \frac{C_{water}}{(2\pi)^2} \int_0^{\frac{c}{2m}(t-2H/c)} \iint \Psi_{TX}(\bar{\kappa})\, \Theta_{TX}(\bar{\kappa}(H+z/m)) \\ &\quad \cdot \Psi^*_{RX}(\bar{\kappa})\, \Theta^*_{RX}(\bar{\kappa}(H+z/m))\, e^{j\bar{\kappa}\cdot((\bar{\rho}_{TX}-\bar{\rho}_{RX})+(H+z/m)(\bar{s}_{TX}-\bar{s}_{RX}))} \\ &\quad \cdot (K(z,\bar{\kappa},\bar{0},\tau) \ *_t \ K(z,\bar{\kappa},-z\bar{\kappa},\tau))\, d\bar{\kappa}\, dz, \end{aligned} \tag{4.39}$$

where

$$C_{water} = \frac{Q\, A_{RX}\, \Omega_{RX}\, T^2_{atm}\, T^2_{aw}\, \beta(\pi)}{m^2}\ . \tag{4.40}$$

Assume $\tau \ll 2zm/c$. With $dz = -\frac{c/m}{2} d\tau$, we have the background water return in terms of the lidar range,

$$\begin{aligned} P_{water}(\zeta) &= \frac{C_{water}}{(2\pi)^2} \iint \Psi_{TX}(\bar{\kappa})\, \Theta_{TX}(\bar{\kappa}(H+\zeta/m))\, \Psi^*_{RX}(\bar{\kappa})\, \Theta^*_{RX}(\bar{\kappa}(H+\zeta/m)) \\ &\quad \cdot e^{j\bar{\kappa}\cdot((\bar{\rho}_{TX}-\bar{\rho}_{RX})+(H+\zeta/m)(\bar{s}_{TX}-\bar{s}_{RX}))} \\ &\quad \cdot \frac{c}{2m} \int_{L_1}^{L_2} (K(D,\bar{\kappa},\bar{0},\tau) \ *_t \ K(D,\bar{\kappa},-D\bar{\kappa},\tau))\, d\tau\, d\bar{\kappa}\ , \end{aligned} \tag{4.41}$$

where $L_1 = 0$, $L_2 = 2\zeta m/c$ for infinite column of water. For finite water column with bottom at depth D, the limits of the integral are $L_1 = 2(\zeta - D)m/c$, $L_2 = 2\zeta m/c$, and the expression is valid for $\zeta \geq D$. This is the contribution of photons after the leading edge of the lidar pulse has transited the bottom.

4.3.1.3 Target return

The calculation of the target return and the associated shadow return is similar to the calculation of the bottom and water return, respectively. The radiance backscattered

from a target at depth z, location $\bar{\rho}_{trgt}$ is

$$L_{back} = A_{trgt}\frac{R_{trgt}}{\pi}\delta(\bar{\rho}-\bar{\rho}_{trgt})\iint L_{TX}(H+z,\bar{\rho},\bar{s},t)\,d\bar{s}\ , \tag{4.42}$$

where A_{trgt} is the area of the flat diffuse reflecting surface of the target, R_{trgt} is the reflectance of the target, and L_{TX} is as given in (4.23). Inserting (4.23) into the above equation yields

$$\begin{aligned} L_{back}(H+z,\bar{\rho},\bar{s},t) &= A_{trgt}\frac{R_{trgt}}{\pi}\frac{Q\,T_{atm}\,T_{aw}}{(2\pi)^2}\Big(\int\cdots\int \Psi_{TX}(\bar{\kappa})\Theta_{TX}(\bar{\kappa}(H+z/m)) \\ &\quad \cdot K(z,\bar{\kappa},\bar{0},\tau)\,e^{-j\bar{\kappa}\cdot\bar{\rho}}\,e^{j\bar{\kappa}\cdot(\bar{\rho}_{TX}+(H+z/m)\bar{s}_{TX})}d\bar{\kappa}\Big)\,\delta(\bar{\rho}-\bar{\rho}_{trgt})\ . \end{aligned} \tag{4.43}$$

For a diffuse source on the target surface radiating upwards, radiance is given by (4.26) The radiance presented to the receiver is given by (4.27). Since for two arbitrary functions $f(x)$ and $g(x)$

$$f(x)\delta(x-x_0)*g(x) = f(x_0)g(x-x_0)\ , \tag{4.44}$$

we have

$$\begin{aligned} L_{RX}(\bar{\rho},\bar{s},t) &= \frac{Q\,A_{trgt}\,T_{atm}^2\,T_{aw}^2 R_{trgt}}{m^2\,\pi}\int\cdots\int \Psi_{TX}(\bar{\kappa}_1)\Theta_{TX}(\bar{\kappa}_1(H+z/m)) \\ &\quad \cdot e^{-j\bar{\kappa}_1\cdot\bar{\rho}_{trgt}}\,e^{j\bar{\kappa}_1\cdot(\bar{\rho}_{TX}+(H+z/m)\bar{s}_{TX})}\,e^{-j\bar{\kappa}_2\cdot(\bar{\rho}-\bar{\rho}_{trgt})}\,e^{-j(H+z/m)\bar{\kappa}_2\cdot\bar{s}} \\ &\quad \cdot (K(z,\bar{\kappa}_1,\bar{0},\tau)\ *_t\ K(z,\bar{\kappa}_2,-z\bar{\kappa}_2,\tau))\,\frac{d\bar{\kappa}_1}{(2\pi)^2}\,\frac{d\bar{\kappa}_2}{(2\pi)^2}\ , \end{aligned} \tag{4.45}$$

where $t = 2H/c + 2zm/c + \tau$. Incorporating the receiver FOV and aperture area, and the spatial and angular receiver radiation patterns,

$$P_{target}(t,\bar{\rho}_{trgt}) = A_{RX}\Omega_{RX}\int\cdots\int L_{RX}(\bar{\rho},\bar{s},t)\,\psi_{RX}(\bar{\rho}-\bar{\rho}_{RX})\,\theta_{RX}(\bar{s}-\bar{s}_{RX})\,d\bar{\rho}\,d\bar{s}. \tag{4.46}$$

Inserting the expressions

$$P_{target}(t,\bar{\rho}_{trgt}) = C_{target}\int\cdots\int \Psi_{TX}(\bar{\kappa}_1)\,\Theta_{TX}(\bar{\kappa}_1(H+z/m))$$

$$\cdot \left(K(z,\bar{\kappa}_1,\bar{0},\tau) \;*_t\; K(z,\bar{\kappa}_2,-z\bar{\kappa}_2,\tau)\right)\; e^{-j\bar{\kappa}_1\cdot\bar{\rho}_{trgt}}\; e^{j\bar{\kappa}_1\cdot(\bar{\rho}_{TX}+(H+z/m)\bar{s}_{TX})}$$
$$\cdot \int \psi_{RX}(\bar{\rho}-\bar{\rho}_{RX})\, e^{-j\bar{\kappa}_2\cdot\bar{\rho}} d\bar{\rho} \int \theta_{RX}(\bar{s}-\bar{s}_{RX})\, e^{-j(H+z/m)\bar{\kappa}_2\cdot\bar{s}}\, d\bar{s}\; \frac{d\bar{\kappa}_1}{(2\pi)^2}\; \frac{d\bar{\kappa}_2}{(2\pi)^2}\;, \tag{4.47}$$

where

$$C_{target} = \frac{Q\; A_{RX}\; \Omega_{RX}\; A_{trgt}\; T_{atm}^2\; T_{aw}^2\; R_{trgt}}{m^2\;\pi}\;. \tag{4.48}$$

We have

$$P_{target}(t,\bar{\rho}_{trgt}) =$$
$$C_{target} \int\cdots\int \Psi_{TX}(\bar{\kappa}_1)\; \Theta_{TX}(\bar{\kappa}_1(H+z/m))\; \Psi^*_{RX}(\bar{\kappa}_2)\; \Theta^*_{RX}(\bar{\kappa}_2(H+z/m))$$
$$\cdot\; e^{-j\bar{\rho}_{trgt}\cdot(\bar{\kappa}_1-\bar{\kappa}_2)}\; e^{j\bar{\kappa}_1\cdot(\bar{\rho}_{TX}+(H+z/m)\bar{s}_{TX})}\; e^{-j\bar{\kappa}_2\cdot(\bar{\rho}_{RX}+(H+z/m)\bar{s}_{RX})}$$
$$\cdot\; \left(K(z,\bar{\kappa}_1,\bar{0},\tau) \;*_t\; K(z,\bar{\kappa}_2,-z\bar{\kappa}_2,\tau)\right)\; \frac{d\bar{\kappa}_1}{(2\pi)^2}\; \frac{d\bar{\kappa}_2}{(2\pi)^2}\;. \tag{4.49}$$

In terms of lidar range,

$$P_{target}(\zeta,\bar{\rho}_{trgt}) =$$
$$C_{target} \int\cdots\int \Psi_{TX}(\bar{\kappa}_1)\; \Theta_{TX}(\bar{\kappa}_1(H+D/m))\; \Psi^*_{RX}(\bar{\kappa}_2)\; \Theta^*_{RX}(\bar{\kappa}_2(H+D/m))$$
$$\cdot\; e^{-j\bar{\rho}_{trgt}\cdot(\bar{\kappa}_1-\bar{\kappa}_2)}\; e^{j\bar{\kappa}_1\cdot(\bar{\rho}_{TX}+(H+D/m)\bar{s}_{TX})}\; e^{-j\bar{\kappa}_2\cdot(\bar{\rho}_{RX}+(H+D/m)\bar{s}_{RX})}$$
$$\cdot\; \left(K(D,\bar{\kappa}_1,\bar{0},\tau) \;*_t\; K(D,\bar{\kappa}_2,-D\bar{\kappa}_2,\tau)\right)\; \frac{d\bar{\kappa}_1}{(2\pi)^2}\; \frac{d\bar{\kappa}_2}{(2\pi)^2}\;, \tag{4.50}$$

where $\zeta = D + \frac{c\tau}{2m}$ and D is the target depth. The shadow return can now be written as

$$P_{shadow}(\zeta,\bar{\rho}_{trgt}) =$$
$$C_{shadow} \int\cdots\int \Psi_{TX}(\bar{\kappa}_1)\; \Theta_{TX}(\bar{\kappa}_1(H+\zeta/m))\; \Psi^*_{RX}(\bar{\kappa}_2)\; \Theta^*_{RX}(\bar{\kappa}_2(H+\zeta/m))$$
$$\cdot\; e^{-j\bar{\rho}_{trgt}\cdot(\bar{\kappa}_1-\bar{\kappa}_2)}\; e^{j\bar{\kappa}_1\cdot(\bar{\rho}_{TX}+(H+\zeta/m)\bar{s}_{TX})}\; e^{-j\bar{\kappa}_2\cdot(\bar{\rho}_{RX}+(H+\zeta/m)\bar{s}_{RX})}$$
$$\cdot\frac{c}{2m} \int_0^{2(\zeta-D)m/c} \left(K(\zeta,\bar{\kappa}_1,\bar{0},\tau) \;*_t\; K(\zeta,\bar{\kappa}_2,-\zeta\bar{\kappa}_2,\tau)\right) d\tau\; \frac{d\bar{\kappa}_1}{(2\pi)^2}\; \frac{d\bar{\kappa}_2}{(2\pi)^2}. \tag{4.51}$$

where

$$C_{shadow} = \frac{Q\ A_{trgt}\ A_{RX}\ \Omega_{RX}\ T_{atm}^2\ T_{aw}^2\ \beta(\pi)}{m^2} \tag{4.52}$$

For an arbitrary target with spatial extent $\psi_{trgt}(\bar{\rho})$,

$$P_{trgt}(\zeta, \bar{\rho}) = \iint P_{target}(\zeta, \bar{\rho}_{trgt})\ \psi_{trgt}(\bar{\rho} - \bar{\rho}_{trgt})\ d\bar{\rho}_{trgt}. \tag{4.53}$$

The total return due to the target is the subtraction of the shadow return from the target return. This is a perturbation to the background return from the water column.

4.3.1.4 Evaluation of the integrals

To compute the bistatic lidar returns presented above, we insert the medium transfer function in the integrals and perform the integration over the spatial frequency. The analytical model for the beam spread function is given as [107, 108],

$$\begin{aligned} k(z, \bar{\rho}, \bar{s}, \tau) &= \delta(\bar{\rho})\delta(\bar{s})\delta(\tau)e^{-(a+b)z} && (4.54) \\ &\quad +(1 - e^{-bz})e^{-a(z+c\tau/m)}\ g(z, \tau)\ h(z, \bar{\rho}, \bar{s}, \tau), && (4.55) \end{aligned}$$

where the first term is for unscattered photons, that is, $\tau = 0$. The second term is for photons that experience scattering, $\tau > 0$. The term $(1 - \exp(-bz))$ is the probability that a photon will be scattered. Here a and b are the absorption and scattering coefficients of water, respectively. The distribution of the variable τ dependent on depth is given by

$$g(z, \tau) = \frac{\mu}{\sigma^2\ \Gamma(\mu^2/\sigma^2)} \left(\frac{\mu\tau}{\sigma^2}\right)^{\mu^2/\sigma^2 - 1} \exp\left(-\frac{\mu\tau}{\sigma^2}\right) \tag{4.56}$$

which is the gamma distribution [109]. This is assured by the Poisson nature of the photon scattering. As a photon goes through multiple scattering, the time interval between each scattering can be modeled as an exponential random variable since the arrival time of a photon to a scatterer is a Poisson random variable, and from the photon's point of view, the arrival of a scatterer is Poisson. The multipath time τ is the sum of the time intervals between each scattering. Since the sum of exponential random variables is a gamma random variable, the distribution of τ is gamma. An alternative explanation is

the following [107]. The central limit theorem assures a Gaussian distribution for a large number of scattering events. The gamma density is equivalent to Gaussian density when the variable is positive definite, which is the case for τ.

Notice that the mean μ and the variance σ^2 of the distribution are dependent on the depth z. These are evaluated by using a statistical model developed in [110] and given in [107, 108]. From (4.55), we have the beam transfer function

$$K(z,\bar{\kappa},\bar{q},\tau) = \delta(\tau)e^{-(a+b)z} + (1-e^{-bz})e^{-a(z+c\tau/m)}g(z,\tau)H(z,\bar{\kappa},\bar{q},\tau)\ . \tag{4.57}$$

By using the time-independent solution for the beam transfer function with assuming small-angle scattering and that all the photons in the beam scatter, $H(z,\bar{\kappa},\bar{q},\tau)$ is calculated as [107, 108],

$$H(z,\bar{\kappa},\bar{q},\tau) = \exp\left(-\frac{\tau c}{mz}\left(q^2 + z\bar{q}\cdot\bar{\kappa} + \frac{1}{3}\kappa^2 z^2\right)\right), \tag{4.58}$$

where $\kappa = |\bar{\kappa}|$ and $q = |\bar{q}|$. Notice that

$$H(z,\bar{\kappa},\bar{0},\tau) = H(z,\bar{\kappa},-z\bar{\kappa},\tau)\ . \tag{4.59}$$

Then, for the temporal convolution expression, we have

$$\begin{aligned} K(z,\bar{\kappa}_1,\bar{0},\tau)\ *_t\ K(z,\bar{\kappa}_2,-z\bar{\kappa}_2,\tau) &= e^{-2az}\Big[\delta(\tau)\ e^{-2bz} \\ &+e^{-bz}\ (1-e^{-bz})\ e^{-ac\tau/m}\ g(z,\tau)\ (H(z,\bar{\kappa}_1,\bar{0},\tau) + H(z,\bar{\kappa}_2,-z\bar{\kappa}_2,\tau)) \\ &+(1-e^{-bz})^2\ e^{-ac\tau/m}\ (g(z,\tau)H(z,\bar{\kappa}_1,\bar{0},\tau)\ *_t\ g(z,\tau)H(z,\bar{\kappa}_2,-z\bar{\kappa}_2,\tau))\Big]. \end{aligned} \tag{4.60}$$

We assume that the angular transmit and receive patterns are Gaussian, that is,

$$\theta_i(\bar{s}) = \frac{1}{\pi\theta_{i,x}\theta_{i,y}}\exp\left(-s_x^2/\theta_{i,x} - s_y^2/\theta_{i,y}^2\right), \tag{4.61}$$

where i is either TX or RX, denoting transmitter or receiver. The subscripts x and y denote the x and y components of a vector. A Gaussian pattern is in agreement with

the fact that a laser beam is spatially Gaussian [111, 112]. Correspondingly,

$$\Theta_i(\bar{q}) = \exp\left(-q_x^2/\theta_{i,x}^2 - q_y^2/\theta_{i,y}^2\right). \tag{4.62}$$

Then the transmitter and receiver FOV is given as

$$\Omega_i = \pi\theta_{i,x}\theta_{i,y}. \tag{4.63}$$

Also, we assume

$$\psi_{TX}(\bar{\rho}) = \delta(\bar{\rho}). \tag{4.64}$$

The radiance field changes slowly across the receiver aperture. We, therefore, assume

$$\psi_{RX}(\bar{\rho}) = \delta(\bar{\rho}). \tag{4.65}$$

For the Fourier transform of the aperture functions, we have

$$\Psi_i(\bar{\kappa}) = 1, \tag{4.66}$$

where, again, i denotes either transmitter or receiver. In the actual system, this is true for the PMT. The CCD has a large aperture for this to be true. However, each pixel element of the CCD can be treated as a separate receiver with a narrow receiver FOV. We will tell more about the modeling of the CCD return later in this chapter.

Inserting the above equations in the lidar return expression (4.41), we have

$$\begin{aligned} P_{water}(\zeta) = \\ C_{water} \int_{L_1}^{L_2} \frac{c}{2m} e^{-2a\zeta} \Bigg[& \delta(\tau)\, e^{-2b\zeta} \underbrace{\iint e^{-X_1}\, e^{j\bar{\kappa}\cdot\bar{X}_2}\, \frac{d\bar{\kappa}}{(2\pi)^2}}_{I_1(\zeta)} \\ & + 2e^{-b\zeta}\left(1 - e^{-b\zeta}\right) e^{-ac\tau/m}\, g(\zeta,\tau) \underbrace{\iint e^{-X_1}\, e^{j\bar{\kappa}\cdot\bar{X}_2}\, H(\zeta,\bar{\kappa},\bar{0},\tau)\, \frac{d\bar{\kappa}}{(2\pi)^2}}_{I_2(\zeta)} \\ & + \left(1 - e^{-b\zeta}\right)^2 e^{-ac\tau/m} \end{aligned}$$

$$\cdot \underbrace{\iint e^{-X_1}\, e^{j\bar{\kappa}\cdot\bar{X}_2}\, (g(\zeta,\tau)H(\zeta,\bar{\kappa},\bar{0},\tau)\ *_t\ g(\zeta,\tau)H(\zeta,\bar{\kappa},-\zeta\bar{\kappa},\tau))\ \frac{d\bar{\kappa}}{(2\pi)^2}}_{I_3(\zeta)} \Bigg] d\tau, \tag{4.67}$$

where $L_1 = 0$, $L_2 = 2\zeta m/c$ for infinite column of water. For finite water column with bottom at depth D, $L_1 = 2(\zeta - D)m/c$, and $L_2 = 2\zeta m/c$. In writing the above equation we used (4.59). The shorthand notation X_1 is given as

$$X_1 = \frac{1}{4}\,(H + \zeta/m)^2\ \left(\kappa_x^2(\theta_{RX,x}^2 + \theta_{TX,x}^2) + \kappa_y^2(\theta_{RX,y}^2 + \theta_{TX,y}^2)\right) \tag{4.68}$$

where the subscripts x and y stand for the x and y components of a vector. Also,

$$\bar{X}_2 = (\bar{\rho}_{TX} - \bar{\rho}_{RX}) + (H + \zeta/m)(\bar{s}_{TX} - \bar{s}_{RX}). \tag{4.69}$$

The x component is given as

$$X_{2,x} = (\bar{\rho}_{TX,x} - \bar{\rho}_{RX,x}) + (H + \zeta/m)(\bar{s}_{TX,x} - \bar{s}_{RX,x}), \tag{4.70}$$

where $\rho_{i,x}$ and $s_{i,x}$ are the x components of $\bar{\rho}_i$ and $\bar{s}_i$, i is TX or RX, denoting transmitter or receiver. Similarly for the y component

$$X_{2,y} = (\bar{\rho}_{TX,y} - \bar{\rho}_{RX,y}) + (H + \zeta/m)(\bar{s}_{TX,y} - \bar{s}_{RX,y}). \tag{4.71}$$

The task of calculating the water return has been reduced to calculating the integrals $I_1(\zeta)$, $I_2(\zeta)$, and $I_3(\zeta)$. For the computation of the integral I_1 we make use of the integral

$$\frac{1}{2\pi}\int e^{-ax^2}\, e^{jbx}\, dx = \frac{1}{2\sqrt{\pi a}} e^{-b^2/4a} \tag{4.72}$$

which can be calculated by completing the squares in the exponents and recalling the normal density. Writing I_1 in its x and y components and using (4.72), we obtain

$$I_1(\zeta) \ = \ \left(\pi(H + \zeta/m)^2 \left(\theta_{RX,x}^2 + \theta_{TX,x}^2\right)^{\frac{1}{2}} \left(\theta_{RX,y}^2 + \theta_{TX,y}^2\right)^{\frac{1}{2}}\right)^{-1}$$

$$\cdot \exp\left(-\frac{(\rho_{TX,x}-\rho_{RX,x}\ +\ (H+\zeta/m)\ (s_{TX,x}-s_{RX,x}))^2}{(H+\zeta/m)^2\ (\theta^2_{RX,x}+\theta^2_{TX,x})}\right)$$
$$\cdot \exp\left(-\frac{(\rho_{TX,y}-\rho_{RX,y}\ +\ (H+\zeta/m)\ (s_{TX,y}-s_{RX,y}))^2}{(H+\zeta/m)^2\ (\theta^2_{RX,y}+\theta^2_{TX,y})}\right). \qquad (4.73)$$

To calculate I_2, we insert

$$H(\zeta,\bar{\kappa},\bar{0},\tau)=\exp\left(-\frac{1}{3m}\zeta\tau c\kappa^2\right), \qquad (4.74)$$

where $\kappa^2=|\bar{\kappa}|^2=(\kappa_x^2+\kappa_y^2)$, and again use (4.72), which yields

$$\begin{aligned} I_2(\zeta) \ = \ & \left(\pi(H+\zeta/m)^2\left(\theta^2_{RX,x}+\theta^2_{TX,x}+\frac{4\zeta\tau c}{3m(H+\zeta/m)^2}\right)^{\frac{1}{2}}\right. \\ & \left.\cdot\left(\theta^2_{RX,y}+\theta^2_{TX,y}+\frac{4\zeta\tau c}{3m(H+\zeta/m)^2}\right)^{\frac{1}{2}}\right)^{-1} \\ & \cdot\exp\left(-\frac{((\rho_{TX,x}-\rho_{RX,x})\ +\ (H+\zeta/m)\ (s_{TX,x}-s_{RX,x}))^2}{(H+\zeta/m)^2\ (\theta^2_{RX,x}+\theta^2_{TX,x})+\frac{4\zeta\tau c}{3m}}\right) \\ & \cdot\exp\left(-\frac{((\rho_{TX,y}-\rho_{RX,y})\ +\ (H+\zeta/m)\ (s_{TX,y}-s_{RX,y}))^2}{(H+\zeta/m)^2\ (\theta^2_{RX,y}+\theta^2_{TX,y})+\frac{4\zeta\tau c}{3m}}\right). \end{aligned} \qquad (4.75)$$

In $I_3(\zeta)$,

$$\begin{aligned} & g(z,\tau)H(z,\bar{\kappa},\bar{0},\tau)\ *_t\ g(z,\tau)H(z,\bar{\kappa},-z\bar{\kappa},\tau)= \\ & \quad\int g(\zeta,\tau')H(\zeta,\bar{\kappa},\bar{0},\tau)H(\zeta,\bar{\kappa},-z\bar{\kappa},\tau)g(\zeta,\tau-\tau')\ d\tau', \end{aligned} \qquad (4.76)$$

where

$$\begin{aligned} H(\zeta,\bar{\kappa},\bar{0},\tau)H(\zeta,\bar{\kappa},-z\bar{\kappa},\tau) \ &= \ \exp\left(-\frac{1}{3m}\zeta\tau' c\kappa^2\right)\exp\left(-\frac{1}{3m}\zeta(\tau-\tau')c\kappa^2\right) \\ &= \ \exp\left(-\frac{1}{3m}\zeta\tau c\kappa^2\right)=H(\zeta,\bar{\kappa},\bar{0},\tau). \end{aligned} \qquad (4.77)$$

Thus,

$$I_3(\zeta)=(g(\zeta,\tau)\ *_t\ g(\zeta,\tau))\ I_2(\zeta)\ , \qquad (4.78)$$

where

$$g(\zeta,\tau) \;*_t\; g(\zeta,\tau) = \frac{\mu}{\sigma^2\,\Gamma(2\mu^2/\sigma^2)}\left(\frac{\mu\tau}{\sigma^2}\right)^{2\mu^2/\sigma^2-1}\exp\left(-\frac{\mu\tau}{\sigma^2}\right) \tag{4.79}$$

for $\tau \geq 0$. This can be calculated by using the characteristic function of the gamma distribution.

The bottom return contains the integrals I_1, I_2, and I_3 too, but not the integral over τ. Thus, for the bottom return, we have

$$\begin{aligned} P_{bottom}(\zeta) \;=\; & C_{bottom}\, e^{-2aD}\,\Big[\delta(\tau)\, e^{-2bD} I_1(D) \\ & + 2e^{-bD}\,(1-e^{-bD})\, e^{-ac\tau/m}\, g(D,\tau) I_2(D) \\ & + (1-e^{-bD})^2\, e^{-ac\tau/m} I_3(D)\Big], \end{aligned} \tag{4.80}$$

where $\zeta = D + c\tau/2m$ and D is the bottom depth.

Inserting the transmitter and receiver aperture and radiation patterns into the shadow return, we have

$$\begin{aligned} P_{shadow}(\zeta,\bar{\rho}_{trgt}) = C_{shadow} & \int_0^{2(\zeta-D)m/c} \frac{c}{2m} \int\!\!\cdots\!\!\int e^{-Y_1-Y_2+jY_3+jY_4} \\ & \cdot\,(K(\zeta,\bar{\kappa}_1,\bar{0},\tau) \;*_t\; K(\zeta,\bar{\kappa}_2,-\zeta\bar{\kappa}_2,\tau))\, \frac{d\bar{\kappa}_1}{(2\pi)^2}\, \frac{d\bar{\kappa}_2}{(2\pi)^2}\, d\tau, \end{aligned} \tag{4.81}$$

where

$$\begin{aligned} Y_1 \;=\; & \frac{1}{4}(H+\zeta/m)^2\,\left(\kappa_{1,x}^2\theta_{TX,x}^2 + \kappa_{1,y}^2\theta_{TX,y}^2\right) \\ Y_2 \;=\; & \frac{1}{4}(H+\zeta/m)^2\,\left(\kappa_{2,x}^2\theta_{RX,x}^2 + \kappa_{2,y}^2\theta_{RX,y}^2\right) \\ Y_3 \;=\; & \kappa_{1,x}\,(\rho_{TX,x} + (H+\zeta/m)s_{TX,x} - \rho_{trgt,x}) \\ & + \kappa_{1,y}\,(\rho_{TX,y} + (H+\zeta/m)s_{TX,y} - \rho_{trgt,y}) \\ Y_4 \;=\; & -\kappa_{2,x}\,(\rho_{RX,x} + (H+\zeta/m)s_{RX,x} - \rho_{trgt,x}) \\ & - \kappa_{2,y}\,(\rho_{RX,y} + (H+\zeta/m)s_{RX,y} - \rho_{trgt,y})\,. \end{aligned} \tag{4.82}$$

Inserting $K(z,\bar{\kappa}_1,\bar{0},\tau) *_t K(z,\bar{\kappa}_2,-z\bar{\kappa}_2,\tau)$ from (4.60) into the shadow return expression, we have

$$
\begin{aligned}
&P_{shadow}(\zeta,\bar{\rho}_{trgt}) = \\
&C_{shadow} \int_0^{2(\zeta-D)m/c} \frac{c}{2m}\, e^{-2a\zeta} \Bigg[\delta(\tau)\, e^{-2b\zeta} \underbrace{\iint e^{-Y_1+jY_3}\, \frac{d\bar{\kappa}_1}{(2\pi)^2}}_{J_1(\zeta)} \underbrace{\iint e^{-Y_2+jY_4}\, \frac{d\bar{\kappa}_2}{(2\pi)^2}}_{J_2(\zeta)} \\
&+e^{-b\zeta}\,(1-e^{-b\zeta})\, e^{-ac\tau/m}\, g(\zeta,\tau)\, J_1(\zeta) \underbrace{\iint e^{-Y_2+jY_4}\, H(\zeta,\bar{\kappa}_2,-\zeta\bar{\kappa}_2,\tau)\, \frac{d\bar{\kappa}_2}{(2\pi)^2}}_{J_3(\zeta)} \\
&+e^{-b\zeta}\,(1-e^{-b\zeta})\, e^{-ac\tau/m}\, g(\zeta,\tau)\, J_2(\zeta) \underbrace{\iint e^{-Y_1+jY_3}\, H(\zeta,\bar{\kappa}_1,\bar{0},\tau)\, \frac{d\bar{\kappa}_1}{(2\pi)^2}}_{J_4(\zeta)} \\
&+(1-e^{-b\zeta})^2\, e^{-ac\tau/m} \underbrace{\int\!\cdots\!\int e^{-Y_1-Y_2+jY_3+jY_4} p(\zeta,\bar{\kappa}_1,\bar{\kappa}_2,\tau)\, \frac{d\bar{\kappa}_1}{(2\pi)^2}\, \frac{d\bar{\kappa}_2}{(2\pi)^2}}_{J_5(\zeta)} \Bigg]\, d\tau.
\end{aligned}
\tag{4.83}
$$

where

$$
p(\zeta,\bar{\kappa}_1,\bar{\kappa}_2,\tau) = g(\zeta,\tau)H(\zeta,\bar{\kappa}_1,\bar{0},\tau) \;*_t\; g(\zeta,\tau)H(\zeta,\bar{\kappa}_2,-\zeta\bar{\kappa}_2,\tau). \tag{4.84}
$$

For the evaluation of J_1, we insert Y_1 and Y_3 from (4.82) and use (4.72), which yields

$$
\begin{aligned}
J_1(\zeta) \;=\; & \left(\pi(H+\zeta/m)^2\, \theta_{TX,x}\, \theta_{TX,y}\right)^{-1} \\
& \cdot \exp\left(-\frac{(\rho_{TX,x}+(H+\zeta/m)\, s_{TX,x}-\rho_{trgt,x})^2}{(H+\zeta/m)^2\, \theta_{TX,x}^2}\right) \\
& \cdot \exp\left(-\frac{(\rho_{TX,y}+(H+\zeta/m)\, s_{TX,y}-\rho_{trgt,y})^2}{(H+\zeta/m)^2\, \theta_{TX,y}^2}\right).
\end{aligned}
\tag{4.85}
$$

Similarly,

$$
\begin{aligned}
J_2(\zeta) \;=\; & \left(\pi(H+\zeta/m)^2\, \theta_{RX,x}\, \theta_{RX,y}\right)^{-1} \\
& \cdot \exp\left(-\frac{(\rho_{RX,x}+(H+\zeta/m)\, s_{RX,x}-\rho_{trgt,x})^2}{(H+\zeta/m)^2\, \theta_{RX,x}^2}\right)
\end{aligned}
$$

$$\cdot \exp\left(-\frac{\left(\rho_{RX,y} + (H + \zeta/m)\, s_{RX,y} - \rho_{trgt,y}\right)^2}{(H + \zeta/m)^2\, \theta^2_{RX,y}}\right). \tag{4.86}$$

The calculation of $J_3(\zeta)$ is performed similarly after recalling (4.59) and inserting (4.74). We obtain

$$\begin{aligned} J_3(\zeta) \;=\; & \left(\pi(H + \zeta/m)^2 \left(\theta^2_{RX,x} + \frac{4\zeta\tau c}{3m(H + \zeta/m)^2}\right)^{\frac{1}{2}}\right. \\ & \left. \cdot \left(\theta^2_{RX,y} + \frac{4\zeta\tau c}{3m(H + \zeta/m)^2}\right)^{\frac{1}{2}}\right)^{-1} \\ & \cdot \exp\left(-\frac{\left(\rho_{RX,x} + (H + \zeta/m)\, s_{RX,x} - \rho_{trgt,x}\right)^2}{(H + \zeta/m)^2\, \theta^2_{RX,x} + \frac{4\zeta\tau c}{3m}}\right) \\ & \cdot \exp\left(-\frac{\left(\rho_{RX,y} + (H + \zeta/m)\, s_{RX,y} - \rho_{trgt,y}\right)^2}{(H + \zeta/m)^2\, \theta^2_{RX,y} + \frac{4\zeta\tau c}{3m}}\right). \end{aligned} \tag{4.87}$$

Similarly,

$$\begin{aligned} J_4(\zeta) \;=\; & \left(\pi(H + \zeta/m)^2 \left(\theta^2_{TX,x} + \frac{4\zeta\tau c}{3m(H + \zeta/m)^2}\right)^{\frac{1}{2}}\right. \\ & \left. \cdot \left(\theta^2_{TX,y} + \frac{4\zeta\tau c}{3m(H + \zeta/m)^2}\right)^{\frac{1}{2}}\right)^{-1} \\ & \cdot \exp\left(-\frac{\left(\rho_{TX,x} + (H + \zeta/m)\, s_{TX,x} - \rho_{trgt,x}\right)^2}{(H + \zeta/m)^2\, \theta^2_{TX,x} + \frac{4\zeta\tau c}{3m}}\right) \\ & \cdot \exp\left(-\frac{\left(\rho_{TX,y} + (H + \zeta/m)\, s_{TX,y} - \rho_{trgt,y}\right)^2}{(H + \zeta/m)^2\, \theta^2_{TX,y} + \frac{4\zeta\tau c}{3m}}\right). \end{aligned} \tag{4.88}$$

The calculation of $J_5(\zeta)$ requires the calculation of $p(\zeta, \bar{\kappa}_1, \bar{\kappa}_2, \tau)$, given in (4.84). We can express $g(\zeta,\tau)H(\zeta,\bar{\kappa}_1,\bar{0},\tau)$ and $g(\zeta,\tau)H(\zeta,\bar{\kappa}_2,-\zeta\bar{\kappa}_2,\tau)$ as gamma distributions within scalar factors. Then, $p(\zeta,\bar{\kappa}_1,\bar{\kappa}_2,\tau)$ is a time convolution of two gamma distributions corresponding to random variables τ_1 and τ_2. In that case, $p(\zeta,\bar{\kappa}_1,\bar{\kappa}_2,\tau)$ itself becomes a gamma distribution, let us say, for random variable τ_3, where $\tau_3 = \tau_1 + \tau_2$. Assuming τ_1 and τ_2 independent, and calculating the mean and variance of τ_3, we obtain,

$$p(\zeta,\bar{\kappa}_1,\bar{\kappa}_2,\tau) = \frac{c_0^{2x}}{c_1^x\, c_2^x}\left(\frac{c_3^y}{\Gamma(y)}\, \tau^{y-1}\, \exp\left(-c_3\tau\right)\right) \tag{4.89}$$

for $\tau > 0$, where

$$\begin{aligned} x &= \frac{\mu^2}{\sigma^2} \\ c_0 &= \frac{\mu}{\sigma^2} \\ c_1 &= c_0 + Z_1 \\ c_2 &= c_0 + Z_2 \\ c_3 &= \frac{c_1 c_2 (c_1 + c_2)}{c_1^2 + c_2^2} \\ Z_1 &= \frac{c\kappa_1^2 \zeta}{3m} \\ Z_2 &= \frac{c\kappa_2^2 \zeta}{3m} \\ y &= \frac{x(c_1 + c_2)^2}{c_1^2 + c_2^2} \end{aligned} \tag{4.90}$$

with μ and σ^2 as the mean and variance of the gamma distribution with parameters x and c_0. This is a difficult expression to integrate over κ_1 or κ_2. We can approximate this as

$$p(\zeta, \bar{\kappa}_1, \bar{\kappa}_2, \tau) \approx (g(\zeta, \tau) \; *_t \; g(\zeta, \tau)) \; \exp(-\tau Z_1) \; \exp(-\tau Z_2). \tag{4.91}$$

Then,

$$J_5(\zeta) = (g(\zeta, \tau) \; *_t \; g(\zeta, \tau)) \; J_3(\zeta) J_4(\zeta). \tag{4.92}$$

This completes the calculation of the shadow return.

The target return is then

$$\begin{aligned} P_{target}(\zeta, \bar{\rho}_{trgt}) = \; & C_{target} \, e^{-2aD} \Big[\delta(\tau) \, e^{-2bD} J_1(D) J_2(D) \\ & + e^{-bD} \, (1 - e^{-bD}) \, e^{-ac\tau/m} \, g(D, \tau) J_1(D) J_3(D) \\ & + e^{-bD} \, (1 - e^{-bD}) \, e^{-ac\tau/m} \, g(D, \tau) J_2(D) J_4(D) \\ & + (1 - e^{-bD})^2 \, e^{-ac\tau/m} J_5(D) \Big]. \end{aligned} \tag{4.93}$$

4.3.2 Simulated PMT/CCD returns

We have written a program in MATLAB and C to compute the lidar returns using the bistatic lidar equations derived above. The program performs the numerical integration using Gauss-Legendre quadrature [113, 114]. The program can compute the background return for different water types and the return from a submerged target at a specified location. Our analysis assumes a flat ocean surface. There are studies in the literature that discuss how to incorporate a nonflat surface [115].

We compute the PMT output for a monostatic setting of the transmitter and the PMT. A simulation result is shown in Figure 4.7. The simulated object is 6.4 m (21 ft) deep. The dashed curve is the background return from the water column without the object.

For the CCD return, we use a bistatic lidar return computation. Assuming that each pixel is a separate receiver element, we set different receiver position and angle offsets for each pixel of the CCD. An example simulation of a CCD return is shown in Figure 4.8. The corresponding CCD return from the CEFT data is shown in Figure 4.9. Notice that the simulated return does not account for noise. For a better visual comparison, we add Gaussian noise to the simulated data and display the result in Figure 4.10. The SNR is 20 dB. We compute SNR using the formula, $\text{SNR} = 20\log_{10}(\sigma_x/\sigma_n)$, where σ_x^2 and σ_n^2 are the signal energy and noise variance, respectively. The SNR level in the real data shown in Figure 4.9 is 28 dB, as recorded in the CEFT database. The method used for SNR calculation of the real data is classified. It might be different than ours. The simulated lidar return matches the characteristics of the real data very well. Notice the Gaussian structure of the base of the mesh surfaces. This is due to the spatially Gaussian structure of the laser beam, which we take into account in our simulation.

4.4 Image Reconstruction Results

Taking CCD and PMT measurements at various angles, we obtain different planar slices and linear traces of the 3-D Fourier transform of the reflectivity. An image can then be formed by 3-D inverse Fourier transformation. However, it is necessary to employ interpolation of the data onto a Cartesian grid prior to inverse Fourier transformation.

We performed reconstructions from both simulated and real data. In our simulations, we generally used the same system parameters as for the real data. One exception was the elevation angle θ. The simulations did not work well for the elevation angles at which the real images were obtained. This is because the analytic lidar return expressions are for the small-angle scattering scenario and require the incident angle to be small. We generated synthetic data for elevation angles that were 8 degrees offset from those of the real data. This still provided a fair basis for comparison because the test object was circularly symmetric. Almost the same real data would have been obtained if the real CCD images had been collected at the elevation angles of the simulated data. Angular diversity is important in providing reconstruction quality. Therefore, we used the same range of angles in both reconstructions. We assumed a CCD of size 32×32 for the simulated data, and we decimated the real CCD images accordingly in our results that follow.

For reconstruction from the real data, we chose 6 CCD images from the CEFT data, which consisted of 22 shots. We performed this selection in order not to simulate all 22 cases, and in order to include in the reconstruction only the images with high SNR. The test object was a mine with a 1-m diameter, at a depth of 21 ft. We chose shots with high SNR and, at the same time, tried to maintain high angular diversity. All 22 CCD images of the CEFT data are shown in Figure 4.2, along with image number, SNR, and orientation of the shot in θ and ϕ. Figure 4.11 shows SNR, θ, and ϕ as a function of image number. We chose shots 2, 4, 5, 6, 12, and 16. In-water elevation angles θ for these shots were 17.67°, 17.42°, 16.76°, 13.16°, 14.42°, 16.15°, respectively, and azimuth angles ϕ were 140.45°, 138.79°, 168.35°, 183.23°, 179.62°, 201.95°, respectively. The average size of the beam spot on the water surface was 11.6 m. The reconstruction results are shown in Figure 4.12. Displayed images are the cross sections of the 3-D reconstruction at $z = 0$, $x = 0$, and $y = 0$. The reconstruction from the simulated data is shown in Figure 4.13. The reconstruction from the simulated data with 20 dB of Gaussian noise is shown in Figure 4.14. In these reconstructions, we used only CCD data; we did not include PMT data. This is because the PMT data were found to be of no help in the reconstruction, since the spatial length of the laser pulse was comparable to the object size [116].

The reconstructions from both simulated and real data display the same characteristics. The reconstruction from the real data, however, is more smeared out compared to that of the noise-free simulated data. Reconstruction from the simulated noisy data is closer to the real case. Also, in the real data case, the CCD images involve effects of the wavy ocean surface, which usually is in the form of smearing [115]. The range of angles in θ and ϕ were approximately 4.5° and 63.2°, respectively. Since the angular diversity is large in the ϕ dimension, we obtained good resolution in the x-y plane.

Our image reconstruction process was based on Fourier inversion, which does not account for several factors that are present in the actual imaging scenario. These and a few other related factors are as follows.

(1) The Fourier based reconstruction assumes the integral is a line integral through the object without taking into account the opacity of the object.

(2) The tomographic model assumes that the contribution of a point reflector to a projection is independent of the view angle. In practice, a Lambertian scattering model is probably more accurate, where the brightness falls off with the cosine of the angle from the surface normal. Accounting for Lambertian scattering via a CLEAN approach to image reconstruction can significantly improve 3-D image quality [117].

(3) There is an exponential decay term in the integral for the CCD returns, because of the absorption in the medium. In this case, the projection integral is known as *attenuated* or *exponential* Radon transform [3, 118]. There are studies on the inversion of this type of projections [119–124].

(4) The size of the beam spot on the surface of the water may be different from shot to shot, depending on the altitude of the aircraft, elevation angle, etc. Consequently, the dimensions of each CCD image used in a reconstruction are different. Before the reconstruction, each image should be resampled to a larger or smaller grid to make the size of the images equal. This is an interpolation between two uniform rectangular grids, and can be performed precisely [125].

(5) In the actual system, each CCD image has a different noise level. Thus, a noise cancellation process needs to consider the CCD images altogether to estimate each level and apply an appropriate parameter for noise cancellation. It is also an interesting problem to inherently account for noise in the reconstruction process. Another interesting

problem would be to select from a noisy collection of CCD images the optimum set of projections that will trade off angular diversity and the effects of noise.

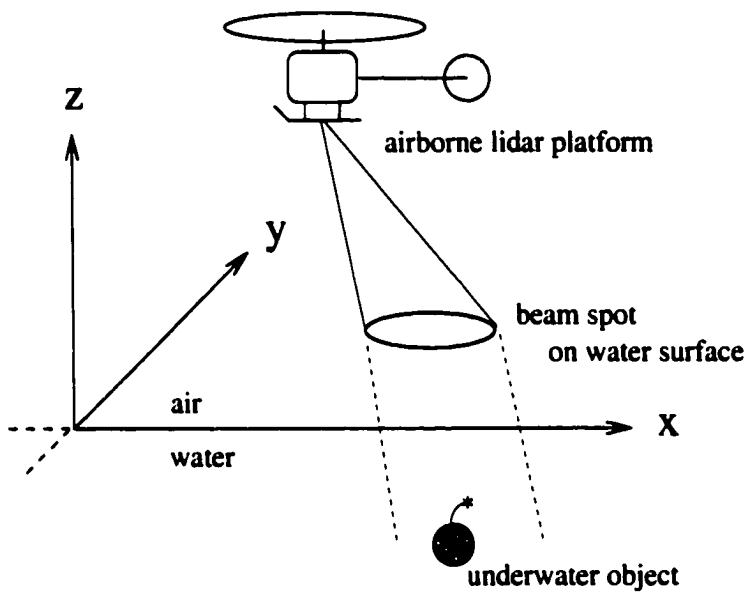

Figure 4.1 Data collection geometry for lidar imaging of underwater objects.

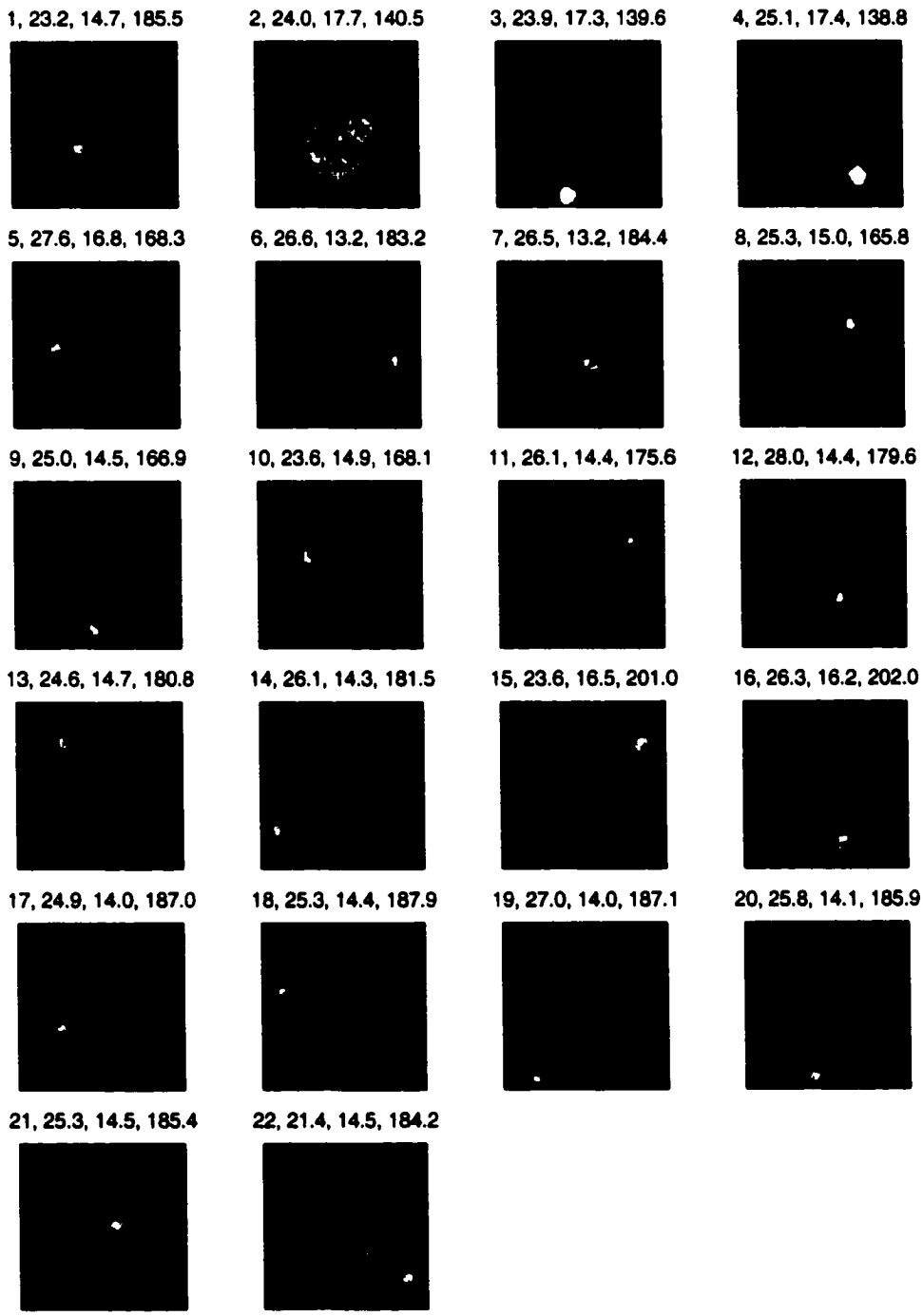

Figure 4.2 CCD images from CEFT database along with image number, SNR, and orientation of the shot in θ and ϕ.

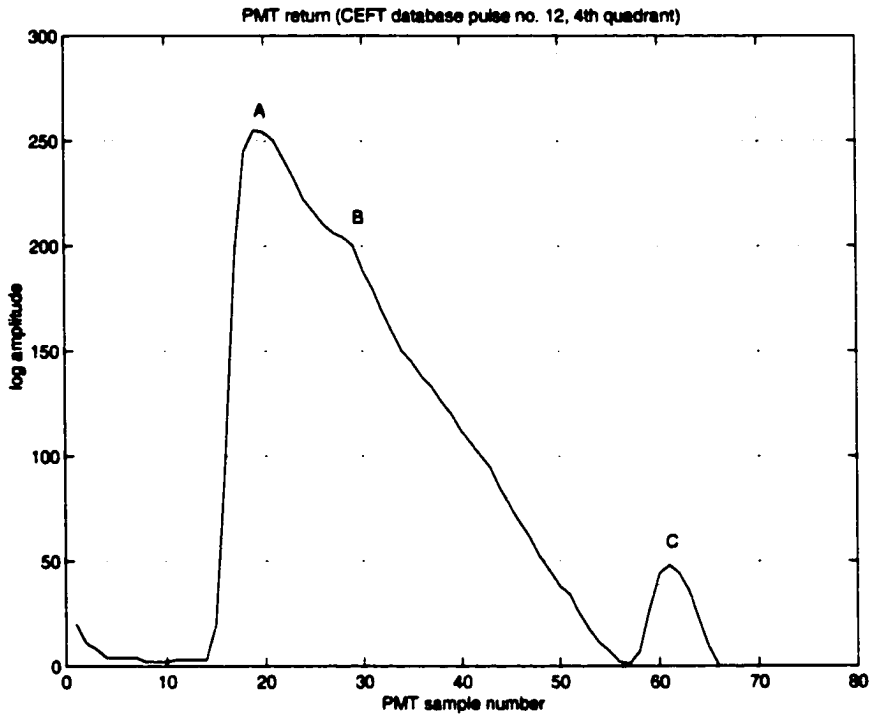

Figure 4.3 Real PMT data (CEFT database, shot 12, fourth quadrant).

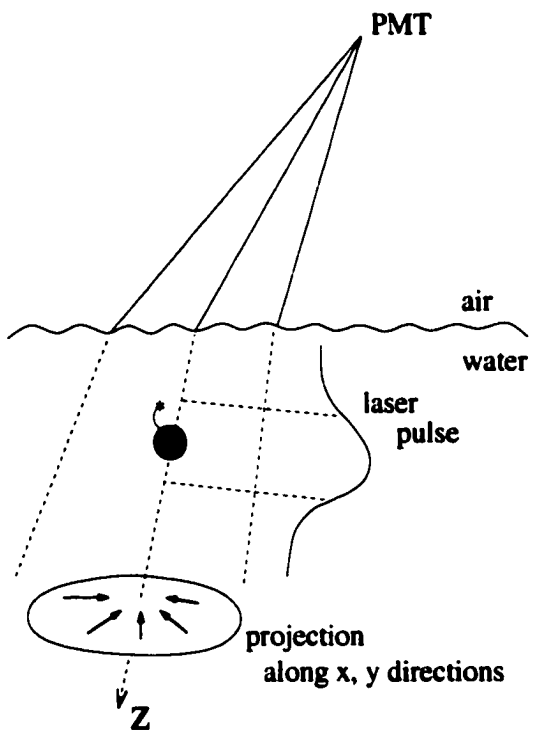

Figure 4.4 Tomographic interpretation of the PMT output.

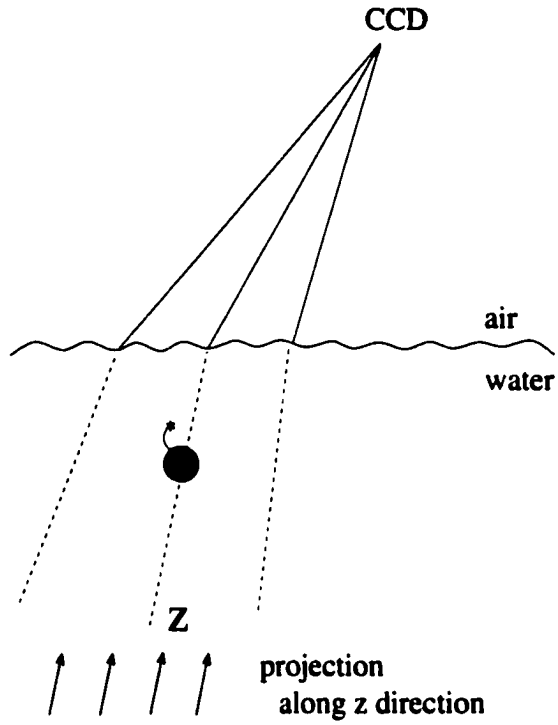

Figure 4.5 Tomographic interpretation of the CCD output.

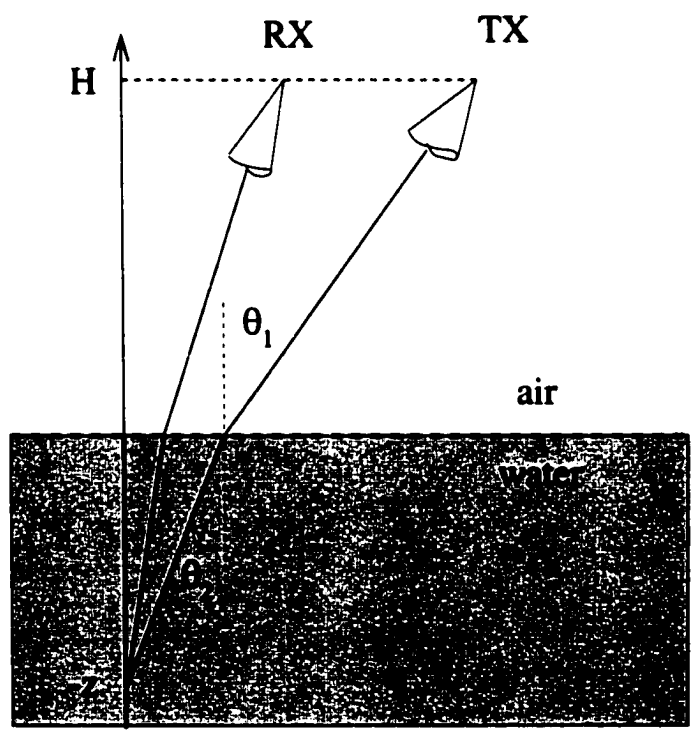

Figure 4.6 Bistatic lidar geometry.

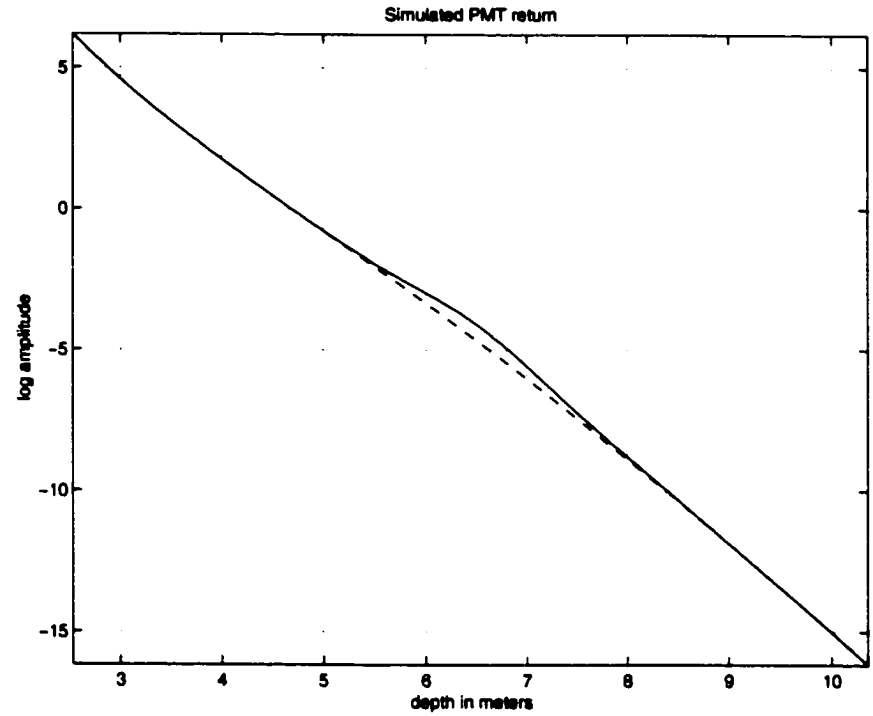

Figure 4.7 Simulated PMT return (solid). Dashed line is for background return from water.

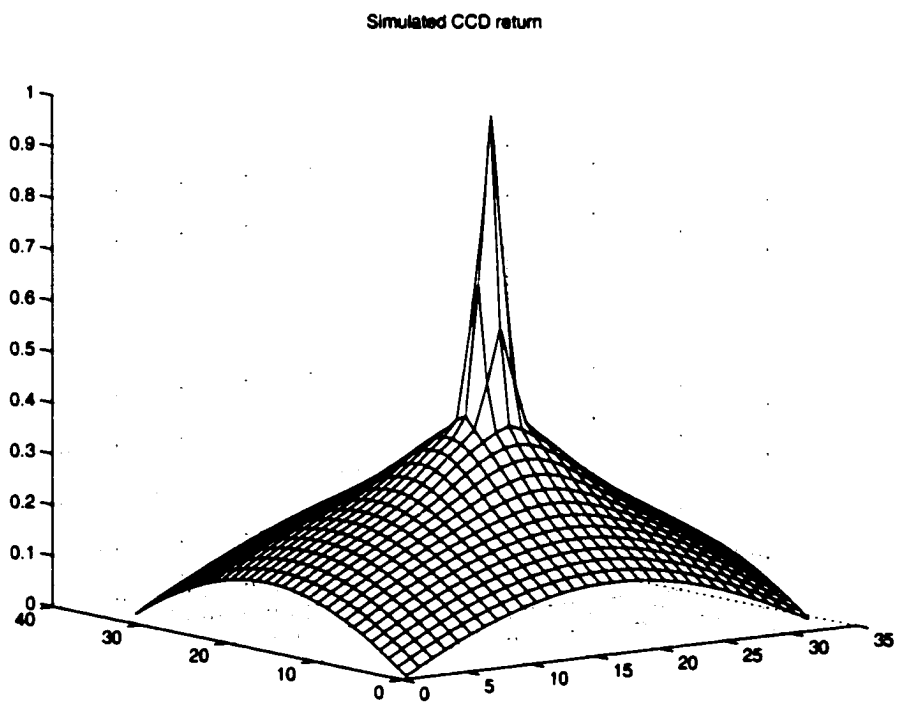

Figure 4.8 Simulated CCD return.

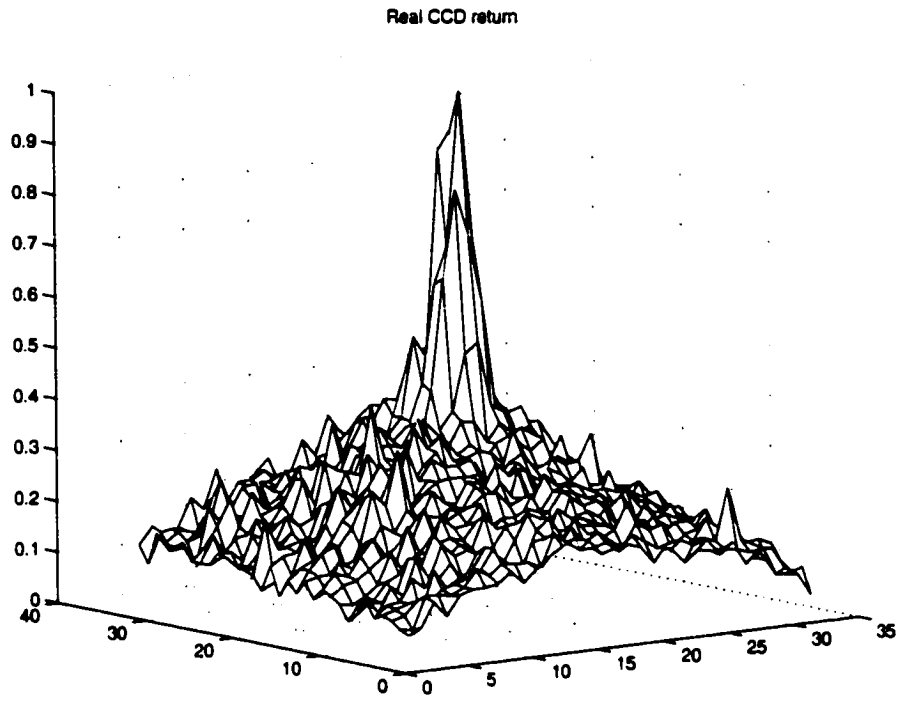

Figure 4.9 Real CCD return from CEFT data.

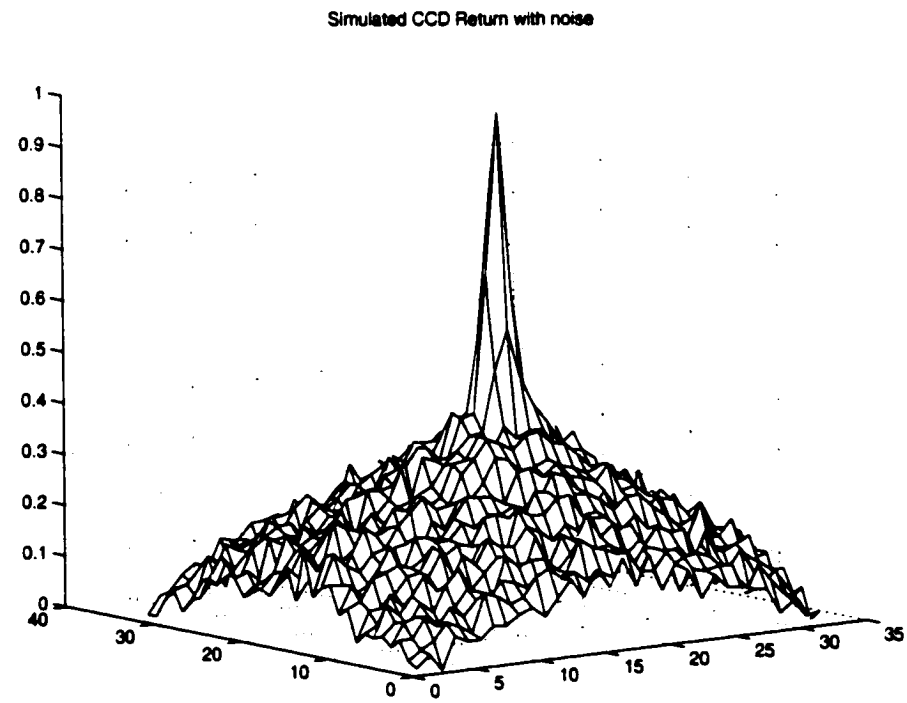

Figure 4.10 Simulated CCD return with noise.

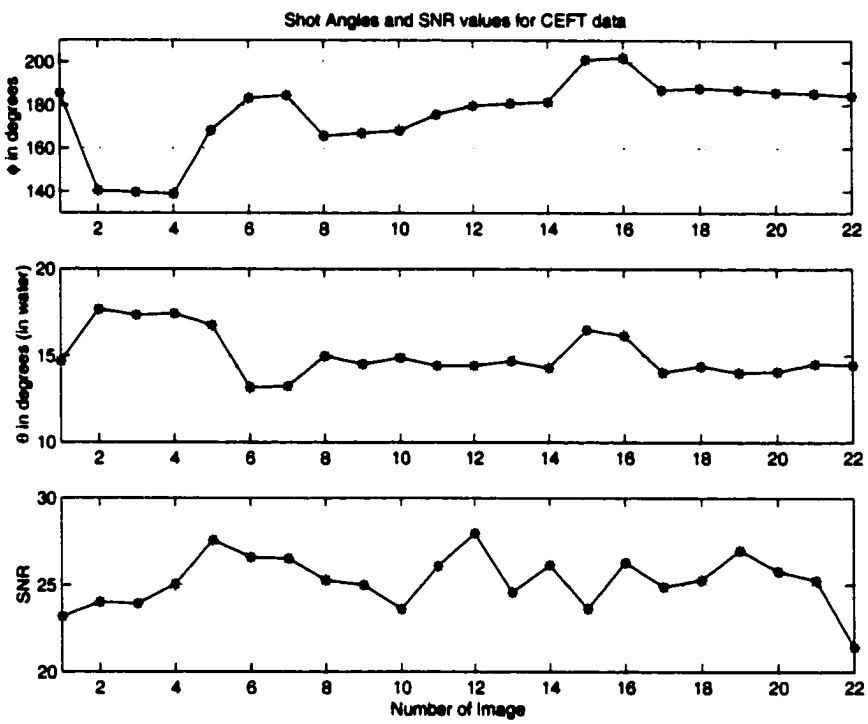

Figure 4.11 Shot angles and listed SNR values of the 22 CCD images from CEFT database.

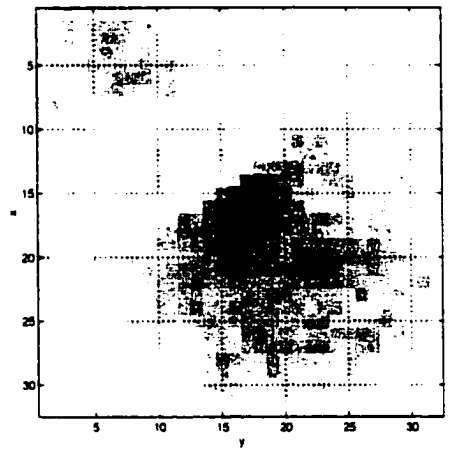

(a)

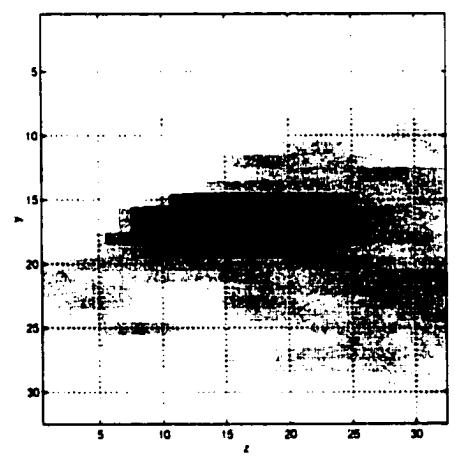

(b)

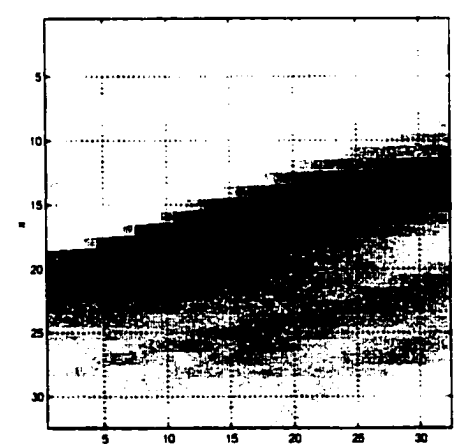

(c)

Figure 4.12 Reconstruction from real data (CEFT). Displayed images are the cross sections of the 3-D reconstruction at (a) $z = 0$, (b) $x = 0$, and (c) $y = 0$.

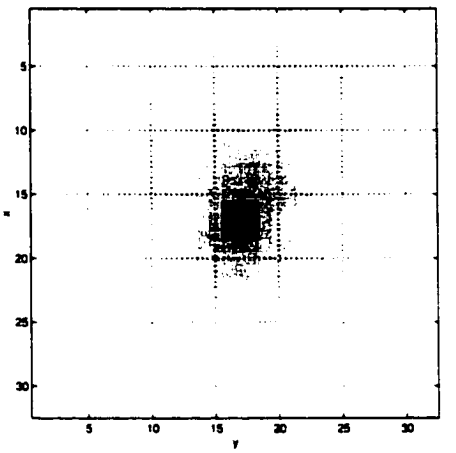

(a)

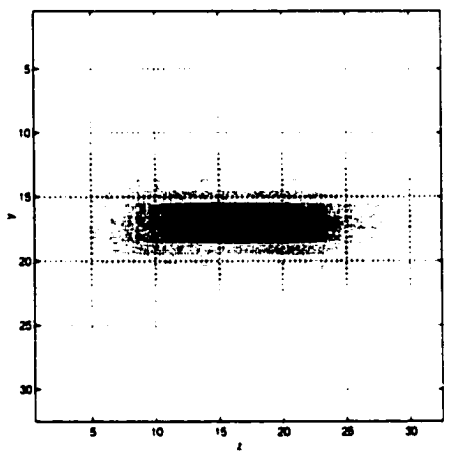

(b)

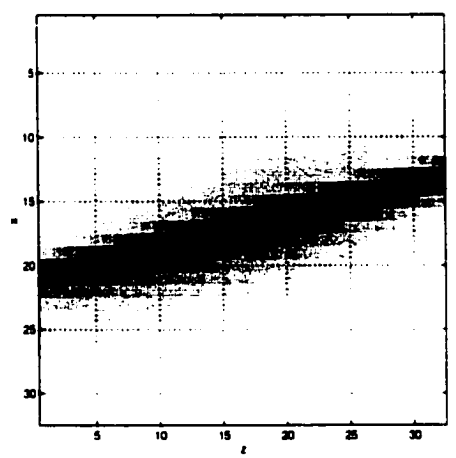

(c)

Figure 4.13 Reconstruction from simulated data. Displayed images are the cross sections of the 3-D reconstruction at (a) $z = 0$, (b) $x = 0$, and (c) $y = 0$.

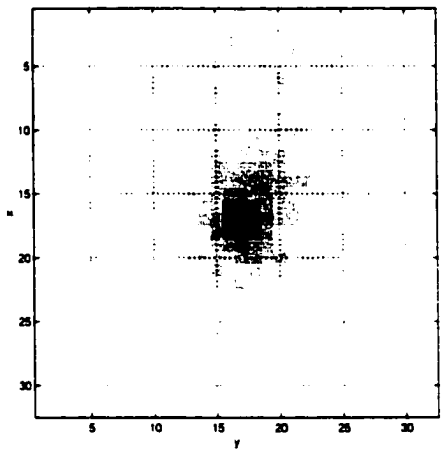

(a)

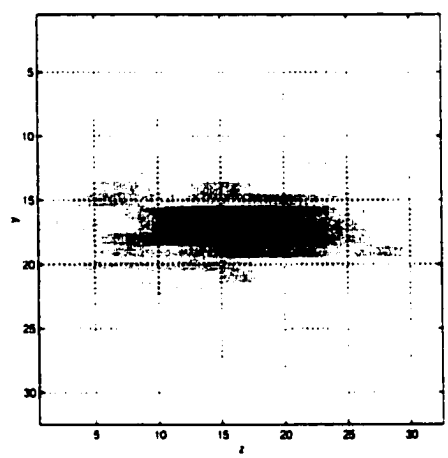

(b)

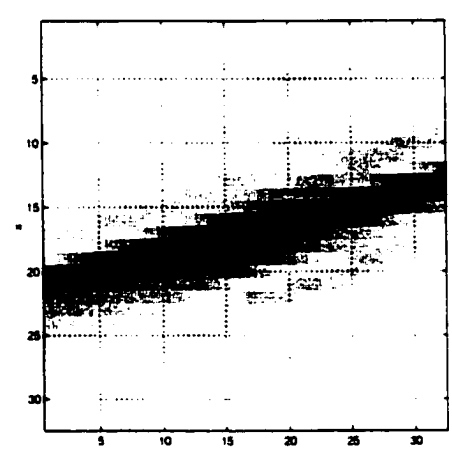

(c)

Figure 4.14 Reconstruction from simulated data with noise. Displayed images are the cross sections of the 3-D reconstruction at (a) $z = 0$, (b) $x = 0$, and (c) $y = 0$.

CHAPTER 5

CONCLUSIONS AND FURTHER WORK

In the study of SAR imaging of runways, we investigated the problem of runway imaging from an aircraft approaching for landing [79, 126, 127]. Specifically, we studied the performance of the $\omega - k$ algorithm in this highly squinted scenario, which necessitates incorporating the wavefront curvature into the image formation process. We demonstrated the aberrations that the algorithm can produce when the squint angle is close to 90°. Based on our careful analysis of the algorithm, we explained the source of these aberrations being mainly as the inaccuracy of the interpolation. Furthermore, we showed that the interpolation accuracy can be improved by increasing the number of temporal samples in our interpolation scheme, which exploits the structure of the unevenly spaced data so as to use a 1-D interpolation to interpolate 2-D data. The computational complexity of the interpolation increases only linearly in the number of temporal frequency samples.

We also investigated a general inversion method (GIM) which accurately models the wavefront curvature. We compared the results with those of the $\omega - k$ algorithm. Since GIM is a direct solution of the measurement equation, it is expected to produce results closer to the optimal solution. Since GIM is computationally more expensive and the performance of the $\omega - k$ algorithm can be improved by increasing the number of temporal samples, which in turn increases the complexity, for fair comparison, we let both algorithms use the same amount of computation. In the simulations, the $\omega - k$ algorithm produced comparable results to those of GIM. However, since GIM is inherently robust to noise, results of GIM were superior in the noisy case.

We presented a solution to the left-right ambiguity problem of runway imaging using the $\omega - k$ algorithm. We showed that the ambiguity can be resolved using a second

antenna that is spatially separated from the main antenna. We presented simulation results supporting our solution.

The point target simulations reported in Section 2.3.6 were obtained by using the software mentioned in Section 2.3.5. We had hoped to include simulations of larger, realistic targets obtained from sophisticated computational electromagnetics software such as Xpatch or FISC [128, 129]. However, Xpatch does not provide near-field data and the frequency of operation in our application is very high for FISC, which would require an unreasonably large computer memory. A new version of Xpatch, capable of performing near-field simulations at high frequencies, was scheduled for release early in the year 2000. Unfortunately, this schedule did not hold and we could not include simulations obtained by this new software. This task is left for further research.

In the study of imaging of objects buried in soil, an acoustic approach was pursued, with the primary purpose of detecting and imaging cultural artifacts [96, 130, 131]. A mathematical model and associated computer software were developed in order to simulate the signals acquired by the actual experimental system. We developed a SAR-type reconstruction algorithm via the application of synthetic aperture theory for acoustic data collected in a bistatic manner. Subsurface images were reconstructed from simulated data using this algorithm. Objects were detectable, but near-field objects suffered from shifts and smears due to the invalidity of the employed approximations in the near field. The SAR-type reconstruction algorithm was also applied to real data obtained from the experimental system. However, the result was not satisfactory; there was a large amount of clutter in the image, although there were bright spots at the locations of the objects. The reasons for this are the following. (1) The plane-wave approximation for objects close to the surface is invalid. (2) In a SAR reconstruction, azimuth resolution depends on the distance covered by the data acquisition system during illumination of a target by the transmitted beam. In our experimental system, the length of the scan was limited by the size of the box, which presented a complication to successfully applying SAR-type imaging. (3) In our data model we incorporated the attenuation of the medium by using a single parameter for a single frequency. However, the attenuation of the soil is frequency dependent, and high frequency components of the return signals are attenuated so much that they are almost invisible in the return signals. (4) The system

was not designed to focus the transmitted energy. Hence, there were contributions from all directions around the transmitter. To account for wavefront curvature, we formulated processing of the simulated data using the 3-D version of the monostatic $\omega - k$ algorithm which would be expected to provide superior results in the near-field. Implementation and application of this algorithm is left for further research.

In the study of lidar imaging of underwater objects, [116, 132], we formulated the lidar detection and localization problem as a 3-D tomographic reconstruction problem: We described the relation between the airborne CCD/PMT returns and corresponding tomographic projections of an underwater object. Having CCD/PMT data at various angular orientations with respect to the object, a 3-D tomographic reconstruction was obtained. We developed software to simulate lidar returns in PMT and CCD sensors. Our simulator can model multiple scattering and absorption for various water types and system parameters. Our simulator in the acoustic imaging scenario was able to model absorption and scattering, too; however, it was simpler. Here we use a sophisticated analytic model for lidar returns. We also worked with a real data set from a previous study (1998 Competitive Evaluation Field Test (CEFT), Panama City, FL). We presented our reconstruction results from the simulated and real data. Simulated data were found to fit the characteristics of real data very well. Our image reconstruction process was based on Fourier inversion, which does not account for several factors that are present in the actual imaging scenario. For instance, absorption in the medium introduces a decaying exponential in the projection integral in CCD returns. In the real system the CCD can saturate. Also, the noise levels in the real data are different in each shot. Furthermore, Fourier-based inversion assumes that the object is transparent, which is actually not the case. The simulator can be useful in investigation of new algorithms which account for these problems in order to produce better reconstructions.

APPENDIX A

QUADRATURE DEMODULATION AND DERAMPING

The radar return in real passband form is given in (2.6). When the linear FM pulse in (2.1) is inserted into (2.6), we obtain

$$\bar{s}_R(t,y) = \iint_{-\infty}^{\infty} |g(x',y')| \cos\left(\omega_0(t-\frac{2r'_y}{c}) + \alpha(t-\frac{2r'_y}{c})^2 + \psi(x',y')\right) dx'dy'. \quad \text{(A.1)}$$

We pass $\bar{s}_R(t,y)$ through the structure as shown in Figure A.1 where

$$q^c(t) = 2\cos\left(\omega_0(t-\tau_0) + \alpha(t-\tau_0)^2\right) \quad \text{(A.2)}$$

$$q^s(t) = -2\sin\left(\omega_0(t-\tau_0) + \alpha(t-\tau_0)^2\right) \quad \text{(A.3)}$$

and $\tau_0 = \frac{2R_0}{c}$, with R_0 being the distance to the center (X_0, Y_0) of the target scene from the origin of the coordinate system. The structure in Figure A.1 is referred to as a *quadrature demodulator*. It is used to remove the carrier and obtain the in-phase and quadrature components of the complex baseband version of the return signal. When the oscillation phase of the demodulating signals $q^c(t)$ and $q^s(t)$ is $\omega_0(t-\tau_0) + \alpha(t-\tau_0)^2$ as above, instead of $\omega_0 t$ as in the former procedure to remove the carrier, the processing is called *deramping*, and it provides the temporal Fourier transform of the data directly. As a matter of fact, this can be recognized as the chirp transform [133].

Let us concentrate on the upper branch and define

$$\hat{s}^c_R(t,y) = \bar{s}_R(t,y) \cdot q^c(t), \quad \text{(A.4)}$$

which is

$$\hat{s}_R^c(t,y) = \iint_{-\infty}^{\infty} |g_(x',y')|\, 2\cos\underbrace{\left(\omega_0(t-\tau_0)+\alpha(t-\tau_0)^2\right)}_{A} \tag{A.5}$$

$$\cdot\cos\underbrace{\left(\omega_0(t-\frac{2r'_y}{c})+\alpha(t-\frac{2r'_y}{c})^2+\psi(x',y')\right)}_{B}\, dx'dy'. \tag{A.6}$$

We use the trigonometric identities

$$2\cos A\cos B = \cos(A+B)+\cos(B-A) \tag{A.7}$$

$$-2\sin A\cos B = -\sin(A+B)+\sin(B-A), \tag{A.8}$$

by writing

$$A+B = \omega_0(2t-\tau_0-\frac{2r'_y}{c})+\alpha\left[(t-\tau_0)^2+(t-\frac{2r'_y}{c})^2\right]+\psi(x',y') \tag{A.9}$$

$$B-A = \omega_0(t-\frac{2r'_y}{c}-t+\tau_0)+\alpha\left[(t-\frac{2r'_y}{c})^2-(t-\tau_0)^2\right]+\psi(x',y'). \tag{A.10}$$

Notice that the term with the argument $A+B$ has the frequency component $2\omega_0$, which is higher than the cutoff frequency of the lowpass filter. Therefore it is filtered out. To write the remaining expression in a better way we manipulate the $B-A$ term:

$$B-A = -\frac{2}{c}\omega_0(r'_y-R_0)-\frac{4\alpha t}{c}(r'_y-R_0)+\frac{4\alpha}{c^2}(r'^2_y-R_0^2)+\psi(x',y'). \tag{A.11}$$

For the third term, use

$$r'^2_y-R_0^2 = (r'_y-R_0)^2+2R_0(r'_y-R_0). \tag{A.12}$$

Thus, we have

$$B-A = -\frac{2}{c}\left(\omega_0+2\alpha t-2\alpha\tau_0\right)(r'_y-R_0)+\frac{4\alpha}{c^2}(r'_y-R_0)^2+\psi(x',y'). \tag{A.13}$$

Since $\omega = \omega_0 + 2\alpha(t - \tau_0)$ and $k = \omega/c$, we have

$$s_R^c(t,y) = \iint_{-\infty}^{\infty} |g(x',y')| \cos\left(-2k(r'_y - R_0) + \frac{4\alpha}{c^2}(r'_y - R_0)^2 + \psi(x',y')\right) dx'dy', \tag{A.14}$$

Similarly, for the imaginary part, we can obtain

$$s_R^c(y,t) = \iint_{-\infty}^{\infty} |g(x',y')| \sin\left(-2k(r'_y - R_0) + \frac{4\alpha}{c^2}(r'_y - R_0)^2 + \psi(x',y')\right) dx'dy'. \tag{A.15}$$

Finally,

$$s_R(t,y) = s_R^c(t,y) + j s_R^s(t,y) \tag{A.16}$$

yields the following, which was stated in (2.9),

$$s_R(t,y) = \iint_{-\infty}^{\infty} |g(x',y')| \exp\left(j\psi(x',y')\right) \tag{A.17}$$

$$\exp\left(-j2k(r'_y - R_0)\right) \exp\left(j\frac{4\alpha}{c^2}(r'_y - R_0)^2\right) dx'dy'. \tag{A.18}$$

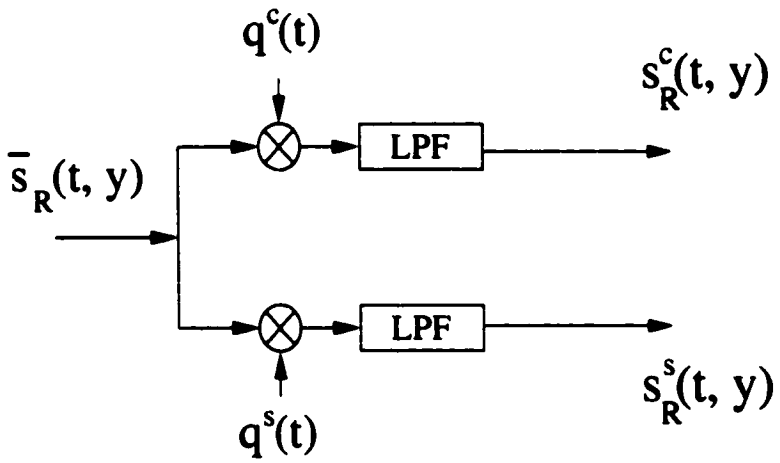

Figure A.1 Quadrature demodulation of the received signal.

APPENDIX B

BESSEL AND HANKEL FUNCTIONS

Here we summarize for easy reference some definitions and asymptotic forms of various Bessel functions which are used elsewhere in this thesis. For further reference, see [98, 134, 135].

Hankel functions of the first and second kind, of order p, are given as

$$H_p^{(1)}(x) = J_p(x) + jY_p(x) \tag{B.1}$$

$$H_p^{(2)}(x) = J_p(x) - jY_p(x) \tag{B.2}$$

where $J_p(x)$ and $Y_p(x)$ are the Bessel functions[1] of the first and second kind of order p, respectively [135, p. 364].

When p is fixed and $|x|$ is large, the Bessel functions can be approximated as

$$J_p(x) = \sqrt{\frac{2}{\pi x}}[A(p,x)\cos\xi - B(p,x)\sin\xi] \qquad |\arg(x)| < \pi \tag{B.3}$$

$$Y_p(x) = \sqrt{\frac{2}{\pi x}}[A(p,x)\sin\xi + B(p,x)\cos\xi] \qquad |\arg(x)| < \pi \tag{B.4}$$

where $\xi = x - (p/2 + 1/4)\pi$. Hence

$$H_p^{(1)}(x) = \sqrt{\frac{2}{\pi x}}[A(p,x) + jB(p,x)]\exp(j\xi) \qquad -\pi < \arg(x) < 2\pi \tag{B.5}$$

$$H_p^{(2)}(x) = \sqrt{\frac{2}{\pi x}}[A(p,x) - jB(p,x)]\exp(-j\xi) \qquad -2\pi < \arg(x) < \pi \tag{B.6}$$

[1] $Y_p(x)$ is also known as the Neumann function and is denoted by $N_p(x)$ [134].

The terms $A(p,x)$ and $B(p,x)$ are given as follows:

$$A(p,x) \approx \sum_{k=0}^{\infty}(-1)^k \frac{\rho(p,2k)}{(2x)^{2k}} \tag{B.7}$$

$$B(p,x) \approx \sum_{k=0}^{\infty}(-1)^k \frac{\rho(p,2k+1)}{(2x)^{2k+1}}, \tag{B.8}$$

where

$$\rho(p,k) = \frac{1}{4^k(k)!} \underbrace{(\mu-1)(\mu-3^2)(\mu-5^2)\ldots}_{k \text{ terms}}, \tag{B.9}$$

and $\mu = 4p^2$. Thus,

$$A(p,x) \approx 1 - \frac{(\mu-1)(\mu-9)}{2!\,(8x)^2} + \frac{(\mu-1)(\mu-9)(\mu-25)(\mu-49)}{4!\,(8x)^4} \tag{B.10}$$

$$B(p,x) \approx \frac{(\mu-1)}{(8x)} - \frac{(\mu-1)(\mu-9)(\mu-25)}{3!\,(8x)^3} + \ldots . \tag{B.11}$$

If p is real and non-negative and x is positive, the remainder after k terms in the expansion of $A(p,x)$ does not exceed the $(k+1)$st term in absolute value and is of the same sign provided that $k > \frac{1}{2}p - \frac{1}{4}$. The same is true of $B(p,x)$ provided that $k > \frac{1}{2}p - \frac{3}{4}$. For $p = 1$,

$$\begin{aligned} A(1,x) &\approx 1 - \frac{(\mu-1)(\mu-9)}{2!\,(8x)^2} + \frac{(\mu-1)(\mu-9)(\mu-25)(\mu-49)}{4!\,(8x)^4} + \ldots \\ &= 1 + \frac{3\cdot 5}{2!\,(8x)^2} - \frac{3^2\cdot 5^2\cdot 7\cdot 9}{4!\,(8x)^4} + \ldots \\ B(1,x) &\approx \frac{(\mu-1)}{(8x)} - \frac{(\mu-1)(\mu-9)(\mu-25)}{3!\,(8x)^3} + \ldots \\ &= \frac{3}{(8x)} - \frac{3^2\cdot 5\cdot 7}{3!\,(8x)^3} + \ldots \end{aligned} \tag{B.12}$$

As $|x| \to \infty$, we have $A(p,x) \asymp 1$ and $B(p,x) \asymp 0$. Thus,

$$H_p^{(1)}(x) \asymp \sqrt{\frac{2}{\pi x}} \exp\left(j(x - (\frac{1}{2}p + \frac{1}{4})\pi)\right) \tag{B.13}$$

$$H_p^{(2)}(x) \asymp \sqrt{\frac{2}{\pi x}} \exp\left(-j(x - (\frac{1}{2}p + \frac{1}{4})\pi)\right), \tag{B.14}$$

which is the standard approximation given in most books [98]. For $p = 1$,

$$H_1^{(1)}(x) \asymp \sqrt{\frac{1}{\pi x}}\,(-1-j)\,\exp(jx) \tag{B.15}$$

$$H_1^{(2)}(x) \asymp \sqrt{\frac{1}{\pi x}}\,(-1+j)\,\exp(-jx). \tag{B.16}$$

Derivatives can be computed by

$$\frac{d}{dx}[Z_p(\alpha x)] = \alpha Z_{p-1}(\alpha x) - \frac{p}{x} Z_p(\alpha x) \tag{B.17}$$

$$= -\alpha Z_{p+1}(\alpha x) + \frac{p}{x} Z_p(\alpha x), \tag{B.18}$$

where Z_p can be J_p, Y_p, $H_p^{(1)}$ or $H_p^{(2)}$.

Modified Bessel functions of the first and second kind, of order p, are denoted by $I_p(x)$ and $K_p(x)$, respectively, and are given by

$$I_p(x) = j^{-p} J_p(jx) \tag{B.19}$$

$$K_p(x) = \frac{\pi}{2} j^{p+1} H_p^{(1)}(jx) = \frac{\pi}{2}(-j)^{p+1} H_p^{(2)}(-jx). \tag{B.20}$$

The modified Bessel function $K_p(x)$ is also called the modified Hankel function [134].

APPENDIX C

FOURIER TRANSFORM OF THE IMAGING KERNEL

C.1 Two-Dimensional Case

Here we compute the two-dimensional approximate Fourier transform of the imaging kernel $f(x', y; \omega)$ by first transforming it in the y dimension, approximating the resulting expression and then taking its transform in the x' direction. Consider the following 1-D Fourier transform pairs [134, p. 118; 136, p. 453],

$$\mathcal{F}_y\left\{\frac{\sin(b\sqrt{a^2+y^2})}{\sqrt{a^2+y^2}}\right\} = \begin{cases} \pi J_0(a\sqrt{b^2-k_y^2}) & |k_y| < b \\ 0 & |k_y| > b \end{cases} \tag{C.1}$$

$$\mathcal{F}_y\left\{\frac{\cos(b\sqrt{a^2+y^2})}{\sqrt{a^2+y^2}}\right\} = \begin{cases} -\pi Y_0(a\sqrt{b^2-k_y^2}) & |k_y| < b \\ 2K_0(a\sqrt{k_y^2-b^2}) & |k_y| > b \end{cases} \tag{C.2}$$

where the functions J_0, Y_0 and K_0 are defined in Appendix B, and the following forward and inverse Fourier transform definitions are used:

$$F(k_y) = \mathcal{F}_y\{f(y)\} = \int_{-\infty}^{\infty} f(y)e^{-jk_y y}dy \tag{C.3}$$

$$f(y) = \mathcal{IF}_y\{F(k_y)\} = \frac{1}{2\pi}\int_{-\infty}^{\infty} F(k_y)e^{jk_y y}dk_y\ . \tag{C.4}$$

Combining these two pairs we obtain

$$\mathcal{F}_y\left\{\frac{\exp\left(-jb\sqrt{a^2+y^2}\right)}{\sqrt{a^2+y^2}}\right\} = \begin{cases} -j\pi H_0^{(2)}(a\sqrt{b^2-k_y^2}) & |k_y| < b \\ 2K_0(a\sqrt{k_y^2-b^2}) & |k_y| > b\ . \end{cases} \tag{C.5}$$

Differentiating both sides of the pair with respect to b yields

$$\mathcal{F}_y\left\{\exp\left(-jb\sqrt{a^2+y^2}\right)\right\} = \begin{cases} -\pi H_1^{(2)}(a\sqrt{b^2-k_y^2})\frac{ab}{\sqrt{b^2-k_y^2}} & |k_y| < b \\ -j\pi H_1^{(2)}(-ja\sqrt{k_y^2-b^2})\frac{ab}{\sqrt{k_y^2-b^2}} & |k_y| > b\ . \end{cases} \tag{C.6}$$

By using this formula, the 1-D Fourier transform (in the dimension y) of the imaging kernel in (2.11) can be written as

$$\mathcal{F}_y\left\{f(x',y;\omega)\right\} = \begin{cases} -\pi H_1^{(2)}(x'\sqrt{4k^2-k_y^2})\frac{2kx'}{\sqrt{4k^2-k_y^2}} & |k_y| < 2k \\ -j\pi H_1^{(2)}(-jx'\sqrt{k_y^2-4k^2})\frac{2kx'}{\sqrt{k_y^2-4k^2}} & |k_y| > 2k \end{cases} \tag{C.7}$$

By using the asymptotic expansion of the Hankel functions from Appendix B, we can write

$$\begin{aligned} F_y(x',k_y;\omega) &\approx \begin{cases} \frac{-\pi 2kx'}{\sqrt{4k^2-k_y^2}}\left(\pi x'\sqrt{4k^2-k_y^2}\right)^{-\frac{1}{2}}(-1+j)e^{-jx'\sqrt{4k^2-k_y^2}} & |k_y| < 2k \\ \frac{-j\pi 2kx'}{\sqrt{k_y^2-4k^2}}\left(-j\pi x'\sqrt{k_y^2-4k^2}\right)^{-\frac{1}{2}}(-1+j)e^{-x'\sqrt{k_y^2-4k^2}} & |k_y| > 2k \end{cases} \\ &= \begin{cases} (1-j)\ 2k\ \left(\frac{\pi x'}{(4k^2-k_y^2)^{\frac{3}{2}}}\right)^{\frac{1}{2}} e^{-jx'\sqrt{4k^2-k_y^2}} & |k_y| < 2k \\ (1+j)\ 2k\ \left(\frac{j\pi x'}{(k_y^2-4k^2)^{\frac{3}{2}}}\right)^{\frac{1}{2}} e^{-x'\sqrt{k_y^2-4k^2}} & |k_y| > 2k\ . \end{cases} \end{aligned} \tag{C.8}$$

Let us define the amplitude functions

$$a_1(k,x') = (1-j)2k\left(\frac{\pi x'}{(4k^2-k_y^2)^{\frac{3}{2}}}\right)^{\frac{1}{2}} \tag{C.9}$$

$$a_2(k,x') = (1-j)2k\left(\frac{\pi x'}{(4k^2-k_y^2)^{\frac{3}{2}}}\right)^{\frac{1}{2}}\ . \tag{C.10}$$

For the case $|k_y| \ll 2k$, $a_1(k,x')$ can be approximated as

$$a_1(k,x') \approx \tilde{a}_1(k,x') = \sqrt{\frac{-j\pi x'}{k}}\ . \tag{C.11}$$

Since the change in $\tilde{a}_1(k,x')$ with respect to x' is slow, we can approximate $\tilde{a}_1(k,x')$ by a constant A_1. Then, taking the 1-D Fourier transform of the right-hand side of (C.8) with respect to x', we obtain

$$F(k_{x'},k_y;\omega) \approx \begin{cases} 2\pi A_1\ \delta(k_{x'}+\sqrt{4k^2-k_y^2}) & |k_y|<2k \\ \mathcal{F}_{x'}\left\{a_2(k,x')e^{-x'\sqrt{k_y^2-4k^2}}\right\} & |k_y|>2k\ . \end{cases} \tag{C.12}$$

C.2 Three-Dimensional Case

Consider the Fourier transform pair from [18]

$$\mathcal{F}_{x,y}\left\{\frac{e^{-ja\sqrt{b^2+x^2+y^2}}}{\sqrt{b^2+x^2+y^2}}\right\} = \frac{-j2\pi}{\sqrt{a^2-k_x^2-k_y^2}}\ e^{-jb\sqrt{a^2-k_x^2-k_y^2}} \tag{C.13}$$

with the definition of the Fourier transform given as

$$F(k_x,k_y) = \mathcal{F}_{x,y}\left\{f(x,y)\right\} = \iint_{-\infty}^{\infty} f(x,y)e^{-jk_xx-jk_yy}dxdy. \tag{C.14}$$

Taking the derivative of both sides of C.13 with respect to a and rearranging,

$$\mathcal{F}_{x,y}\left\{e^{-ja\sqrt{b^2+x^2+y^2}}\right\} = \left[\frac{2\pi a}{[a^2-k_x^2-k_y^2]^{\frac{3}{2}}} + \frac{j2\pi ab}{(a^2-k_x^2-k_y^2)}\right] e^{-jb\sqrt{a^2-k_x^2-k_y^2}}. \tag{C.15}$$

Applying this to the 3-D imaging kernel

$$f(x,y,z';\omega) = \exp\left(-j2k\sqrt{x^2+y^2+z'^2}\right), \tag{C.16}$$

we obtain the Fourier transform of the kernel in the x and y directions, which we denote by $F_{x,y}(k_x,k_y,z';\omega)$ and give as

$$F_{x,y}(k_x,k_y,z';\omega) = \left[\frac{4\pi k}{[4k^2-k_x^2-k_y^2]^{\frac{3}{2}}} + \frac{j4\pi kz'}{(4k^2-k_x^2-k_y^2)}\right] e^{-jz'\sqrt{4k^2-k_x^2-k_y^2}}. \tag{C.17}$$

For the case when $|k_x|,\ |k_y| \ll 2k$ and the variation in z' is small, we can approximate the amplitude function on the right hand side by a constant, A_2. Then,

$$F(k_x, k_y, k_{z'}; \omega) = 2\pi A_2\ \delta(k_{z'} + \sqrt{4k^2 - k_x^2 - k_y^2}). \tag{C.18}$$

APPENDIX D

STRIP-MAPPING SAR INVERSION

Here we describe the correlation-based SAR inversion algorithm for a monostatic SAR moving along a straight path and using a linear FM (chirp) probing signal [41, 42, 54]. In strip-mapping SAR, the antenna is directed broadside to sweep out a strip on the ground. At regular spatial intervals on its flight path along the y axis, the radar transmits a real passband signal as in (2.1). The range function and the complex reflectivity function are as defined in (2.4) and (2.5), respectively. We denote the range function by r'_y when the radar is at location y on the flight path and the coordinates of a particular scatterer are given by (x', y'). The return signal from a scene with reflectivity $g(x, y)$ is the sum of returns from all infinitesimal scatterers in the scene within the area illuminated by the radar beam. The return signal in real passband form can be written as

$$\tilde{s}_R(t, y) = \iint_{-\infty}^{\infty} |g(x', y')|\ w(x', y - y')\ \Re e\left\{ p(t - \frac{2r'_y}{c})\ e^{j(\omega_0(t - \frac{2r'_y}{c}) + \psi(x', y'))} \right\}\ dx'dy', \tag{D.1}$$

where the window function $w(x, y)$ models the radar antenna gain. After passing this signal through a quadrature demodulator with an oscillation phase of $\omega_0 t$, we obtain the complex baseband signal as

$$s_R(t, y) = \iint_{-\infty}^{\infty} g(x', y')\ w(x', y - y')\ p(t - \frac{2r'_y}{c}) \exp\left(-j2k_0 r'_y\right)\ dx'dy' \tag{D.2}$$

where $k_0 = \omega_0/c$.

For the case $x \gg y - y'$, that is, the case of a broadside-looking radar in the far-field, we can write using a Taylor series approximation,

$$r'_y = \sqrt{x'^2 + (y - y')^2} \approx x' + \frac{(y - y')^2}{2x'} \ . \tag{D.3}$$

We shall assume

$$p(t - \frac{2r'_y}{c}) \approx p(t - \frac{2x'}{c}) \ . \tag{D.4}$$

Then

$$s_R(t, y) \approx \iint_{-\infty}^{\infty} g(x', y')\ w(x', y - y')\ p(t - \frac{2x'}{c}) \exp(-j2k_0 x') \exp\left(-j2k_0 \frac{(y - y')^2}{2x'}\right)\ dx'dy' \ . \tag{D.5}$$

Let

$$g_1(x', y') = g(x', y') \exp(-j2k_0 x') \tag{D.6}$$

and insert $t = 2x/c$. Also, assume the antenna gain is separable into range and azimuth components as

$$w(x', y') = w_r(x')w_a(y') \ . \tag{D.7}$$

We then have the spatial version of the return signal as

$$s(x, y) = \iint_{-\infty}^{\infty} g_1(x', y')\ w_r(x')w_a(y - y')\ p(\frac{2}{c}(x - x')) \exp\left(-jk_0 \frac{(y - y')^2}{x'}\right)\ dx'dy'. \tag{D.8}$$

We can write this as

$$s(x, y) = \int_{-\infty}^{\infty} w_r(x')\ \bar{g}(x', y)\ p(\frac{2}{c}(x - x'))\ dx' \tag{D.9}$$

with

$$\bar{g}(x', y) = \int_{-\infty}^{\infty} g_1(x', y')\ w_a(y - y')\ \exp\left(-jk_0 \frac{(y - y')^2}{x'}\right)\ dy' \ . \tag{D.10}$$

D.1 Range Processing

From (D.9), we see that

$$s(x,y) = [w_r(x)\bar{g}(x,y)] * p(\frac{2x}{c}) \ . \tag{D.11}$$

An estimate of $\bar{g}(x,y)$ is found by matched filtering:

$$\begin{aligned}
\hat{\bar{g}}(x,y) &= s(x,y) * p^*(-\frac{2x}{c}) && \text{(D.12)}\\
&= \int_{-\infty}^{\infty} s(\xi,y)\ p^*(-\frac{2}{c}(x-\xi))\ d\xi && \text{(D.13)}\\
&= \iint_{-\infty}^{\infty} w_r(x')\ \bar{g}(x',y)\ p(\frac{2}{c}(\xi-x'))\ p^*(-\frac{2}{c}(x-\xi))\ dx'\ d\xi && \text{(D.14)}\\
&= \int_{-\infty}^{\infty} w_r(x')\ \bar{g}(x',y)\ \left[\int_{-\infty}^{\infty} p(\frac{2}{c}(\xi-x'))\ p^*(-\frac{2}{c}(x-\xi))\ d\xi\right] dx'. && \text{(D.15)}
\end{aligned}$$

Defining the autocorrelation as

$$\rho(\frac{2x}{c}) = \int_{-\infty}^{\infty} p(\frac{2}{c}u)\ p^*(\frac{2}{c}(u-x))\ du, \tag{D.16}$$

and making a change of variables $u = \xi - x'$ in the inner integral of (D.15), inner integral is computed to be $\rho(\frac{2}{c}(x-x'))$. Thus,

$$\hat{\bar{g}}(x,y) = [w_r(x)\bar{g}(x,y)] * \rho(\frac{2x}{c}). \tag{D.17}$$

For pulses with large time-bandwidth products, $\rho(\frac{2x}{c})$ is approximately a narrow sinc [42].

D.2 Azimuth Processing

Expressing (D.10) as a convolution,

$$\bar{g}(x,y) = \int_{-\infty}^{\infty} g_1(x,y')\ w_a(y-y')\ \exp\left(-jk_0\frac{(y-y')^2}{x}\right)\ dy' \tag{D.18}$$

$$= g_1(x,y) * \left[w_a(y) \exp\left(-jk_0 \frac{y^2}{x}\right) \right]. \tag{D.19}$$

Let

$$h_a(y) = w_a(y) \exp\left(-jk_0 \frac{y^2}{x}\right). \tag{D.20}$$

An estimate $\hat{g}_1(x,y)$ of $g_1(x,y)$ is then found again by matched filtering as follows

$$\hat{g}_1(x,y) = \bar{g}(x,y) * h_a^*(-y) \tag{D.21}$$

$$= \int_{-\infty}^{\infty} \bar{g}(x,\nu) h_a^*(-(y-\nu))\, d\nu \tag{D.22}$$

$$= \iint_{-\infty}^{\infty} g_1(x,y') \underbrace{w_a(\nu - y') \exp\left(-jk_0 \frac{(\nu - y')^2}{x}\right)}_{h_a(\nu - y')} h_a^*(-(y-\nu))\, d\nu\, dy' \tag{D.23}$$

$$= \int_{-\infty}^{\infty} g_1(x,y') \left[\int_{-\infty}^{\infty} h_a(\nu - y') h_a^*(\nu - y)\, d\nu \right] dy'. \tag{D.24}$$

Defining

$$\phi(y) = \int_{-\infty}^{\infty} h_a(u) h_a^*(u - x)\, du\ , \tag{D.25}$$

the inner integral equals $\phi(y - y')$. Thus,

$$\hat{g}_1(x,y) = g_1(x,y) * \phi(y)\ . \tag{D.26}$$

In this step, instead of $\bar{g}(x,y)$ we actually use $\hat{\bar{g}}(x,y)$ which has been found in the range processing step.

APPENDIX E

A GENERAL INVERSION METHOD (GIM)

Here we describe briefly a general inversion method for approximate solution of the Fredholm integral equation of the first kind. This method is due to Arıkan [74]. The Fredholm integral equation of the first kind is given as

$$s(x) = \int K(x,y)g(y)dy + n(x), \tag{E.1}$$

where s is the measurement, g is the physical property to be estimated, and n is the measurement noise. The measurement kernel K models the relationship between g and s, and it is assumed to possess finite energy; that is, it is square summable. When we have a 2-D physical property to be estimated, and a number of observations, we may have a set of integral equations

$$s_i(x) = \iint K_i(x-x',y)\; g(x',y)\; dy\; dx' + n_i(x) \quad 1 \le i \le I\ . \tag{E.2}$$

Each equation represents a nonseparable projection in y and a convolution in x. One way to solve this set of equations is to decompose the measurement kernel into singular functions, obtain a form of separable projection followed by convolution, and then solve for the physical property by multichannel deconvolution followed by back projection. This method has been proposed and applied to borehole induction measurements [74].

Any finite energy kernel can be approximated arbitrarily closely by means of a kernel of finite rank where the approximation is in the mean, that is in the metric of the space of square summable complex valued functions [77, p. 158]. Thus,

$$K_i(x,y) \approx \sum_{j=1}^{J_i} \lambda_{ij} u_{ij}(x) v_{ij}^*(y) \tag{E.3}$$

where

$$\lambda_{i1} \geq \lambda_{i2} \geq \ldots \geq \lambda_{iJ_i} > 0 \tag{E.4}$$

are the singular values. Error in this approximation decreases as J_i increases. The singular functions satisfy

$$\lambda_{ij} u_{ij}(x) = \int K_i(x,y) v_{ij}(y) dy \tag{E.5}$$

$$\lambda_{ij} v_{ij}(x) = \int K_i^*(x,y) u_{ij}(x) dx \tag{E.6}$$

and

$$\int u_{ij}(x) u_{ik}^*(x) dx = \delta_{jk} \tag{E.7}$$

$$\int v_{ij}(y) v_{ik}^*(y) dy = \delta_{jk} \, . \tag{E.8}$$

Inserting this into (E.2), we have

$$s_i(x) = \int \int \sum_{j=1}^{J_i} \lambda_{ij} u_{ij}(x - x') v_{ij}^*(y) g(x', y) dy dx' + n_i(x) \quad 1 \leq i \leq I \, . \tag{E.9}$$

This is a sum of convolutions of $u_{ij}(x)$ with projections of $g(x,y)$ onto $v_{ij}(y)$. Thus, components of $g(x,y)$ lying in the subspace spanned by all $v_{ij}(y)$ influence the measurement. To obtain a separable relation, we need to find an orthogonal basis for this so-called y-observable subspace. Let the orthonormal basis functions be

$$q_m(y) \quad 1 \leq m \leq M \tag{E.10}$$

and write

$$v_{ij}(y) = \sum_{m=1}^{M} \alpha_{ijm} q_m(y) \, . \tag{E.11}$$

Then,

$$s_i(x) \approx \sum_{m=1}^{M} \int \sum_{j=1}^{J_i} \lambda_{ij} u_{ij}(x - x') \alpha_{ijm}^* \int q_m^*(y) g(x', y) dy dx' + n_i(x) \, . \tag{E.12}$$

Let

$$z_{im}(x) = \sum_{j=1}^{J_i} \lambda_{ij} u_{ij}(x - x') \alpha^*_{ijm} \ , \tag{E.13}$$

which is independent of the unknown $g(x, y)$; hence it can be precomputed. The projection of $g(x, y)$ onto a basis component of the y-observable subspace is

$$p_m(x) = \int q^*_m(y) g(x, y) dy \ . \tag{E.14}$$

We then have

$$s_i(x) \approx \sum_{m=1}^{M} \int z_{im}(x - x') p_m(x') dx' + n_i(x) \quad 1 \leq i \leq I \ . \tag{E.15}$$

Here, $z_{im}(x)$ is known and we will estimate the projection $p_m(x)$ by multichannel deconvolution. Then $g(x, y)$ will be obtained by back-projection. The estimate of the projection is given by

$$\hat{p}_m(x) = \sum_{i=1}^{I} \int h_{mi}(x - x') s_i(x') dx' \ . \tag{E.16}$$

The back-projection results in

$$\hat{g}(x, y) = \sum_{m=1}^{M} \hat{p}_m(x) q_m(y) \ . \tag{E.17}$$

Measurement noise is accounted for in the deconvolution stage. The choice of deconvolution filters $h_{mi}(x)$ depends on the available a priori information on the statistics of p_m and on the estimation criterion used. In the Fourier domain

$$\hat{P}_m(\omega) = \sum_{i=1}^{I} H_{mi}(\omega) S_i(\omega), \tag{E.18}$$

which can be written in vector-matrix form as

$$\underline{\hat{P}}(\omega) = \underline{\underline{H}}(\omega) \underline{S}(\omega) \ . \tag{E.19}$$

Similarly, (E.15) can be transformed as

$$\underline{S}(\omega) = \underline{\underline{Z}}(\omega)\underline{P}(\omega) + \underline{N}(\omega) \ . \tag{E.20}$$

Thus,

$$\underline{\hat{P}}(\omega) = \underline{\underline{H}}(\omega)\underline{\underline{Z}}(\omega)\underline{P}(\omega) + \underline{\underline{H}}(\omega)\underline{N}(\omega) \ . \tag{E.21}$$

The forms of $\underline{\underline{H}}(\omega)$, which are to be given next, are not dependent on the measurements. $\underline{\underline{H}}(\omega)$ can be precomputed for each frequency ω and inverse transformed to find the deconvolution filters $h_{mi}(x)$.

E.1 Least-Squares (LS) Estimate

Assume there is no prior distribution on $\underline{P}(\omega)$. The least-squares criterion states

$$\underline{\hat{P}}(\omega) = \min_{\underline{P}(\omega)} \| \underline{S}(\omega) - \underline{\underline{Z}}(\omega)\underline{P}(\omega) \|^2 \ . \tag{E.22}$$

Expanding the square of the norm and taking the derivative with respect to $\underline{P}(\omega)$ to find the minimizing argument, we get

$$\underline{\hat{P}}(\omega) = [\underline{\underline{Z}}^{\dagger}(\omega)\underline{\underline{Z}}(\omega)]^{-1}\underline{\underline{Z}}^{\dagger}(\omega)\underline{S}(\omega) \tag{E.23}$$

where † indicates Hermitian transpose. Thus, the filter that produces $\underline{\hat{P}}(\omega)$ to minimize the norm squared is given as

$$\underline{\underline{H}}_{LS}(\omega) = \left[\underline{\underline{Z}}^{\dagger}(\omega)\underline{\underline{Z}}(\omega)\right]^{-1}\underline{\underline{Z}}^{\dagger}(\omega) \ . \tag{E.24}$$

E.2 Maximum-Likelihood (ML) Estimate

Assume $\underline{N}(\omega)$ is Gaussian with zero mean and autocorrelation $\underline{\underline{R}}_N(\omega)$. Then the log-likelihood is given as

$$\mathcal{L} = -\frac{1}{2}\left(\underline{S}(\omega) - \underline{\underline{Z}}(\omega)\underline{P}(\omega)\right)^{\dagger}\underline{\underline{R}}_N^{-1}(\omega)\left(\underline{S}(\omega) - \underline{\underline{Z}}(\omega)\underline{P}(\omega)\right) \tag{E.25}$$

and the optimal estimate is

$$\arg\max_{\underline{P}(\omega)} \mathcal{L} = \arg\min_{\underline{P}(\omega)} \left(\underline{S}(\omega) - \underline{\underline{Z}}(\omega)\underline{P}(\omega)\right)^{\dagger} \underline{\underline{R}}_N^{-1}(\omega)\left(\underline{S}(\omega) - \underline{\underline{Z}}(\omega)\underline{P}(\omega)\right) \quad \text{(E.26)}$$

$$= \min_{\underline{P}(\omega)} \left[\underline{S}(\omega)^{\dagger}\underline{\underline{R}}_N^{-1}(\omega)\underline{S}(\omega) - \underline{S}^{\dagger}(\omega)\underline{\underline{R}}_N^{-1}(\omega)\underline{\underline{Z}}(\omega)\underline{P}(\omega) - \underline{P}^{\dagger}(\omega)\underline{\underline{Z}}^{\dagger}(\omega)\underline{\underline{R}}_N^{-1}(\omega)\underline{S}(\omega) + \underline{P}^{\dagger}(\omega)\underline{\underline{Z}}^{\dagger}(\omega)\underline{\underline{R}}_N^{-1}(\omega)\underline{\underline{Z}}(\omega)\underline{P}(\omega)\right] \quad \text{(E.27)}$$

Taking the derivative with respect to $\underline{P}(\omega)$ and equating to zero, the optimum $\underline{P}(\omega)$ satisfies

$$\underline{S}(\omega)^{\dagger}\underline{\underline{R}}_N^{-1}(\omega)\underline{\underline{Z}}(\omega) = \underline{P}^{\dagger}(\omega)\underline{\underline{Z}}^{\dagger}(\omega)\underline{\underline{R}}_N^{-1}(\omega)\underline{\underline{Z}}(\omega) \; . \quad \text{(E.28)}$$

Hence,

$$\hat{\underline{P}}(\omega) = \left(\underline{\underline{Z}}^{\dagger}(\omega)\underline{\underline{R}}_N^{-1}(\omega)\underline{\underline{Z}}(\omega)\right)^{-1} \underline{\underline{Z}}^{\dagger}(\omega)\underline{\underline{R}}_N^{-1}(\omega)\underline{S}(\omega) \; , \quad \text{(E.29)}$$

and the filter for this criterion is

$$\underline{\underline{H}}_{ML}(\omega) = \left(\underline{\underline{Z}}^{\dagger}(\omega)\underline{\underline{R}}_N^{-1}(\omega)\underline{\underline{Z}}(\omega)\right)^{-1} \underline{\underline{Z}}^{\dagger}(\omega)\underline{\underline{R}}_N^{-1}(\omega) \quad \text{(E.30)}$$

E.3 Maximum a Posteriori (MAP) Estimate

Assume $\underline{P}(\omega)$ and $\underline{N}(\omega)$ are independent and Gaussian distributed with autocorrelations $\underline{\underline{R}}_N(\omega)$ and $\underline{\underline{R}}_P(\omega)$, respectively. Since

$$\underline{S}(\omega) = \underline{\underline{Z}}(\omega)\underline{P}(\omega) + \underline{N}(\omega) \; , \quad \text{(E.31)}$$

the probability distribution of the measurement given $\underline{P}(\omega)$ is Gaussian with autocorrelation $\underline{\underline{R}}_N(\omega)$. If we denote a probability distribution function by f, we have by Bayes rule,

$$f_{\underline{P}|\underline{S}} = \frac{f_{\underline{S}|\underline{P}} f_{\underline{P}}}{f_{\underline{S}}} \; . \quad \text{(E.32)}$$

The MAP estimate is then

$$\hat{\underline{P}}(\omega) = \arg\max_{\underline{P}(\omega)} f_{\underline{P}|\underline{S}} \quad \text{(E.33)}$$

$$= \arg\max_{\underline{P}(\omega)} f_{\underline{S}|\underline{P}} f_{\underline{P}} \tag{E.34}$$

$$= \arg\max_{\underline{P}(\omega)} \left(\log f_{\underline{S}|\underline{P}} + \log f_{\underline{P}} \right) \tag{E.35}$$

$$= \arg\min_{\underline{P}(\omega)} \left[\underline{S}^{\dagger}(\omega) \underline{\underline{R}}_N^{-1}(\omega) \underline{S}(\omega) - \underline{S}^{\dagger}(\omega) \underline{\underline{R}}_N^{-1}(\omega) \underline{\underline{Z}}(\omega) \underline{P}(\omega) \right.$$
$$- \underline{P}^{\dagger}(\omega) \underline{\underline{Z}}^{\dagger}(\omega) \underline{\underline{R}}_N^{-1}(\omega) \underline{S}(\omega) \tag{E.36}$$
$$\left. + \underline{P}^{\dagger}(\omega) \underline{\underline{Z}}^{\dagger}(\omega) \underline{\underline{R}}_N^{-1}(\omega) \underline{\underline{Z}}(\omega) \underline{P}(\omega) + \underline{P}^{\dagger}(\omega) \underline{\underline{R}}_P^{-1}(\omega) \underline{P}(\omega) \right] . \tag{E.37}$$

Taking the derivative of this quantity and equating to zero, we obtain the following equation to be satisfied by the optimum argument

$$\underline{S}^{\dagger}(\omega) \underline{\underline{R}}_N^{-1}(\omega) \underline{\underline{Z}}(\omega) - \underline{P}^{\dagger}(\omega) \underline{\underline{Z}}^{\dagger}(\omega) \underline{\underline{R}}_N^{-1}(\omega) \underline{\underline{Z}}(\omega) - \underline{P}^{\dagger}(\omega) \underline{\underline{R}}_P^{-1}(\omega) = 0 . \tag{E.38}$$

Thus, we have

$$\hat{\underline{P}}(\omega) = \left(\underline{\underline{Z}}^{\dagger}(\omega) \underline{\underline{R}}_N^{-1}(\omega) \underline{\underline{Z}}(\omega) + \underline{\underline{R}}_P^{-1}(\omega) \right)^{-1} \underline{\underline{Z}}^{\dagger}(\omega) \underline{\underline{R}}_N^{-1}(\omega) \underline{S}(\omega), \tag{E.39}$$

and the filter for this case is

$$\underline{\underline{H}}_{MAP}(\omega) = \left(\underline{\underline{Z}}^{\dagger}(\omega) \underline{\underline{R}}_N^{-1}(\omega) \underline{\underline{Z}}(\omega) + \underline{\underline{R}}_P^{-1}(\omega) \right)^{-1} \underline{\underline{Z}}^{\dagger}(\omega) \underline{\underline{R}}_N^{-1}(\omega). \tag{E.40}$$

E.4 Regularization

The error covariance of the maximum-likelihood estimate is

$$\mathcal{E} \left\{ \left(\underline{P}(\omega) - \underline{\underline{H}}(\omega) \underline{S}(\omega) \right) \left(\underline{P}(\omega) - \underline{\underline{H}}(\omega) \underline{S}(\omega) \right)^{\dagger} \right\} = \left(\underline{\underline{Z}}^{\dagger}(\omega) \underline{\underline{R}}_N^{-1}(\omega) \underline{\underline{Z}}(\omega) \right)^{-1} . \tag{E.41}$$

The maximum-likelihood estimate is unbiased, but its covariance can be very large due to the inversion at those frequencies where $\underline{\underline{Z}}(\omega)$ has small singular values. A regularized maximum likelihood estimate can be written as

$$\underline{\underline{H}}_{MLR}(\omega) = \left(\underline{\underline{Z}}^{\dagger}(\omega) \underline{\underline{R}}_N^{-1}(\omega) \underline{\underline{Z}}(\omega) + \mu^2(\omega) \underline{\underline{I}} \right)^{-1} \underline{\underline{Z}}^{\dagger}(\omega) \underline{\underline{R}}_N^{-1}(\omega) \tag{E.42}$$

where the regularization parameter $\mu(\omega)$ can be either a fixed function of ω or can be chosen adaptively depending on the measurement. The former is not satisfactory when there are many frequencies and the noise is not independent and identically distributed. The latter, on the other hand, requires too much computation. In [74], the filter is chosen as a solution to the problem

$$\min \| \underline{\underline{H}}(\omega)\underline{\underline{Z}}(\omega) - \underline{\underline{I}} \|_F^2 \tag{E.43}$$

subject to the constraint

$$\mathrm{tr}\left[\underline{\underline{H}}(\omega)\underline{\underline{R}}_N(\omega)\underline{\underline{H}}^\dagger(\omega)\right] \leq \epsilon^2(\omega) \tag{E.44}$$

where $\| \underline{\underline{A}} \|_F$ denotes the Frobenius norm, given as

$$\| \underline{\underline{A}} \|_F = \left(\sum_{ij} |\underline{\underline{A}}_{ij}|^2 \right)^{\frac{1}{2}}. \tag{E.45}$$

When the cost in (E.43) is small, the mean of the estimate is close to the true value and the constraints put an upper bound on the expected energy of the noise around this mean. The solution to this problem is given as

$$\underline{\underline{H}}_\epsilon(\omega) = \left(\underline{\underline{Z}}^\dagger(\omega)\underline{\underline{R}}_N^{-1}(\omega)\underline{\underline{Z}}(\omega) + \mu^2\underline{\underline{I}}\right)^{-1} \underline{\underline{Z}}^\dagger(\omega)\underline{\underline{R}}_N^{-1}(\omega) \tag{E.46}$$

with μ chosen as the solution to

$$\sum_{i=1}^{M} \left(\frac{\eta_i}{\eta_i^2 + \mu^2} \right)^2 = \epsilon^2(\omega) \tag{E.47}$$

where the η_i's are the singular values of $\underline{\underline{R}}_N^{-\frac{1}{2}}(\omega)\underline{\underline{Z}}(\omega)$.

APPENDIX F

APPLICATION OF GIM TO SAR INVERSION

Passing the real passband data in (2.6) through a quadrature demodulator with an oscillation phase of $\omega_0 t$, we obtain the complex baseband signal as

$$s_R(t,y) = \iint_{-\infty}^{\infty} g(x',y')\ w(x',y-y')\ p(t-\frac{2r'_y}{c}) \exp\left(-j2k_0 r'_y\right)\ dx'dy' \qquad \text{(F.1)}$$

where $k_0 = \omega_0/c$. The spatial version of this signal can be obtained by making a change of variable $t = 2x/c$, giving

$$s_1(x,y) = \iint_{-\infty}^{\infty} g(x',y')\ w(x',y-y')\ p\left(\frac{2}{c}(x-r'_y)\right)\ \exp\left(-j2k_0 r'_y\right)\ dx'dy'. \qquad \text{(F.2)}$$

We perform range compression on this signal by using a matched filter to give

$$\begin{aligned}
s_2(x,y) &= s_1(x,y) * p^*(-\frac{2x}{c}) \\
&= \int_{-\infty}^{\infty} s_1(\xi,y) p^*\left(-\frac{2}{c}(x-\xi)\right)\ d\xi \\
&= \iint_{-\infty}^{\infty} g(x',y')\ w(x',y-y') \\
&\quad \cdot \underbrace{\int_{-\infty}^{\infty} p\left(\frac{2}{c}(\xi-r'_y)\right) p^*\left(-\frac{2}{c}(x-\xi)\right)\ d\xi}_{\rho(\frac{2}{c}(x-r'_y))} \exp\left(-j2k_0 r'_y\right)\ dx'dy' \\
&= \iint_{-\infty}^{\infty} g(x',y')\ w(x',y-y')\ \rho(\frac{2}{c}(x-r'_y)) \exp\left(-j2k_0 r'_y\right)\ dx'dy' \\
&= \iint_{-\infty}^{\infty} K(x,y-y';x') g(x',y')\ dx'dy', \qquad \text{(F.3)}
\end{aligned}$$

where $K(x, y; x')$ is the *measurement kernel* given as

$$K(x, y; x') = w(x', y)\ \rho(\frac{2}{c}(x - r(x', y)))\exp(-j2k_0 r(x', y)) \tag{F.4}$$

and

$$\rho(\frac{2x}{c}) = \int_{-\infty}^{\infty} p(\frac{2}{c}u)\ p^*(\frac{2}{c}(u - x))\ du\ . \tag{F.5}$$

The expression for the range compressed signal is now in the form of a Fredholm integral equation of the first kind with a nonseparable kernel. The inversion method described in Appendix E can be applied to this case as explained in the following.

1. First, we wish to decompose this last integral into a set of integral equations, each along a basis component of the x-range space of the measurement kernel. For this purpose, we first find a basis for this subspace and then project the measurements onto each basis component. Let this basis be composed of vectors $\{\gamma_i(x)\}_{i=1}^{I}$. Then form

$$\Gamma(x, z) = \iint_{-\infty}^{\infty} K(x, y'; x')\ K^*(z, y'; x')\ dx'dy'\ . \tag{F.6}$$

The basis functions $\{\gamma_i(x)\}_{i=1}^{I}$ can be obtained by eigendecomposition of the discrete version of $\Gamma(x, z)$. This is a spectral representation of the measurement kernel. The number of basis functions I is determined by an energy constraint on the singular values of the discrete form of $\Gamma(x, z)$. For instance, in our simulations we choose I to keep 99% of the energy.

2. Project onto the subspace spanned by $\{\gamma_i(x)\}_{i=1}^{I}$, i.e.,

$$f_i(y) = \int_{-\infty}^{\infty} \gamma_i^*(x)\ s_2(x, y)\ dx \tag{F.7}$$

$$K_i(y, x') = \int_{-\infty}^{\infty} \gamma_i^*(x)\ K(x, y; x')\ dx \tag{F.8}$$

and obtain the decomposition into projected measurements as

$$f_i(y) = \iint_{-\infty}^{\infty} K_i(y - y', x')g(x', y')\ dx'\ dy'\ . \tag{F.9}$$

3. Represent the integral in multichannel convolution form by first approximating the kernel by

$$K_i(y,x') \approx \sum_{j=1}^{J_i} \lambda_{ij} u_{ij}(y) v_{ij}^*(x') \ . \tag{F.10}$$

Let $\{q_m(x')\}_{m=1}^M$ be an orthonormal basis. Then

$$v_{ij}(x') = \sum_{m=1}^{M} \alpha_{ijm} q_m(x') \ . \tag{F.11}$$

Then,

$$\begin{aligned} f_i(y) &\approx \sum_{m=1}^{M} \int_{-\infty}^{\infty} \underbrace{\sum_{j=1}^{J_i} \lambda_{ij} u_{ij}(y-y') \alpha_{ijm}^*}_{z_{im}(y-y')} \underbrace{\int_{-\infty}^{\infty} q_m^*(x') g(x',y') \, dx'}_{p_m(y')} \, dy' \\ &\approx \sum_{m=1}^{M} \int_{-\infty}^{\infty} z_{im}(y-y') p_m(y') \, dy', \end{aligned} \tag{F.12}$$

where

$$z_{im}(y) = \sum_{j=1}^{J_i} \lambda_{ij} u_{ij}(y) \alpha_{ijm}^* \tag{F.13}$$

$$p_m(y') = \int_{-\infty}^{\infty} q_m^*(x') g(x',y') \, dx'. \tag{F.14}$$

4. Solve the multichannel deconvolution problem to obtain the estimate of the projections as

$$\hat{p}_m(y') = \sum_{i=1}^{I} \int_{-\infty}^{\infty} h_{mi}(y'-y) f_i(y) dy \ . \tag{F.15}$$

Appendix E explains how to obtain deconvolution filters.

5. Back-project to obtain an estimate of the reflectivity.

$$\hat{g}(x',y') = \sum_{m=1}^{M} \hat{p}_m(y') q_m(x') \ . \tag{F.16}$$

REFERENCES

[1] G. N. Hounsfield, "Computerized transverse axial scanning (tomography): I. Description of system," *Br. J. Radiol.*, vol. 46, pp. 1016–1022, 1973.

[2] G. T. Herman, *Image Reconstruction From Projections: The Fundamentals of Computerized Tomography.* New York: Academic Press, 1980.

[3] S. R. Deans, *The Radon Transform and Some of Its Applications.* New York: Wiley, 1983.

[4] A. Macovski, *Medical Imaging Systems.* Englewood Cliffs, NJ: Prentice-Hall, 1983.

[5] A. C. Kak and M. Slaney, *Principles of Computerized Tomographic Imaging.* New York: IEEE Press, 1988.

[6] *IEEE Trans. Biomedical Engineering,* special issue on computerized medical imaging, vol. BME-28, no. 2, Feb. 1981.

[7] *Proceedings of the IEEE,* special issue on computerized tomography, vol. 71, no. 3, Mar. 1983.

[8] W. H. Munk, P. Worcester, and C. Wunsch, *Ocean Acoustic Tomography.* New York: Cambridge University Press, 1995.

[9] K. K. Shung, M. B. Smith, and B. M. W. Tsui, *Principles of Medical Imaging.* San Diego, CA: Academic Press, 1992.

[10] G. F. Roach, Ed., *Inverse Problems and Imaging.* New York: Longman Scientific & Technical, 1991.

[11] B. E. Hornby, "Tomographic reconstruction of near-borehole slowness using refracted borehole sonic arrivals," *Geophysics*, vol. 58, pp. 1726–1738, Dec. 1993.

[12] H. Na and C. Biswas, "Three-dimensional computerized ionospheric tomography using volumetric constraints," *Radio Science*, vol. 33, pp. 1793–1805, Nov.-Dec. 1998.

[13] S. Gindikin and P. Michor, Eds., *75 Years of Radon Transform.* Boston, MA: International Press, 1994.

[14] A. Cormack, "Representation of a function by its line integrals, with some radiological applications," *J. Appl. Phys.*, vol. 34, pp. 2722–2727, 1963.

[15] R. M. Mersereau and A. V. Oppenheim, "Digital reconstruction of multidimensional signals from their projection," *Proc. IEEE*, vol. 62, pp. 1319–1338, Oct. 1974.

[16] D. E. Dudgeon and R. M. Mersereau, *Multidimensional Digital Signal Processing.* Englewood Cliffs, NJ: Prentice Hall, 1984.

[17] F. Natterer, *The Mathematics of Computerized Tomography.* New York: John Wiley & Sons, 1986.

[18] R. E. Blahut, *Theory of Remote Image Formation.* New York: Cambridge University Press, to be published.

[19] A. K. Jain, *Fundamentals of Digital Image Processing.* Englewood Cliffs, NJ: Prentice Hall, 1989.

[20] S. Gindikin, Ed., *Applied Problems of Radon Transform*, vol. 162 of *American Mathematical Society Translations, Series 2.* Providence, RI: American Mathematical Society, 1994.

[21] R. J. Gardner, *Geometric Tomography.* New York: Cambridge University Press, 1995.

[22] A. G. Ramm and A. I. Katsevic, *The Radon Transform and Local Tomography.* Boca Raton, FL: CRC Press, 1996.

[23] G. T. Herman and A. Kuba, Eds., *Discrete Tomography: Foundations, Algorithms and Applications.* Boston: Birkhäuser, 1999.

[24] H. J. Scudder, "Introduction to computer aided tomography," *Proc. IEEE*, vol. 66, pp. 628–637, June 1978.

[25] D. E. Kuhl and R. Q. Edwards, "Image separation radioisotope scanning," *Radiol.*, vol. 80, pp. 653–662, 1963.

[26] R. Jaszczak, "Tomographic radiopharmaceutical imaging," *Proc. IEEE*, vol. 76, no. 9, pp. 1079–1094, 1988.

[27] R. E. Coleman, R. A. Blinder, and R. J. Jaszczak, "Single photon emission computed tomography (SPECT) Part II: Clinical applications," *Inv. Radiol.*, vol. 21, no. 1, pp. 1–11, 1986.

[28] R. Leahy and C. Byrne, "Recent developments in iterative image reconstruction for PET and SPECT," *IEEE Trans. Medical Imaging*, vol. 19, pp. 257–260, Apr. 2000.

[29] Z. H. Cho, H. S. Kim, H. B. Song, and J. Cumming, "Fourier transform nuclear magnetic resonance tomographic imaging," *Proc. IEEE*, vol. 70, pp. 1152–1173, Oct. 1982.

[30] M. A. Foster, *Magnetic Resonance in Medicine and Biology.* New York: Pergamon Press, 1984.

[31] D. D. Stark and W. G. Bradley, *Magnetic Resonance Imaging.* St. Louis, MO: C. V. Mosby Co., 1988.

[32] C. A. Zelt, A. M. Hojka, E. R. Flueh, and K. D. McIntosh, "3D simultaneous seismic refraction and reflection tomography of wide-angle data from the central Chilean margin," *Geophys. Res. Lett.*, vol. 26, pp. 2577–2580, 1999.

[33] M. Weijian and G. W. Stuart, "Transmission-reflection tomography: Application to reverse VSP data," *Geophysics*, vol. 62, pp. 884–894, May-June 1997.

[34] P. Carrion, "Reflection tomography in underwater acoustics," *J. Acoust. Soc. Am.*, vol. 97, pp. 1318–1321, Feb. 1995.

[35] J. Lefebvre, P. Recotillet, and P. Lasaygues, "NDE application of ultrasonic reflection tomography," in *Proc. IEEE Ultrasonics Symposium*, vol. 2, 1994, pp. 1289–1292.

[36] C. Stork, "Reflection tomography in the postmigrated domain," *Geophysics*, vol. 57, pp. 680–692, May 1992.

[37] K. A. Dines and S. A. Goss, "Computed ultrasonic reflection tomography," *IEEE Trans. Ultrasonics, Ferroelectrics, Frequency Control*, vol. UFFC-34, pp. 309–318, May 1987.

[38] P. B. Abraham and C. F. Gaumond, "Reflection tomography," *J. Acoust. Soc. Am.*, vol. 82, pp. 1303–1314, Oct. 1987.

[39] D. C. Munson, Jr., J. D. O'Brien, and W. K. Jenkins, "A tomographic formulation of spotlight-mode synthetic aperture radar," *Proc. IEEE*, vol. 71, pp. 917–925, Aug. 1983.

[40] C. V. Jakowatz, Jr., D. E. Wahl, P. H. Eichel, D. C. Ghiglia, and P. A. Thompson, *Spotlight-Mode Synthetic Aperture Radar: A Signal Processing Approach.* Boston: Kluwer Academic Publishers, 1996.

[41] D. C. Munson, Jr., "An introduction to strip-mapping synthetic aperture radar," in *Proc. IEEE Int. Conf. Acoust., Speech, Signal Processing*, vol. 4, Dallas, TX, April 6-9, 1987, pp. 2245–2248.

[42] D. C. Munson, Jr., and R. L. Visentin, "A signal processing view of strip-mapping synthetic aperture radar," *IEEE Trans. Acoust., Speech, Signal Processing*, vol. 37, pp. 2131–2147, Dec. 1989.

[43] B. K. P. Horn, "Density reconstruction using arbitrary ray-sampling schemes," *Proc. IEEE*, vol. 66, no. 5, pp. 551–562, 1978.

[44] D. A. Hayner and W. K. Jenkins, "The missing cone problem in computer tomography," in *Advances in Computer Vision and Image Proceesing*, vol. 1, T. S. Huang, Ed. Greenwich, CT: JAI Press, 1984, pp. 83–144.

[45] F. Macias-Garza, A. C. Bovik, and K. R. Diller, "Missing cone of frequencies and low-pass distortion in three-dimensional microscopic images," *Optical Engineering*, vol. 27, pp. 461–465, June 1988.

[46] R. Rangayyan, A. P. Dhawan, and R. Gordan, "Algorithms for limited-view computed tomography: An annotated bibliography and a challange," *Appl. Opt.*, vol. 24, pp. 4000–4012, 1985.

[47] D. Verhoeven, "Limited-data computed tomography algorithms for the physical sciences," *Appl. Opt.*, vol. 32, pp. 3736–3754, 1993.

[48] A. H. Delaney and Y. Bresler, "A fast and accurate Fourier algorithm for iterative parallel-beam tomography," *IEEE Trans. Image Processing*, vol. 5, pp. 740–753, May 1996.

[49] A. H. Delaney and Y. Bresler, "Globally convergent edge-preserving regularized reconstruction: An application to limited-angle tomography," *IEEE Trans. Image Processing*, vol. 7, pp. 204–221, Feb. 1998.

[50] P. Feng, S. F. Yau, and Y. Bresler, "A multicoset sampling approach to the missing cone problem in computer-aided tomography," in *Proc. IEEE Int. Symp. Circuits and Systems*, vol. 2, Atlanta, GA, May 12-15, 1996, pp. 734–737.

[51] H. Choi, "Signal processing issues in synthetic aperture radar and computer tomography," Ph.D. dissertation, University of Illinois at Urbana-Champaign, 1997.

[52] J. A. C. Lee, "Topics in image-formation algorithms for synthetic aperture radar," Ph.D. dissertation, University of Illinois at Urbana-Champaign, 1997.

[53] A. W. Rihaczek, *Principles of High-Resolution Radar*. New York: McGraw-Hill, 1969.

[54] J. C. Curlander and R. N. McDonough, *Synthetic Aperture Radar*. New York: John Wiley & Sons, 1991.

[55] W. C. Carrara, R. S. Goodman, and R. M. Majewski, *Spotlight Synthetic Aperture Radar: Signal Processing Algorithms*. Norwood, MA: Artech House, 1995.

[56] G. Franceschetti and R. Lanari, *Synthetic Aperture Radar Processing*. Boca Raton, FL: CRC Press, 1999.

[57] C. Cafforio, C. Prati, and F. Rocca, "SAR data focusing using seismic migration techniques," *IEEE Trans. Aerosp. Electron. Syst.*, vol. 27, pp. 194–207, March 1991.

[58] C. Cafforio, C. Prati, and F. Rocca, "Full resolution focusing of Seasat SAR images in the frequency-wave number domain," *Int. J. Remote Sensing*, vol. 12, no. 3, pp. 491–510, 1991.

[59] M. Soumekh, "A system model and inversion for synthetic aperture radar imaging," *IEEE Trans. Image Processing*, vol. 1, pp. 64–76, Jan. 1992.

[60] M. Soumekh, "Bistatic synthetic aperture radar inversion with application in dynamic object imaging," *IEEE Trans. Signal Processing*, vol. 39, pp. 2044–2055, Sept. 1991.

[61] R. Bamler, "A comparison of range-doppler and wavenumber domain SAR focusing algorithms," *IEEE Trans. Geosci. Remote Sens.*, vol. 30, pp. 706–713, July 1992.

[62] A. S. Milman, "SAR imaging by $\omega - k$ migration," *Int. J. Remote Sens.*, vol. 14, no. 10, pp. 1965–1979, 1993.

[63] M. Soumekh, *Synthetic Aperture Radar Signal Processing with MATLAB Algorithms*. New York: Wiley, 1999.

[64] R. Stolt, "Migration by Fourier transform," *Geophysics*, vol. 43, pp. 23–48, Feb. 1978.

[65] J. Gazdag and P. Sguazzero, "Migration of seismic data," *Proc. IEEE*, vol. 72, pp. 1302–1315, Oct. 1984.

[66] P. M. Morse and H. Feshbach, *Methods of Theoretical Physics*. New York: McGraw-Hill, 1953.

[67] J. A. C. Lee and D. C. Munson, Jr., "Runway imaging from an approaching aircraft using synthetic aperture radar," in *Proc. IEEE Int. Conf. Image Processing*, vol. 3, Sept. 16-19, 1996, pp. 915–918.

[68] R. Rau, "Postprocessing tools for ultra-wideband SAR images," Ph.D. dissertation, Georgia Institute of Technology, Atlanta, 1998.

[69] S. Cloude, A. Milne, P. D. Smith, C. Thornhill, and G. Crisp, "K-space imaging algorithms applied to UWB SAR," in *Proc. IEEE Int. Conf. Image Processing*, vol. 1, Nov. 13–16, 1994, pp. 491–495.

[70] M. Soumekh, "Reconnaissance with ultra wideband UHF synthetic aperture radar," *IEEE Signal Processing Mag.*, vol. 12, pp. 21–40, July 1995.

[71] C. A. Balanis, *Antenna Theory: Analysis and Design*. New York: Wiley, 1982.

[72] J. A. C. Lee and D. C. Munson, Jr., "Effect of a nonplanar wavefront in spotlight-mode synthetic aperture radar," in *Proc. IEEE Int. Conf. Image Processing*, vol. 1, Austin, TX, Nov. 13-16, 1994, pp. 481–485.

[73] F. G. Tricomi, *Integral Equations*. New York: Dover Publications, 1985, reprint ed.

[74] O. Arıkan, "Regularized inversion of a two-dimensional integral equation with application in borehole induction measurements," *Radio Science*, vol. 29, pp. 519–538, May-June 1994.

[75] J. A. C. Lee, O. Arıkan, and D. C. Munson, Jr., "Formulation of a general imaging algorithm for high-resolution synthetic aperture radar," in *Proc. IEEE Int. Conf. Acoust., Speech, Signal Processing*, vol. 4, Atlanta, GA, May 7-10, 1996, pp. 2092–2095.

[76] D. Hanselman and B. Littlefield, *Mastering MATLAB 5: A comprehensive Tutorial and Reference*. Upper Saddle River, NJ: Prentice Hall, 1998.

[77] F. Riesz and B. Szökefalvi-Nagy, *Functional Analysis*. New York: Dover, 1990.

[78] A. A. Giordano and F. M. Hsu, *Least Square Estimation with Application to Digital Signal Processing*. New York: John Wiley & Sons, 1985.

[79] N. Çadallı and D. C. Munson, Jr., "A simulation study of the $\omega - k$ SAR algorithm for the highly squinted case with application to runway imaging," in *Proc. IEEE Int. Conf. Acoust., Speech, Signal Processing*, vol. 5, Istanbul, Turkey, June 5-9, 2000, pp. 3025–3028.

[80] L. Råde and B. Westergen, *Beta Mathematics Handbook*, 2nd ed. Boca Raton, FL: CRC Press, 1990.

[81] J. Gallagher, N.C., "Median filters: A tutorial," in *Proc. IEEE Int. Symp. Circuits and Systems*, vol. 2, June 7-9, 1988, pp. 1737 - 1744.

[82] A. Restrepo (Palacios) and L. Chacon, "A smooting property of the median filter," *IEEE Trans. Signal Processing*, vol. 42, pp. 1553–1555, June 1994.

[83] Neal C. Gallagher, Jr. and G. L. Wise, "A theoretical analysis of the properties of median filters," *IEEE Trans. Acoust., Speech, Signal Processing*, vol. ASSP-29, pp. 1136–1141, Dec. 1981.

[84] A. J. Witten and W. C. King, "Acoustic imaging of subsurface features," *J. Env. Eng.*, vol. 116, pp. 166–181, Feb. 1990.

[85] L. Peters, Jr., J. J. Daniels, and J. D. Young, "Ground penetrating radar as a subsurface environmental sensing tool," *Proc. IEEE*, vol. 82, pp. 1802–1822, Dec. 1994.

[86] D. M. McCann, P. D. Jackson, and P. J. Fenning, "Comparison of seismic and ground probing radar methods in geological surveying," *IEE Proceedings*, vol. 135, Pt. F, pp. 380–390, Aug. 1988.

[87] M. Soumekh, "Depth-focused interior echo imaging," *IEEE Trans. Image Processing*, vol. 8, pp. 1608–1618, Nov. 1999.

[88] M. A. Biot, "Theory of propagation of elastic waves in a fluid saturated porous solid: I. Low-frequency range," *J. Acoust. Soc. Am*, vol. 28, pp. 168–178, Mar. 1956.

[89] M. A. Biot, "Theory of propagation of elastic waves in a fluid saturated porous solid: II. High-frequency range," *J. Acoust. Soc. Am*, vol. 28, pp. 179–191, Mar. 1956.

[90] W. D. O'Brien, Jr., and R. G. Darmody, "Acoustic characterization of soil," *Soil Science Society of America Journal*, 1999, submitted for publication.

[91] C. Hickey and J. Sabatier, "Measurements of two types of dilatational waves in an air-filled unconsolidated sand," *J. Acoust. Soc. Am.*, vol. 102, pp. 128–136, July 1997.

[92] J. W. Goodman, "Statistical properties of laser speckle patterns," in *Laser Speckle and Related Phenomena*, J. C. Dainty, Ed. Berlin: Springer-Verlag, 1977, pp. 9–77.

[93] V. Dutt, "Statistical analysis of ultrasound echo envelope," Ph.D. dissertation, The Mayo Graduate School, Rochester, MN, 1995.

[94] A. D. Pierce, *Acoustics: An Introduction to Its Physical Principles and Applications*. New York: McGraw-Hill, 1981.

[95] J. P. Weight and A. J. Hayman, "Observations of the propagation of very short ultrasonic pulses and their reflection by small targets," *J. Acoust. Soc. Am.*, vol. 63, pp. 396–404, Feb. 1978.

[96] C. H. Frazier, N. Çadallı, D. C. Munson, Jr., and W. D. O'Brien, Jr., "Acoustic imaging of objects buried in soil," *J. Acoust. Soc. Am.*, vol. 108, pp. 147–156, July 2000.

[97] J. A. Kong, *Electromagnetic Wave Theory*. New York: John Wiley & Sons, 1986.

[98] C. A. Balanis, *Advanced Engineering Electromagnetics*. New York: Wiley, 1989.

[99] N. G. Jerlov, *Marine Optics*. Amsterdam: Elsevier Scientific Publishing, 1976.

[100] A. Ishimaru, *Wave Propagation and Scattering in Random Media*. New York: Academic Press, 1978.

[101] R. M. Measures, *Laser Remote Sensing: Fundamentals and Applications*. New York: John Wiley & Sons, 1984.

[102] L. Tsang, J. A. Kong, and R. T. Shin, *Theory of Microwave Remote Sensing*. New York: John Wiley & Sons, 1985.

[103] J. R. Apel, *Principle of Ocean Physics.* Orlando, FL: Academic Press, 1987.

[104] C. D. Mobley, *Light and Water: Radiative Transfer in Natural Waters.* San Diego, CA: Academic Press, 1994.

[105] R. E. Walker, *Marine Light Field Statistics.* New York: John Wiley & Sons, 1994.

[106] I. L. Katsev, E. P. Zege, A. S. Prikhach, and I. N. Polonsky, "Efficient technique to determine backscattered light power for various atmospheric and oceanic sounding and imaging systems," *J. Opt. Soc. Am.*, vol. A-14, pp. 1338–1346, June 1997.

[107] J. W. McLean, J. D. Freeman, and R. E. Walker, "Beam spread function with time dispersion," *Applied Optics*, vol. 37, pp. 4701–4711, 20 July 1998.

[108] R. E. Walker and J. W. McLean, "Lidar equations for turbid media with pulse stretching," *Applied Optics*, vol. 38, pp. 2384–2397, 20 April 1999.

[109] A. Papoulis, *Probability, Random Variables and Stochastic Processes*, 3rd ed. New York: McGraw-Hill, 1991.

[110] R. F. Lutomirski, A. P. Ciervo, and G. J. Hall, "Moments of multiple scattering," *Appl. Opt.*, vol. 34, pp. 7125–7136, 1995.

[111] M. Born and E. Wolf, *Principles of Optics: Electromagnetic Theory of Propagation, Interference and Diffraction of Light*, 7th ed. New York: Cambridge University Press, 1999.

[112] B. E. A. Saleh and M. C. Teich, *Fundamentals of Photonics.* New York: Wiley, 1991.

[113] K. E. Atkinson, *An Introduction to Numerical Analysis*, 2nd ed. New York: John Wiley & Sons, 1989.

[114] R. W. Hamming, *Numerical Methods for Scientists and Engineers.* New York: McGraw-Hill, 1962.

[115] J. W. McLean and J. D. Freeman, "Effects of ocean waves on airborne lidar imaging," *Applied Optics*, vol. 35, pp. 3261–3269, June 1996.

[116] P. J. Shargo, N. Çadallı, A. C. Singer, and D. C. Munson, Jr., "A tomographic framework for LIDAR imaging," accepted for publication in Proc. IEEE Int. Conf. Acoust., Speech, Signal Processing, 2001.

[117] A. J. Johnson, D. L. Marks, R. A. Stack, D. J. Brady, and D. C. Munson Jr., "Three-dimensional surface reconstruction of optical lambertian objects using cone-beam tomography," in *Proc. Int. Conf. Image Processing*, Kobe, Japan, Oct. 24–28, 1999.

[118] O. J. Tretiak and C. Metz, "The exponential radon transform," *SIAM J. Appl. Math.*, vol. 39, pp. 341–354, 1980.

[119] F. Natterer, "On the inversion of the attenuated radon transforms," *Numer. Math.*, vol. 32, pp. 431–438, 1979.

[120] G. T. Gullberg and T. F. Budinger, "The use of filtering methods to compensate for constant attenuation in single-photon emission computed tomography," *IEEE Trans. Biomedical Engineering*, vol. BME-28, pp. 142–157, Feb. 1981.

[121] G. T. Gullberg, R. H. Huesman, J. A. Malko, N. J. Pelc, and T. F. Budinger, "An attenuated projector-backprojector for iterative spect reconstruction," *Physics in Med. Biol.*, vol. 30, pp. 799–816, Aug. 1985.

[122] Y. Weng, G. L. Zeng, and G. T. Gullberg, "Analytical inversion formula for uniformly attenuated fan-beam projections," *IEEE Trans. Nuclear Science*, vol. 44, pp. 243–249, Apr. 1997.

[123] A. Welch, , R. Clack, F. Natterer, and G. T. Gullberg, "Toward accurate attenuation correction in spect without transmission measurements," *IEEE Trans. Medical Imaging*, vol. 16, pp. 532–541, Oct. 1997.

[124] A. Welch, C. Campbell, R. Clackdoyle, F. Natterer, M. Hudson, A. Bromiley, P. Mikecz, F. Chillcot, M. Dodd, P. Hopwood, S. Craib, G. T. Gullberg, and P. Sharp, "Attenuation correction in pet using consistency information," *IEEE Trans. Nuclear Science*, vol. 45, pp. 3134–3141, Dec. 1998.

[125] O. Arıkan, "Investigation of topics in radar signal processing," Ph.D. dissertation, University of Illinois at Urbana-Champaign, 1990.

[126] N. Çadallı and D. C. Munson, Jr., "A comparison of $\omega - k$ and generalized SAR inversion for runway imaging," in *Proc. IEEE Int. Conf. Image Processing*, Vancouver, BC, Canada, Sept. 10-13, 2000.

[127] N. Çadallı, J. A. C. Lee, and D. C. Munson, Jr., "Feasibility of runway imaging by using wavenumber-domain SAR inversion," to be submitted to IEEE Trans. Aerosp. Electron. Syst.

[128] D. J. Andersh, S. W. Lee, F. L. Beckner, M. Gilkey, R. Schindel, M. Hazlett, and C. L. Yu, "XPATCH: A high frequency electromagnetic scattering prediction code using shooting and bouncing rays," in *Proc. 10th Annual Review of Progress in Applied Computational Electromagnetics*, vol. 2, 1994, pp. 424–33.

[129] J. M. Song, C. C. Lu, W. C. Chew, and S. W. Lee, "Fast Illinois solver code (FISC)," *IEEE Antennas Propag. Mag.*, vol. 40, pp. 27–34, June 1998.

[130] N. Çadallı, C. H. Frazier, D. C. Munson, Jr., and W. D. O'Brien, Jr., "Acoustic imaging of objects buried in soil," in *Proc. IEEE Int. Conf. Image Processing*, vol. 1, Chicago, IL, Oct. 4-7, 1998, pp. 14–18.

[131] C. H. Frazier, N. Çadallı, D. C. Munson, Jr., and W. D. O'Brien, Jr., "A subsurface acoustic imaging system," in *IEEE Ultrasonics Symposium Proc.*, vol. 1, Sendai, Japan, Oct. 5-8, 1998, pp. 739–742.

[132] N. Çadallı, P. J. Shargo, A. C. Singer, and D. C. Munson, Jr., "3-D tomographic imaging of ocean mines from real and simulated lidar returns," abstract submitted to SPIE's 46th Annual Meeting: The International Symposium on Optical Science and Technology, 29 July–3 August, 2001.

[133] A. V. Oppenheim and R. W. Schafer, *Discrete-Time Signal Processing*. Englewood Cliffs, NJ: Prentice Hall, 1989.

[134] W. Magnus and F. Oberhettinger, *Formulas and Theorems for the Functions of Mathematical Physics*. New York: Chelsea, 1954.

[135] M. Abramowitz and I. Stegun, Eds., *Handbook of Mathematical Functions with Formulas, Graphs and Mathematical Tables*, 9th ed. New York: Dover, 1977.

[136] S. M. Selby, Ed., *CRC Standard Mathematical Tables*, 20th ed. Cleveland, OH: The Chemical Rubber Co., 1972.

VITA

Nail Çadallı received the B.S. and M.S. degrees both in electrical and electronics engineering from Bilkent University, Ankara, Turkey, in 1994 and 1996, respectively. During his B.S. study, he was a recipient of Bilkent University Scholarship. From August 1994 to August 1996, he was a research assistant at the Department of Electrical and Electronics Engineering at Bilkent University, Ankara, Turkey.

He entered the Ph.D. program in the department of Electrical and Computer Engineering at the University of Illinois at Urbana-Champaign in September 1996. Since then, he has been working as a research assistant at the Coordinated Science Laboratory of the University of Illinois at Urbana-Champaign. He spent the summer of 1998 at Schlumberger-Doll Research Center, Ridgefield, CT. His research interests include signal and image processing, synthetic aperture radar, and tomography.